Helsinki University of Technology
Department of Electrical and Communications Engineering
Laboratory of Electronics Production Technology
Espoo 2007

Vibration test as a new method for studying the mechanical reliability of solder interconnections under shock loading conditions

Pekka Marjamäki

Dissertation for the degree of Doctor of Science in Technology to be presented with due permission of the Department of Electrical and Communications Engineering, Helsinki University of Technology, for public examination and debate in Auditorium S5 at Helsinki University of Technology (Espoo, Finland) on the 20^{th} of April, 2007, at 12.

SUPERVISOR

Professor Jorma Kivilahti, D. Sc. (Eng.)
Department of Electrical and Communications Engineering
Laboratory of Electronics Production Technology

REVIEWERS

Professor Heikki Martikka, D. Sc. (Eng.)
Lappeenranta University of Technology
Department of Mechanical Engineering
Laboratory of Machine Elements and Mechanisms

Senior Specialist Olli Salmela, D. Sc. (Eng.)
Nokia, P.O. Box 301, 00045 Nokia Group
Nokia, Linnoitustie 6, 02600 Espoo

OPPONENTS

Senior Specialist Olli Salmela, D. Sc. (Eng.)
Nokia, P.O. Box 301, 00045 Nokia Group
Nokia, Linnoitustie 6, 02600 Espoo

Chief Research Scientist Jaakko Lenkkeri, D. Sc. (Eng.)
VTT Technical Research Centre of Finland, P.O. Box 1100, 90571 Oulu

Distribution:
Helsinki University of Technology
Department of Electrical and Communications Engineering
Laboratory of Electronics Production Technology
P.O. Box 3000
FIN-02015 HUT, Finland
Tel: +358 (0)9 451 2716
Fax: +358 (0)9 451 5776
E-mail: Pia.Holmberg@tkk.fi
www.ept.tkk.fi

TKK-EVT-17
ISSN 1457-0440
ISBN 978-951-22-8734-5 (printed)
ISBN 978-951-22-8735-2 (pdf)

Abstract

This thesis presents a new large-amplitude vibration test method for studying the reliability of electronic assemblies under mechanical shock loadings. The vibration test has two important advantages as compared to the widely employed JESD22-B111 drop test: firstly, the vibration test is a more versatile method and, secondly, the testing can be carried out very rapidly, in the matter of seconds. The impact forces caused by dropping of portable devices make their component boards to vibrate excessively, which causes failures in solder interconnections between component bodies and the bending circuit boards. The component boards can be drop tested according to the JEDEC standard or vibration tested with the method developed in this work. The loading conditions and the failure modes during the tests are compared by making use of the finite element method, experimental measurements, and the standard methods of failure analysis. The finite element method is used to analyse the vibration of the component boards during the tests and the stresses produced in the interconnections. The plastic properties needed for the analyses are measured for the three solders (Sn2Ag0.5Cu, Sn3.4Ag0.8Cu, and Sn4Ag0.5Cu) as a function of strain rate and temperature. Due to the high strain rates during the rapid bending in the tests, the magnitudes of stresses increase significantly as compared to those during thermal cycling. According to the analyses, the vibration system generates equivalent stresses as the drop test, if the bending frequency and amplitude are properly adjusted. Strain gauges are used to determine the bending of the component boards during the drop tests, and similar vibratory bending is reproduced with the help of the vibration system. When the bending frequencies and amplitudes of the component boards in the vibration test are similar to those in the drop test, the same failure modes are observed. Because of the similar strain rates, maximum strains, calculated stresses, and the same observed failure modes, it is concluded that the vibration test can be used for studying the reliability of solder interconnections under shock loading conditions.

Tiivistelmä

Tämä väitöskirja esittelee uuden suurella amplitudilla tapahtuvan tärytystestausmenetelmän, joka on tarkoitettu komponenttilevyjen luotettavuuden tutkimiseen mekaanisessa iskumaisessa kuormituksessa. Tärytystestillä on kaksi merkittävää etua laajasti käytettyyn JESD22-B111-pudotustestiin verrattuna: tärytyslaitteistolla voidaan tehdä monipuolisempia testejä ja testit ovat erittäin nopeita, sekuntien luokkaa. Kannettavan laitteen putoamisesta aiheutuvan iskun johdosta laitteen piirilevyt alkavat värähdellä voimakkaasti, mikä aiheuttaa vaurioita komponenttien ja taipuvan piirilevyn välissä oleviin juoteliitoksiin. Komponenttilevyjä voidaan pudotustestata JEDEC:n standardin mukaisesti tai tärytystestata tässä työssä kehitetyllä menetelmällä. Työssä testien aikaisia kuormituksia ja syntyneitä vauriotyyppejä verrattiin elementtimenetelmällä, mittauksilla ja normaaleilla vaurioanalyysimenetelmillä. Elementtimenetelmällä analysoitiin komponenttilevyjen värähtelyä testien aikana ja juoteliitoksiin syntyneitä jännityksiä. Laskuja varten kolmen juotteen (Sn2Ag0.5Cu, Sn3.4Ag0.8Cu ja Sn4Ag0.5Cu) plastiset ominaisuudet mitattiin venymänopeuden ja lämpötilan funktioina. Nopean taipumisen aiheuttamien suurten venymänopeuksien vuoksi jännitykset kasvavat näissä testeissä merkittävästi yli lämpösyklauksessa esiintyvien jännitysten. Jännitysanalyysin perusteella tärytyslaitteisto synnyttää pudotustestausta vastaavat jännitykset, kun herätteen taajuus ja amplitudi säädetään sopiviksi. Komponenttilevyjen taipumaa pudotustestissä tutkittiin venymäliuskoilla ja vastaava taipuma aiheutettiin tärytyslaitteistolla. Kun tärytystestissä komponenttilevyjen taipuman taajuus ja amplitudi olivat saman suuruisia kuin pudotustestissä, havaittiin samat vauriotyypit. Saman suuruisten venymänopeuksien, venymien ja laskettujen jännitysten sekä samojen vauriotyyppien vuoksi voidaan päätellä, että tärytystestillä voidaan tutkia juoteliitosten luotettavuutta iskumaisissa kuormituksissa.

Preface

The work for this thesis has been carried out at the Department of Electrical and Communications Engineering at the Helsinki University of Technology. I am grateful to my supervisor professor Jorma Kivilahti for his advice and support that helped me to complete this thesis.

I would like to thank Dr. Toni Mattila for the numerous discussions during this study. I am also grateful to my co-workers Anna Rantala, Ratan Saha, Hanna Järvelä, and Tommi Repo for their contribution to the experimental work. And I thank all my colleagues for the pleasant working environment and the help in the numerous small tasks. I would also like thank my family and friends for their interest in my work and for the friendly mocking due to the slow progress.

The financial support from the National Technology Agency of Finland (TEKES), Aspocomp Group, Atotech GmbH, Elcoteq SE, Micro Analog Systems Oy, and Nokia Group is greatly acknowledged.

Contents

List of abbreviations and symbols

BGA	ball grid array (a component type)
CSP	chip scale package (package size $\leq 1.2 \times$ chip size) (a component type)
FC	flip chip (a component type)
FE	finite element
FEA	finite element analysis
FEM	finite element method
FR4	fibre reinforced epoxy (Flame Retardant, type 4)
GLJ	grooved lap joint
IMC	intermetallic compound
LPI	liquid photoimageable soldermask
OSP	organic solderability preservative
PWB	printed wiring board, printed circuit board
RCC	resin coated copper
SMT	surface mount technology
UBM	under bump metallisation

a	material parameter, or crack length
a_{cr}	crack length at the moment of failure
A	crack area, or area
b	length of the Burgers vector
B	magnitude of magnetic field
c	damping coefficient
c_{cr}	critical value of the damping coefficient
$\boldsymbol{C}$	damping matrix
C_i	material parameters, $i = 1, 2, \ldots$
D	grain size
e	Napier's constant or Euler number $e = 2.71828...$
e_r	square of a relative error
E	elastic modulus, Young's modulus
f	yield surface, or frequency
f_d, f_n	frequency, natural frequency
F, F_x, F_y	force and it's components in the x- and y-directions
F_B	magnetic force
G	shear modulus
$\mathcal{G}$	energy release rate
$\mathcal{G}_c$	critical value of the energy release rate
g_n	standard acceleration due to gravity, $g_n = 9.80665\ \mathrm{m/s^2}$
h_0	material parameter in Anand's creep model
h_{joint}	height of a joint
h_{PWB}	height of a circuit board
I	second moment of area
I_e	excitation current
J	energy released by a propagating crack
k	spring constant, or the Boltzmann constant $k = 1.3807 \cdot 10^{-23}\ \mathrm{J/K}$
K	stiffness of a plate
$\boldsymbol{K}$	stiffness matrix
K_I	stress intensity factor

ΔK	stress intensity range
L, L_x, L_y	length, dimensions in the x- and y-directions
m	mass
$\bar{m}$	mass per unit length or unit area
$\boldsymbol{M}$	mass matrix
n, n_1, n_2	stress exponent
N	number of cycles
N_f	number of cycles to failure
N_{f0}	number of cycles to crack nucleation
p	material parameter
q	(vertical) distributed load
Q	activation energy
r	distance from the crack tip
R	radius of curvature
R_c, R_{DC}, R_R	resistance of coil, daisy chain component, and external resistor
s	exponent, or deformation resistance
s^*	saturated value of the deformation resistance s
$\hat{s}$	material parameter
S	surface of a PWB
t	time
T	absolute temperature, in Kelvin scale unless otherwise mentioned
T_{ave}	average absolute temperature during a thermal cycle
u_i	displacement in the direction $i = 1, 2, 3$ or $i = x, y, z$
$\boldsymbol{u}$	displacement vector
u_g	general solution to a differential equation
u_F	particular solution to a differential equation
ur_i	rotation around the axis $i = 1, 2, 3$ or $i = x, y, z$
U	strain energy
$\boldsymbol{U}$	vector of displacement amplitudes
U_e	excitation voltage
U_g, U_F	amplitude of a general solution and that of a particular solution
U_o, U_R	voltage across a measurement circuit and that over the external resistor
U_z	time-independent part of bending
U_t	time-dependent part of bending
V^e	volume of an element
w	strain energy density
Δw^e_{pl}	plastic energy in an element during a cycle
W	work done by external load
W_{pl}	plastic work
x_i	coordinate along the axis $i = 1, 2, 3$, typically $x_1 = x, x_2 = y$, and $x_3 = z$
$\dot{()} = d/dt$	derivative over time
$\ddot{()} = d^2/dt^2$	second derivative over time
α	material parameter
α_R	mass proportional damping coefficient
α_T	coefficient of thermal expansion
β_R	mass proportional damping coefficient
$\beta_1, \beta_2, \beta_3$	parameters

Δ	second derivative over spatial coordinates $\Delta = \partial^2/\partial x^2 + \partial^2/\partial y^2$, or a symbol of a range
ϵ^{tot}	total strain
ϵ^{el}	elastic strain
ϵ^{p}	time-independent plastic strain
ϵ^{pl}	plastic strain
ϵ^{cr}	creep strain
ϵ_{ef}	effective strain
ϵ_f	strain to failure
ϵ_{ij}	components of strain, $i = 1, 2, 3$ or $i = x, y, z$
ϵ_{vm}	von Mises strain
γ	shear strain
Γ	surface
λ	Lamé constant $\lambda = \nu E/[(1+\nu)(1-2\nu)]$
λ^{pl}	consistency parameter
ν	Poisson ratio
ω_d	circular frequency
ω_F	circular frequency of a harmonic load
ω_n	natural circular frequency
ϕ	phase angle
Π	potential energy
ρ	density
σ	stress
σ_{ef}	effective stress
σ_{ij}	components of stress, $i = 1, 2, 3$ or $i = x, y, z$
σ_{vm}	von Mises stress
σ_Y	yield strength
τ_{max}	maximum shear stress
θ	bending angle
ξ	material parameter
ζ	material parameter

1 Introduction

Portable electronic devices are subject to accidentally being dropped, which makes the mechanical reliability of solder interconnections under shock loads an important issue for the manufacturers of electronics. Reliability can be defined as the ability of a product to operate without failure under a set of predetermined conditions over a specified period of time [81Mil]. Good reliability makes customers more satisfied with the manufacturer thereby affecting the market shares. The reliability under shock loading conditions is currently being studied by employing drop tests, where a high impact loading is generated by letting test structures fall a specified distance and hit a strike surface. Tests carried out with commercial products show that the generated strong acceleration pulse (or deceleration) makes circuit boards, which are inside the products, to bend and vibrate excessively and rapidly [02Lim, 01Low, 05Tan, 98Wu]. The vibration generates stresses in components and interconnections and, hence, causes failures.

When products are tested, the number of factors affecting the vibration and, thereby, the number of drops to failure is large, and many of the factors are independent of the properties of components. For example, the covers of the product, the mounting of the circuit boards to the body of the product, the mechanical properties of the boards, and the orientation of the product at the moment it hits the solid ground have strong effect on the vibration of the circuit boards. Therefore, in order to reduce the number of factors, a drop test standard for testing the reliability of component boards has been developed [03Jed] (the JEDEC JESD22-B111 drop test standard). Drop testing of component boards has been studied extensively over the past few years [05Ala, 05Cho, 05Mat, 98Mei, 00Ong, 03Tee, 05Zen], and it has been found out that the response of the board to the impact can be very complex. The vibration of boards consists of different bending modes, and each mode vibrates at a specific frequency. This vibratory bending induces stresses in interconnections in the same way as in static bending: components resist the bending of boards, and the interconnections between the components and the boards carry the induced loads. Surface mounted components are often light-weighted, and hence, it is reasonable to expect that the primary source for the stresses in the interconnections is the fast

vibration of circuit boards, not the inertia forces of the components, even though the acceleration can be very high.

In drop-tested component boards cracks are usually located in the reaction layers of the interconnections on the component or board side or in circuit boards [05Ala, 02Arr, 05Cho, 04Lal, 06Mat1], but in slow cyclic loading (thermomechanical cycling) cracks are located mainly in solder. The difference in crack paths results from the temperature and strain rate dependency of the mechanical properties of solders. As compared to other metals, one significant difference in solders is their low melting temperature. The melting temperature T_m of tin is 505 K (232 °C), while that of copper and iron are 1356 K (1083 °C) and 1809 K (1537 °C) [61Met]. Commercial solders are mainly tin-based alloys. Most of the alloying metals reduce the melting temperature of the pure tin; the melting point of the eutectic SnAgCu solder is 490 K (217 °C). At high homologous temperatures ($> 0.4 - 0.5\ T_m$ in Kelvin) the strain rate and temperature affect significantly the mechanical properties and behaviour of metals and alloys [82Fro]. For common solders operational temperatures are well over the half of their melting temperatures, and the plastic properties depend significantly on temperature and strain rate. Because the strength of solders increases strongly with increasing strain rate and decreases strongly with increasing temperature [02Ama, 92Dar, 82Fro, 65Gar], the stress levels in solder interconnections are significantly higher in drop tests than in thermal cycling tests. The increase in the stress levels leads to the observed differences in the crack paths. Thus, when the reliability of solder interconnections is being studied, there are three important testing conditions that should be close to those of the loading conditions of real products: loading magnitude, temperature, and loading rate. Otherwise the mechanical behaviour of solders in tests may differ from that in use, and the loading may be overestimated (or underestimated) causing failure modes that are unimportant.

In drop testing, if the drop height is suitable, the loading rate and the magnitude are close to what devices experience. However, drop testers (a schematic graph in Fig. 1a) are not versatile test devices, and are somewhat impractical when studying which parameters affect the reliability. The strong impact stresses the test apparatus also, causing measurement cables and standoffs to fail occasionally. Controlling the

environmental temperature, for example, is difficult because of the long distances test assemblies fall and the effects of temperature on the bearings and the strike surface. In addition, the bending of test assemblies is complex, which makes the mechanical analysis of drop testing challenging. Mechanical analysis (by the finite element method, FEM) is needed in evaluating how heavily the interconnections are stressed during tests, because measuring the deformations or stresses in the interconnections is impossible due to the sizes and locations of the interconnections. In addition, FE analysis helps understanding what happens during a test, and how different kind of changes in the test conditions and in the layout of the test board affect the stresses.

In addition to applying a high impact load, the strong and rapid loading of interconnections can be generated by vibrating component boards at their resonance frequencies (a schematic graph of a test system in Fig. 1b). In drop tests the bending of boards is the primary source for the stresses in the interconnections, and hence, when the amplitude and frequency of bending in the vibration test are similar to those in drop tests, also the stresses should be similar. Thus, by adjusting the frequency and amplitude of the excitation, it should be possible to produce the same failure modes also. Moreover, the vibration test has some advantages over the drop test. Component boards do not travel during the vibration testing, which makes more versatile testing and measuring possible, and the measurement cables

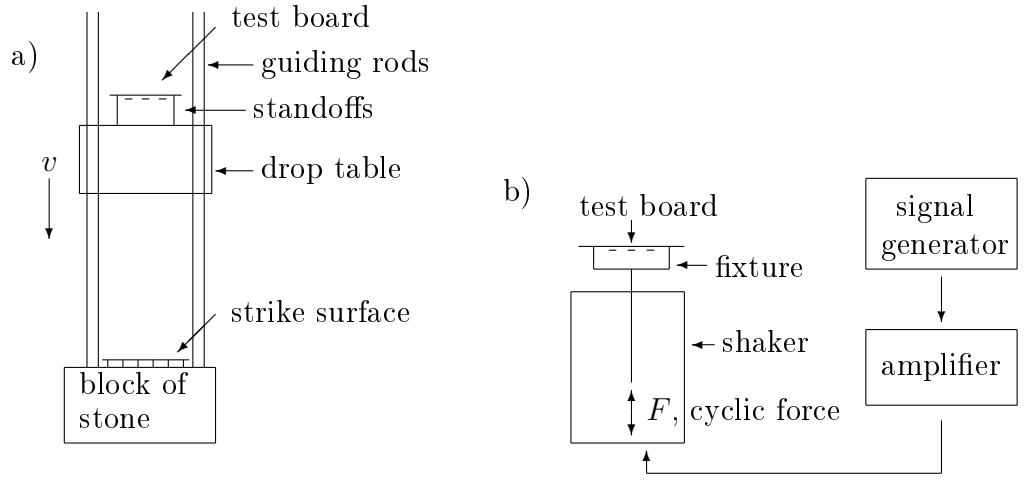

Figure 1 *Schematic graphs of a) the drop test apparatus and b) the vibration test system.*

are not strongly stressed. Testing at high temperatures is more feasible, because in the vibration test the test specimen can be put in a thermal chamber during the test, while the test apparatus is outside the chamber. By controlling the excitation and temperature, for example, the reliability can be studied in different loading conditions, which are closer to the real operational environment. In addition, when only one vibration mode is excited, the bending is less complex, and analysing stresses is easier. Moreover, vibration testing at resonant frequencies is fast. The resonance frequency of a JEDEC board is approximately 200 Hz, which means that 10 000 bending cycles can be carried out in one minute.

Vibration testing has been employed by car and aeroplane industry in order to qualify electronic components, but the magnitude of the loading has usually been rather small compared to that in drop testing. In drop tests the number of drops to failure is often small; for example, in the JEDEC drop test standard the number of drops to carry out has been limited to 30. On the contrary, in conventional vibration tests interconnections are loaded usually for significantly more cycles. For example, the vibration tests carried out by Lau *et al.* [90Lau] and Zhao *et al.* [00Zha] lasted for more than half an hour at frequencies of 50 Hz and above, i.e. more than 100 000 cycles. Hence, the stress levels in conventional vibration tests are significantly lower than in drop tests.

In this work vibration testing is used to produce severe loading of interconnections by vibrating component boards at their resonance frequency. The effects of the amplitude and frequency of the component board bending on the generated failure modes and stresses in the solder interconnections are studied, as well as the effects of strain rate and temperature on the strength of the solders. The vibration of the test assemblies in the JESD22-B111 drop test will be measured and compared to that in the vibration test. The observed failure modes of the solder interconnections will be compared. In addition, the loading of interconnections induced in the tests will be compared by carrying out FE analysis. The measurements and analyses will be used to determine whether the vibration test can be used in studying the reliability of solder interconnection under shock loads.

2 Surface mounted assemblies

The surface mount technology (SMT) has made possible the reduction of component sizes and an increase in interconnection densities. Unfortunately, the decrease in size makes the interconnections more prone to mechanical failure, because mechanical stresses, which are typically generated in interconnections when assemblies bend or expand due to changes in temperature, increase as the interconnection size is reduced (see (56), (65) and (69) on pages 31-34). Therefore, the mechanical reliability of solder interconnections has become an increasingly important factor in the design of electronic devices.

Nowadays the highest interconnection densities are obtained by employing area array interconnections, where interconnections are dotted in an array on the bottom of components. Typical area array component types are ball grid arrays (BGA), chip scale packages (CSP), and flip chips (FC). Flip chips are components (bare chips) which are directly connected to printed wiring boards (PWB) by soldering or using adhesives. In CSPs and BGAs a plastic package, which reduces stresses in interconnections, surrounds the chip. In this work most of the tests are carried out using only one BGA component type. Therefore, in the following sections interconnections are discussed from the BGA point of view.

2.1 Structure of solder interconnections

Solder interconnections connect the wiring of components to the wiring of circuit boards. On the component side solder is in contact with the under bump metallisation (UBM) layers and on the PWB side with the soldering pads; see Fig. 2. During reflow soldering process, solder melts and dissolves parts of the pad and the UBM. During solidification, as a result of chemical reactions on both interfaces, a strong metallurgical bond is formed on the board side between the solder and the pad and on the component side between the solder and the UBM. The composition and structure of the reaction layers depend on the materials used and significantly affects the mechanical properties of the layers. Especially in shock loading, the mechanical properties of the reaction layers are essential to the reliability of interconnections, because cracks are often located in or near the layers.

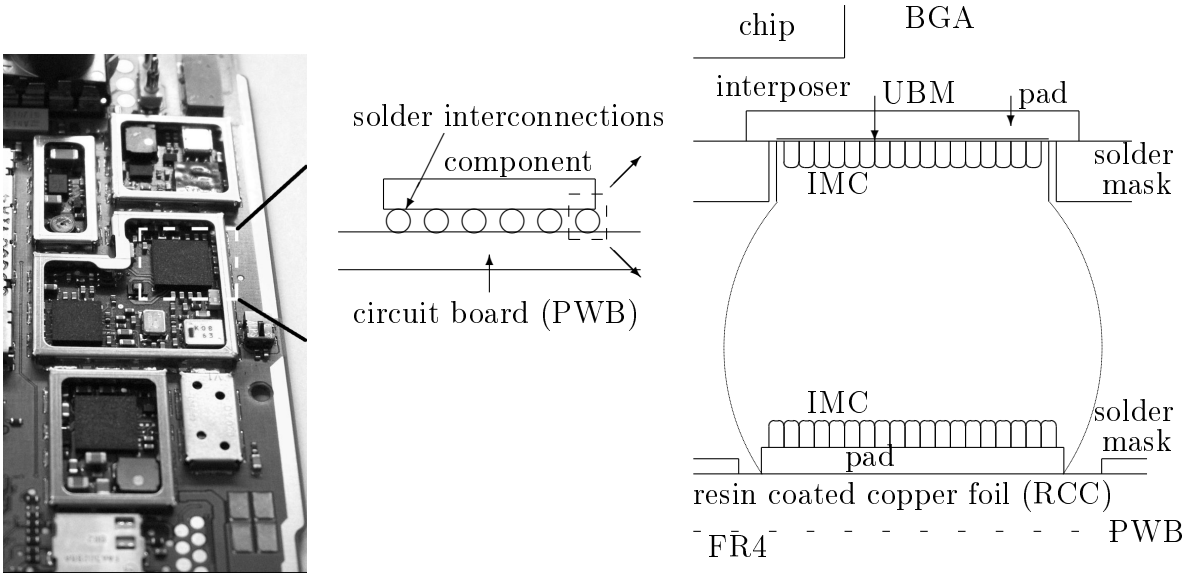

Figure 2 *Typical solder interconnection in BGA assemblies.*

The soldering pads on PWBs, as well as the wiring, are made of copper. During the manufacturing of PWBs a surface finish is applied to their surfaces to hinder the oxidation of copper pads and thereby to preserve the good solderability. The surface finishes that will be employed in this work are organic solderability preservative (OSP), electroless nickel with a very thin flash gold layer (NiAu), and matte tin (Sn). During soldering the OSP finish evaporates, allowing the solder to react with the copper pads, but the nickel in the NiAu finish remains on top of the copper pads and reacts with the solder. In the case of the Sn finish the same reactions should occur as in the case of the OSP finish, because most solders are tin-based alloys.

The reactions between tin and copper and tin and nickel have been studied extensively during recent years, [05Laur, 06Vuo2]. Here a very short summary is given. When tin is in contact with copper at elevated temperature, liquid tin will react with copper forming two intermetallic compounds (IMC): Cu_6Sn_5 and Cu_3Sn. After reflow soldering the thickness of the Cu_6Sn_5 layer is typically a few micrometres, the thickness of Cu_3Sn being much thinner due to its slower growth. With time more copper reacts with the tin, and the thickness of the IMC layers increases.

When tin is in contact with nickel, they form a Ni_3Sn_4 compound, which grows much slower than Cu_6Sn_5. When a Ni(P)|Au surface finish is produced chemically, the nickel bath contains phosphorus. Therefore, also the produced surface finish contains some amount of phosphorus (about 8 wt-% in this work). The remaining

phosphorus makes the reaction layer between tin and the surface finish very complex [02Mats, 06Vuo]. The amorphous layer (Sn, Ni, and P), which contains a large amount of tiny voids, is found to be brittle and often the primary cause of failures in drop tests [05Cho, 06Mat1, 98Mei].

It has also been found out that during a typical reflow soldering process copper from the pads on the PWB side can travel through the molten solder and take part in the reaction on the other side of the interconnection [01Kul]. Thus, one should always consider the whole interconnection when analysing the reaction layers.

In the solidified interconnections the bulk solder consists typically of a couple of colonies of different lattice orientation. Because plastic deformation is dependent on the lattice orientation with respect to loading, the limited number of grains affects the plastic properties of the interconnections. It has been estimated that at least 10 grains should exist in the direction of the deformation if the behaviour is expected to be independent of the number of grains [96Bon]. The measurements were carried out with 98Pb2Sn samples, which have a different microstructure from SnAgCu solders, but we assume that only small differences in the number of grains can be expected if the solder is changed to a lead-free one. In addition to the plastic properties, the number of grains also affects the propagation of cracks. There is usually more impurities on grain boundaries than in grains, which affects the mechanical properties of the boundaries. It has been found out that under thermal cycling cracks propagate in solder along grain boundaries [04Mat]. Hence, grain boundaries may have influence on the nucleation and propagation of cracks in drop tests also. Altogether, a small amount of grains is expected to increase scatter in the reliability of interconnections.

2.2 Evolution of microstructures

After solidification, the microstructure of the interconnections changes gradually. Typical changes are the growth of the reaction layers, the coarsening of the microstructure, and the recrystallisation. Of these phenomena the recrystallisation affects the mechanical properties of solders the most, but it does not always take place. The growth of the IMC layers, IMC particles in the bulk solder, and grains is thermally activated. The recrystallisation is also thermally activated, but a certain

minimum amount of plastic deformation is needed for the initiation of recrystallisation. The plastic deformation of solder materials increases dislocation density in grains, which may initiate recrystallisation locally. During the recrystallisation in areas of major deformation, the nucleated new grains grow by consuming the deformed areas, and the dislocation density reduces. Hence, the recrystallisation reduces the strength of strain-hardened solder and produces more grain boundaries. After the recrystallisation the area of grain boundaries is large, and the grains start to grow in order to reduce the interfacial free energy associated with the grain boundaries. The growth of IMC-layers, IMC particles, and grains and the recrystallisation have Arrhenius-type temperature dependency. The rate of grain growth, for example, is

$$\frac{dD}{dt} = D \exp(-Q/kT) \tag{1}$$

where D is the grain diameter, Q is the activation energy, k is the Boltzmann constant, and T is the absolute temperature. The chemical reactions in the interconnections are slow at room temperature, but the thickness of the reaction layers will increase more rapidly when the interconnections are heated up. The IMC layers become more continuous layers, and their thickness increases.

In addition, during annealing a large number of tiny voids has been observed to form in the Cu_3Sn layer along the copper interface in some cases [05Laur, 06Mat1, 05Zen]. It has been proposed that the voids are Kirkendall voids that are generated because of the different diffusion rates of copper and tin atoms. Impurities have been found to influence the phenomena significantly [05Laur]. The voids provide a weak layer for cracks to propagate, and they have been observed to reduce the number of drops to failure [06Mat2].

The evolution of the microstructure takes too long for having importance during shock loading tests, but it may occur before a functional device is loaded by an impact or between two impacts. For example, electronic equipment are under cyclic thermomechanical loading because of the heat generated by components. Thus, the microstructures of solder interconnections and their mechanical properties may have changed significantly before and between accidental drops.

3 Mechanical properties and behaviour of solders

Deformation of metals is discussed more thoroughly by Dieter [86Die] and Lemaitre and Chaboche [90Lem], for example. Deformation can be divided into reversible and irreversible parts, depending on whether a structure does or does not return to its original form after the loading is removed. The reversible part is known as elastic deformation and the irreversible part as plastic deformation. During elastic deformation the magnitude of the strain is usually very small: strains in structural metals are mainly elastic up to values from 0.1 % to 0.2 %, above which plastic deformation becomes dominant. In common solders the elastic deformation is usually even smaller [04Put]. Plastic deformation is irreversible, and is often considered instantaneous and not dependent on time. However, when a loading is applied over a long period of time or at high homologous temperatures ($> 0.4 - 0.5\ T_m$), plastic strain usually increases with time, which is called creep. Thus, assuming small strains, the total strain is the sum of the three parts

$$\epsilon^{tot} = \epsilon^{el} + \epsilon^{pl} = \epsilon^{el} + \epsilon^{p} + \epsilon^{cr} \tag{2}$$

where ϵ^{tot} is the total strain, ϵ^{el} is the elastic part, ϵ^{pl} is the plastic strain, ϵ^{p} is the time-independent plastic strain, and ϵ^{cr} is the creep strain.

When the homologous temperature of a material is low, the three deformation types can be separated rather easily, but at high homologous temperatures time-dependent deformation mechanisms become faster, and the division of plastic deformation into the time-independent and time-dependent parts is not straightforward. In most applications of solders their homologous temperatures are high, and thus plastic deformation is strongly dependent on the strain rate.

3.1 Elastic deformation

During ideal elastic deformation the distances between atoms change, and after the loading the interatomic forces return the atoms to their initial positions. In practise, a small fraction of atoms is also displaced permanently because of inherent defects in material, but on the macroscopic scale that does not cause noticeable permanent deformation.

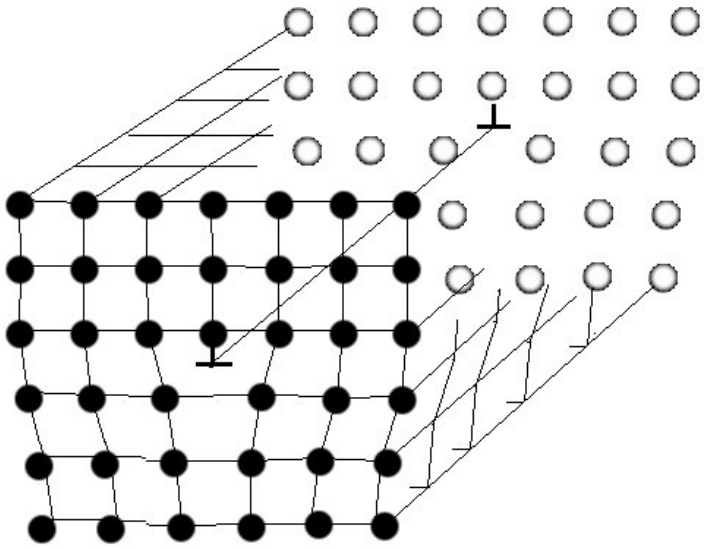

Figure 3 *Edge dislocation in a cubic crystal.*

3.2 Plastic deformation

Plastic deformation of crystalline materials, like metals, is carried out by dislocations, which are line defects in the crystal structure. In Fig. 3 an edge dislocation is presented. During plastic deformation dislocations slide along slip planes, the number and orientation of which depends on the crystal structure. The dislocation in Fig. 3 would slide horisontally to left or right, depending on the loading. Once started, dislocations slide to the surface of the grain under constant loading, unless they meet obstacles. The stress required for dislocations to move depends on several factors: for example, solute atoms, other dislocations, and precipitates hinder dislocation motion. These features, except the dislocation density, are considerably stable. The dislocation density, however, increases rapidly as plastic strain increases, which leads to strain-hardening of materials as dislocations start to hinder the movements of each other. In addition, in some grains plastic deformation starts earlier than in others, because of the orientation of the grains with respect to the loading, but the deformation of those grains cannot continue long unless the neighbouring grains deform also. Hence, the material strengthens as plastic strain increases.

The amount of strain-hardening and plastic strain before rupture varies considerably between different materials and depends largely on the deformation history of the specimen. For example, for pure aluminium the yield strength for an annealed

specimen is 12 MPa, the tensile strength is 47 MPa, and the elongation to rupture is 60 %, but if tests are carried out with a cold-rolled specimen (reduction in the thickness 75 %) the values are 106 MPa, 112 MPa, and 5 % [61Met].

The number of dislocations in metals is huge usually. When the lengths of dislocations in a cubic centimetre are summed up, the value is typically from 10^4 to 10^{10} centimetres; this corresponds to about 0.005-5000 m in an interconnection that is 500 μm in diameter. In solder interconnections some dislocations are formed during solidification and others during deformation. Thus, there is always a large number of dislocations to take care of or to hinder plastic deformation.

At high temperatures vacancies have a strong effect on the plastic behaviour of metals. A vacancy is a point defect in the crystal structure: a lattice location where an atom should be but is not. The strain fields around edge dislocations make vacancies to move towards the core fields of dislocations. Vacancies replace atoms from the extra plane of edge dislocations making dislocations to climb, which helps dislocations to pass obstacles. The climb of dislocations becomes faster at high temperatures, because of the more rapid diffusion of vacancies. Climb is also needed in the annihilation of dislocations, where two dislocations of opposite sign annihilate each other. The number and diffusion rate of vacancies depend largely on temperature, hence plastic deformation becomes largely rate- and temperature-dependent at high homologous temperatures.

Increasing dislocation density increases the internal energy of metals. In order to reduce the energy, metals start to restore gradually by two mechanisms: recovery and recrystallisation. The latter has been shortly described in Chapter 2.2. The recovery processes (the annihilation process *etc.*) depend strongly on temperature. During the restoration processes the dislocation density reduces, and also the strength of metals decreases. Hence, at high homologous temperatures, where the restoration is fast, plastic deformation is strongly dependent on the strain rate.

When the strain rate is very high, as in drop tests, another deformation mechanism, twinning, may also take place. Twinning means that adjacent atomic layers move vis-á-vis each other generating homogeneous deformation. The twinning deformation is very fast but requires high strain rates and low temperatures. Twinning has been found in drop tested specimens [06Mat1, 05Rei].

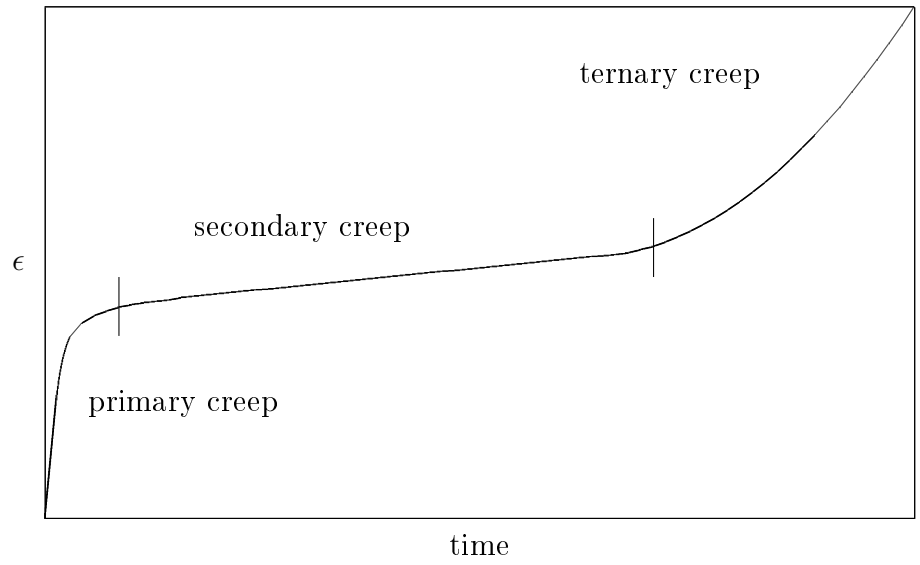

Figure 4 *Creep stages.*

3.2.1 Creep stages

One way to test the creep properties of materials is to apply a constant stress to a test specimen and to measure the elongation as a function of time. Generally, three stages can be observed in these types of creep curves: primary, secondary, and ternary creep; see Fig. 4. During the primary creep the strain increases rapidly, and the strain rate decreases from the initial rate to the constant rate of the secondary creep. If the plastic deformation during the application of the loading is small, dislocations move easily at the beginning of the loading, but as their density increases the strain rate slows down to a constant value, see Fig. 5. During the secondary creep the recovery processes are so rapid that continuous deformation is possible without an increase in the stress. During the ternary creep the number and size of

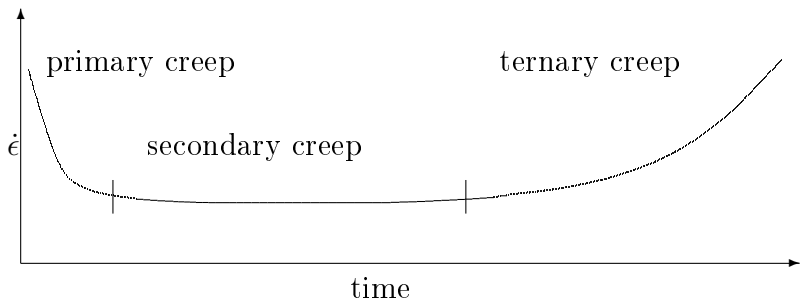

Figure 5 *Creep rate under constant load as a function of time.*

microcracks in specimens increase, increasing stresses in undamaged areas, which leads to the observed increase in the strain rate.

3.3 Constitutive equations

When the stresses and strains of solders under plastic deformation at high homologous temperatures are analysed, strain rate is a very important factor, and the absolute value of strain merely describes which of the three stages of creep the solder is in. Thus, the equations of plastic deformation are formulated using strain rates instead of strains. Strain is more useful under elastic deformation and under plastic deformation at low temperatures.

3.3.1 Three-dimensional stress state

Elastic deformation in three dimensional loading can be accurately calculated by dividing the loading into its components, and superimposing the responses of the material to each component – as long as the strains and displacements are small. On the contrary, calculating plastic deformation is not as simple. The onset of plastic deformation depends on all the stress components, and the direction of plastic strain is not necessarily the same as that of the loading (edge dislocations slide along slip planes). The computation of stresses and plastic strains is discussed extensively in literature [90Lem, 69Mal, 98Sim]. The von Mises and Tresca yield criteria are often used to calculate whether a loading causes plastic yielding or not. For most metals the "right" criterion would be something between these two. According to the criteria, material yields, if the effective stress exceeds the yield strength of the material. The yield strength can be measured in unidirectional loading. The criteria can be expressed in the form

$$f = \sigma_{ef} - \sigma_Y = 0 \tag{3}$$

where f is the yield function, σ_{ef} is the effective stress, and σ_Y is the yield strength of the material in uniaxial tension. Plastic yielding occurs when $f = 0$. The formula of the effective stress depends on the yield criterion.

The von Mises stress is derived by calculating the energy that distorts the shape,

and it's formula is

$$\sigma_{vm} = \sqrt{0.5\left[(\sigma_x - \sigma_y)^2 + (\sigma_y - \sigma_z)^2 + (\sigma_z - \sigma_x)^2\right] + 3\left[\tau_{xy}^2 + \tau_{yz}^2 + \tau_{zx}^2\right]} \quad (4)$$

and the corresponding effective strain is

$$\epsilon_{vm} = \sqrt{2/9\left[(\epsilon_x - \epsilon_y)^2 + (\epsilon_y - \epsilon_z)^2 + (\epsilon_z - \epsilon_x)^2\right] + 4/3\left[\gamma_{xy}^2 + \gamma_{yz}^2 + \gamma_{zx}^2\right]} \quad (5)$$

The effective strain is calculated so that the work done in multiaxial loading is equal to the work done in a uniaxial load by the effective stress

$$\sum_i \sum_j \epsilon_{ij}\sigma_{ij} = \epsilon_{vm}\sigma_{vm} \quad (6)$$

where $i, j = 1 \ldots 3$, $\epsilon_{11} = \epsilon_x, \epsilon_{12} = \frac{1}{2}\gamma_{xy}, \ldots, \sigma_{11} = \sigma_x, \sigma_{12} = \tau_{xy}, \ldots$.

In some cases the maximum shear stress describes the plastic behaviour of metals better, and it is called the Tresca stress:

$$\tau_{max} = \frac{1}{2}\max\{|\sigma_1 - \sigma_2|, |\sigma_2 - \sigma_3|, |\sigma_3 - \sigma_1|\} \quad (7)$$

where σ_i are the principal stresses, and $\sigma_{ef} = 2\tau_{max}$. Thus, if a material yields in uniaxial tension, when $\sigma = \sigma_Y$, then the shear stress that causes yielding is $\tau_{xy} = \sigma_Y/\sqrt{3}$ according to von Mises and $\tau_{xy} = \sigma_Y/2$ according to Tresca. According to both criteria, yielding is independent of pressure, which is typical for metals. From (7) one can also conclude that the magnitude of the largest tensile stress is always larger than or equal to the largest shear stress.

The direction of the plastic strain is usually computed by the formula

$$d\epsilon_{ij}^{pl} = \lambda^{pl}\frac{\partial f}{\partial \sigma_{ij}} \quad (8)$$

where the consistency parameter λ^{pl} describes the magnitude of the strain increment, f is the yield surface, and the gradient $\partial f/\partial\sigma_{ij}$ is the direction of the plastic strain. The yield surface $f = 0$ has sharp corners in the case of the Tresca criterion, which complicates the computation of the gradient. Therefore, the von Mises criterion is used more often, and was used in this work also.

3.3.2 Elastic strain

In metals elastic deformation is relatively small. The amount of elastic strain is related to the applied loading as described by the generalised Hooke's law

$$\epsilon_x^{el} = [\sigma_x - \nu(\sigma_y + \sigma_z)]/E \tag{9a}$$

$$\gamma_{xy}^{el} = \tau_{xy}/G \tag{9b}$$

or

$$\sigma_{ij} = \sum_k \sum_l D_{ijkl}\epsilon_{kl}^{el} \tag{9c}$$

where ϵ_x^{el} is the elastic tensile strain in the direction of the x axis, σ_x, σ_y and σ_z are the tensile stresses in the directions of the x, y, and z axis, ν is Poisson ratio, E is the elastic modulus, γ_{xy}^{el} is the elastic shear strain, τ_{xy} is the shear stress, and G is the shear modulus. Strains in the directions y and z are expressed by replacing the subscripts. On the last row the six equations for $\sigma_x, \cdots, \tau_{yz}$ are given in a matrix form: $i, j, k, l = 1 \ldots 3$ represent the coordinate axes, $\sigma_{11} \equiv \sigma_x$, $\sigma_{12} \equiv \tau_{xy}$ etc., and D_{ijkl} is the elasticity matrix.

3.3.3 Plastic strain

At low temperatures the magnitude of plastic deformation is often described with the equation

$$\epsilon_{ef}^{p} = C_1 \left(\frac{\sigma_{ef}}{E}\right)^{n_1} \tag{10}$$

where ϵ_{ef}^{p} is the effective strain (see Chapter 3.3.1), σ_{ef} is the effective stress, E is the elastic modulus, and C_1 and n_1 are material parameters. The model is independent of the strain rate, as is usually the case for plastic deformation at low temperatures. In FE programs there is usually the possibility of giving the constants C_1 and n_1 at different temperatures, and sometimes also at different strain rates, which makes the model better suited to describing the primary stage of creep.

A large number of equations to describe plastic deformation at high temperatures have been developed. Usually different equations are used for the primary and secondary stages of creep, while for the ternary stage a damage evolution model should be included. A typical equation for the secondary stage strain rate is of the

form

$$\dot{\epsilon}_{ef}^{pl} = C_2(\frac{\sigma_{ef}}{E})^{n_2} \exp(-Q/kT) \tag{11}$$

where C_2 is a constant, n_2 is the stress exponent, Q is the activation energy for the deformation process, k is the Boltzmann constant, and T is the absolute temperature [04Put]. This type of equation fits well with measurements within such a strain rate range, where one mechanism controls the deformation rate. The value of the stress exponent n_2 depends on the deformation mechanism. Therefore, if good fit to measured data is achieved with different values of n_2 in different strain rate ranges, it implies that the deformation mechanism is different between the ranges. Typical values of n_2 were collected by Langdon [82Lan]. Constant C_2 depends on microstructural features, and can be expressed with the formula

$$C_2 = C_3 \frac{Gb}{kT} \left(\frac{b}{D} \right)^{C_4} \tag{12}$$

where G is the shear modulus, b is the length of the Burgers vector, D is the grain size, k is the Boltzmann constant, T is temperature, and C_3 and C_4 are constants [82Lan].

In order to cover a wider strain rate range, the formula

$$\dot{\epsilon}_{ef}^{pl} = C_5 \sinh^n(C_6\sigma_{ef}) \exp(-Q/kT) \tag{13}$$

can be used, where C_5 and C_6 are constants, [65Gar]. Because (13) is used to cover a large range of strain rates, there can be more than one deformation mechanism active. Thus, the parameters are not related to the deformation mechanisms as they are in (11). However, for FE analysis the form (13) is more suitable because of the wider range of strain rates it covers.

Equations (11) and (13) relate stresses to strain rates during the secondary creep stage. In order to include the major hardening during the primary stage of creep, Anand & Brown [87Ana] proposed that C_6 in (13) is a function of an internal variable

s called deformation resistance

$$\dot{\epsilon}_{ef}^{pl} = C_5 \sinh^n(C_6\sigma_{ef}) \exp(-Q/kT) \tag{14a}$$

$$C_6 = \xi/s \tag{14b}$$

$$\dot{s} = \left[h_0 \left|\left(1 - \frac{s}{s^*}\right)\right|^a \operatorname{sign}\left(1 - \frac{s}{s^*}\right)\right] \dot{\epsilon}_{ef}^{pl} \tag{14c}$$

$$s^* = \hat{s} \left[\frac{\dot{\epsilon}_{ef}^{pl}}{C_5} \exp\left(\frac{Q}{kT}\right)\right]^{\zeta} \tag{14d}$$

where ξ, h_0, a, $\hat{s}$, and ζ are material parameters, s is the deformation resistance, $\dot{s}$ the evolution rate of s, and s^* is the value of s during the secondary stage. The deformation resistance is used to capture the dependence of the flow stress on the dislocation density. The equation of the deformation resistance could be modified to include the effect of static recovery (when $\dot{\epsilon}^{pl} = 0$) as explained by Anand, but that is not usually done.

3.4 Predicting the failure time

In the following chapter a few formulae for the computational prediction of the lifetime are presented. From the formulas it is determined, what are the most essential test parameters that should be similar in the drop and vibration tests. Chapter 3.4.1 considers cases, where plastic deformation is small, and Chapter 3.4.2 discusses the equations that have been developed for predicting the lifetime of solder interconnections under thermal cycling. The lifetime prediction of solder interconnections in shock loading conditions, which is studied in few articles only, is discussed in Chapter 3.4.3.

3.4.1 Models for lifetime prediction of elastoplastic materials

The presentation here follows that written by Anderson [94And] and Dieter [86Die]. The earliest failure analyses considered elastic materials. If a small elliptical crack appears in a large plate (plate dimensions much larger than crack length) loaded with a uniform uniaxial load σ perpendicular to the crack (Fig. 6), the stresses in front of the crack tip in the crack plane are

$$\sigma_x = \sigma_y = \frac{\sigma\sqrt{a}}{\sqrt{2r}} = \frac{K_I}{\sqrt{2\pi r}} \tag{15}$$

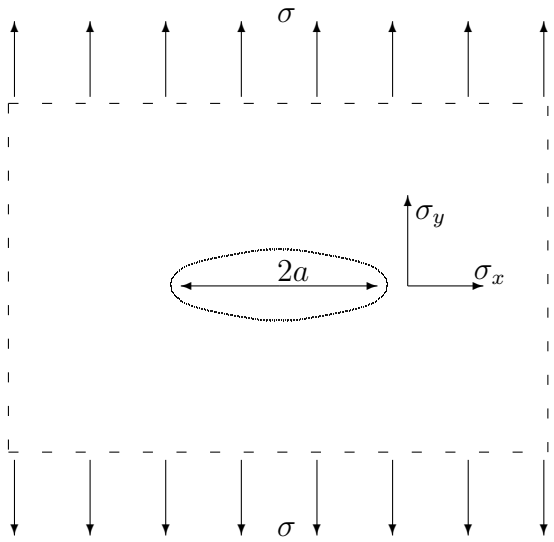

Figure 6 *Elliptical crack in a plate under uniform stress.*

where x is the direction of the crack, y is the direction of the loading, a is the half of the crack length, r is the distance from the crack tip, and K_I is the stress intensity factor. According to Irwin [57Irw], the energy release rate of the crack is

$$\mathcal{G} = \frac{\pi\sigma^2 a}{E} \tag{16}$$

where E is the elastic modulus, a is the half of the crack length, and σ is the applied stress. When the energy release rate exceeds a critical value $\mathcal{G}_c$ the material fails.

$$\mathcal{G}_c = \frac{\pi\sigma_f^2 a_{cr}}{E} \tag{17}$$

Thus, the failure stress σ_f varies with $1/\sqrt{a_{cr}}$, where a_{cr} is the half of the crack length at the moment of failure. When the formulae (16) and (15) are compared the relation $\mathcal{G} = K_I^2/E$ can be obtained.

Under cyclic loading crack propagation has been found to correlate with Paris' law

$$\frac{da}{dN} = C_7(\Delta K)^{C_8} \tag{18}$$

where da/dN is the crack growth rate, C_7 and C_8 are the material parameters, and ΔK is the stress intensity range. According to (15), stresses close to crack tip increase to infinity, which explains why cracks in some materials, such as glass, propagate very quickly. It has also been found out that the value of the mean stress has an important effect on the lifetime in cyclic loading.

Plastic deformation in front of the crack reduces stresses and hinders crack propagation. Therefore, the formulae (15) and (18) are not usually valid. Better results were obtained by Rice [68Ric], who used an energy based approach, in which the energy released by crack propagation is calculated within a volume in front of the crack tip.

$$J = -\frac{d\Pi}{dA} = -\frac{d(U-W)}{dA} \tag{19}$$

where J is the energy released, A is the crack area, and Π is the potential energy, U is the strain energy, and W is the work done by the external load. The value of J depends on the volume that is included in the calculation, but by changing the volume integral to the surface integral (20) the dependence can be avoided:

$$J = \int_{\Gamma} \left(w dy - T_i \frac{\partial u_i}{\partial x} ds \right) \tag{20}$$

where Γ is an arbitrary surface around the crack tip, w is the strain energy density, T_i are the components of the force on the surrounding surface Γ, u_i are displacements, x is the direction of the crack, y is the direction perpendicular to the crack, and s is the coordinate along the surface Γ. Here it is assumed that the structure and the crack have a unit thickness. The energy released by crack opening is then used to calculate the propagation of the crack. Solders, however, are soft and ductile at low strain rates, and the formulae (15)-(20) are not applicable.

3.4.2 Lifetime prediction of solder interconnections under thermomechanical loading

Plastic deformation dominates the behaviour of solders under use conditions. Because of the high homologous temperatures ($T > 0.4\,T_m$), strain rate and loading time have a significant effect on the amount of plastic deformation and, therefore, to the lifetime. Because the formulae (15) - (20) depend mainly on the stresses, not strains, other methods for predicting the lifetime have been studied. Different methods for predicting the lifetime under thermomechanical loading has been reviewed extensively by Salmela [05Sal].

One type of approach to estimating the lifetime of solder interconnections is based on the Coffin-Manson formula (21), which was developed for tensile test specimens

under cyclic deformation.

$$N_f = C_9(\Delta\epsilon^{pl})^{C_{10}} \tag{21}$$

where N_f is the number of cycles to failure, $\Delta\epsilon^{pl}$ is the amplitude of plastic deformation, and C_9 and C_{10} are the material parameters. Engelmaier [83Eng] has done a lot of work with the formula in the case of solder interconnections in thermal cycling, and he has modified the formula to include the effects of temperature range and the length of the cycle time:

$$N_f = C_{11}\left(\frac{\Delta\gamma^{pl}}{2\epsilon_f}\right)^{1/C_{12}} \tag{22a}$$

$$C_{12} = C_{13} + C_{14}T_{ave} + C_{15}\ln(1+f) \tag{22b}$$

where $\Delta\gamma^{pl}$ is the average plastic shear strain amplitude, T_{ave} is the average temperature in the solder joint, and f is the loading frequency. $C_{11} - C_{15}$ and ϵ_f are parameters that depend on the solder material, the geometry of the interconnection, and, probably, on the properties of the component and PWB. In (22) only the average deformation of an interconnection is included. Thus, strain concentrations and interconnection shape are left out, which makes the parameters to dependend on the interconnection geometry. Thus, employing (22) is quite case-sensitive and requires expertise in the subject.

Another type of approach is to calculate the plastic work done during loading and to relate that to the failure time, as has been done by Darveaux [97Dar]. He proposed that the crack propagation path in an interconnection should be determined on the basis of stress analysis, and the average plastic work along this path would correlate with the lifetime of the interconnection. The average plastic work during a cycle (ΔW_{pl}) is calculated by the formulae

$$\Delta w_{pl}^e = \int \sigma_{ij} d\epsilon_{ij}^{pl} \tag{23}$$

$$\Delta W_{pl} = \frac{\Sigma_e \Delta w_{pl}^e V^e}{\Sigma_e V^e} \tag{24}$$

where σ_{ij} and ϵ_{ij}^{pl} are the components of stress and plastic strain and V^e is the volume of element e. The number of cycles after which cracks nucleate is predicted with the formula

$$N_{f0} = C_{17}(\Delta W_{pl})^{C_{18}} \tag{25}$$

where C_{17} and C_{18} are the model parameters and the propagation rate is given by

$$\frac{da}{dN} = C_{19}(\Delta W_{pl})^{C_{20}} \tag{26}$$

where C_{19} and C_{20} are the model parameters. Finally, the time to failure is

$$N_f = N_{f0} + \frac{a_{cr}}{da/dN} \tag{27}$$

where a_{cr} is the length of the determined crack propagation path. The model parameters $C_{17} - C_{20}$ depend on the solder material and the interconnection shape. When FEM is employed they also depend on the size of the element [97Dar].

There are also methods, which can be implemented in the FE code, that compute the propagation of cracks and the effect of the cracks on stresses. Damage tensors that affect calculated stresses and strains have been successfully employed for example by Ju *et al.* [96Ju] and Desai *et al.* [98Des]. In these type of models, one big problem is taking the initial microstructure and its evolution into account.

During long use times at high temperatures the microstructures of solder interconnections change. Mattila *et al.* [04Mat] found out that the recrystallisation preceded crack initiation lead-free BGAs under thermal cycling. However, none of the lifetime prediction models presented above take the microstructural evolution into account explicitly. However, the material parameters in (25), for example, may depend strongly on the microstructural evolution.

3.4.3 Lifetime prediction of solder interconnections under shock loadings

Lifetime prediction has different kind of challenges in drop testing and vibrational bending than in thermal cycling. When the loading excites several bending modes, as in drop tests, the stress analysis is difficult because of the complex bending behaviour of test boards. In addition, many types of failure can be detected in drop and vibration tests: cracks propagate in reaction layers on the component or board side of the interconnections, through copper traces on PWBs, and in the RCC layer below the soldering pads [05Ala, 02Arr, 05Cho, 04Lal, 05Mat]. Failures through bulk solder are not observed usually. Plastic deformation in reaction layers is very small, and therefore, either elastic fracture mechanics (equations such as

(15)) or the J-integral method might give good results in lifetime prediction. But RCC failure significantly complicates stress analysis, making accurate stress analysis almost impossible. However, good accuracy in the lifetime prediction of drop-tested assemblies has been obtained by Tee *et al.* [03Tee] by using the Coffin-Manson type equation

$$N_f = C_{21}\sigma_z^{C_{22}} \tag{28}$$

where σ_z is the maximum peeling stress, i.e. the maximum vertical tensile stress in interconnections. According to the formulae (15), (17), and (28), the stress values perpendicular to the crack paths have significant importance on the number of loading cycles to failure. Hence, the stresses generated in the vibration test should be close to those induced in drop tests, if the vibration test is going to be used instead of the drop test.

4 Dynamic loading

In addition to the mechanical properties of solders, which depend strongly on the strain rate (Chapter 6), the strong inertia forces, which the shock loading in drop tests generates, make the structural behaviour of test assemblies dependent on the loading rate. Therefore, an inspection of structural dynamics is needed. Inertia forces change the behaviour of structures considerably when compared to bending or thermal cycling tests, and the concepts of *natural modes* and *natural frequencies* become essential. Phenomena related to dynamic loading have been described more thoroughly by Tedesco *et al.* [99Ted], for example.

4.1 Equations of motion

From the mathematical point of view the main difference between slow cyclic bending tests and drop tests is the effect of inertia forces. If the vertical motion of a ball attached to a linear massless spring is measured (Fig. 7), the displacement u_z of the ball is described by the equation

$$F_s + F_c + F_I = F(t) \tag{29a}$$

$$ku_z(t) + c\dot{u}_z(t) + m\ddot{u}_z(t) = F(t) \tag{29b}$$

where $F_s = ku_z$ is the spring force, $F_c = c\dot{u}_z$ is the damping force, $F_I = m\ddot{u}_z$ is the inertia force, t is time, k is the spring constant, c is the damping coefficient, m is the mass of the ball, and F is the force applied to the ball.

In the case of slow displacements ($\dot{u}_z(t) \approx 0, \ddot{u}_z(t) \approx 0$) inertia forces are negligible and the displacement of the ball can be defined by the equation

$$ku_z(t) = F(t) \tag{30}$$

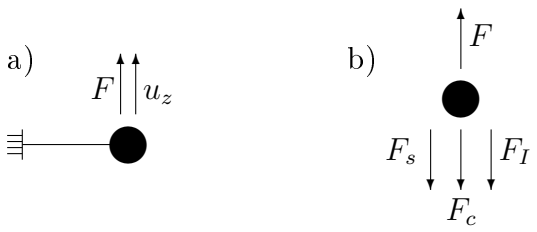

Figure 7 *a) A ball at the end of a spring. b) The forces acting on the mass.*

In shock loading, however, the inertia forces generate the bending that induces stresses in interconnections, and (30) is inapplicable. The equation of motion, (29), is a second order differential equation, and the solution can be divided into two parts:

$$u_z = u_g + u_F \tag{31}$$

where u_g is the general solution in the case where no force is applied ($F(t) = 0$, also called *free vibration*), and u_F is a particular solution in the case of the actual loading $F(t)$ (*forced vibration*). The general solution as a function of time is

$$u_g = U_g e^{st} \tag{32}$$

where U_g is the amplitude of the vibration, and s is obtained by substituting (32) into (29) when $F(t) = 0$:

$$\left(ms^2 + cs + k\right) U_g e^{st} = 0 \tag{33}$$

$$\Rightarrow s_{1,2} = \frac{1}{2m}\left(-c \pm \sqrt{c^2 - 4mk}\right) \tag{34}$$

The displacement oscillates only if the value of the damping factor c is less than the critical value $c < c_{cr} = 2\sqrt{mk}$. In this case the equation of the vibration is

$$u_g = U_g e^{-c/(2m)\, t} \sin(\omega_d t - \phi_g) \tag{35}$$

where ϕ_g is the phase of the displacement, and ω_d is the circular frequency of the motion

$$\omega_d = \sqrt{\frac{k}{m} - \frac{c^2}{4m^2}} = \sqrt{\frac{k}{m}}\sqrt{1 - \frac{c^2}{c_{cr}^2}} \tag{36}$$

The frequency of the motion f_d can be calculated by using the formula

$$\omega_d = 2\pi f_d \tag{37}$$

The values of U_g and ϕ_g in (35) depend on the initial conditions, but the frequencies ω_d and f_d depend only on the properties of the structure. In the special case of no damping ($c = 0$), the frequencies are called the *natural circular frequency* and the *natural frequency*

$$\omega_n = \sqrt{k/m},\ f_n = \frac{\sqrt{k/m}}{2\pi} \tag{38}$$

When a harmonic force $F(t) = F\sin(\omega_F t)$ is applied to the spring structure, the vibration is forced. Substituting the force $F(t)$ into (29) results in

$$u_F(t) = U_F \sin(\omega_F t - \phi_F) \tag{39}$$

where U_F is the response amplitude of the particular solution, and ϕ_F is the phase difference between the particular solution and the force. The resulting vibration is the sum of the general solution (free vibration) and the particular solution (forced vibration)

$$u_z(t) = u_g + u_F = U_g e^{-c/(2m)\,t} \sin(\omega_d t - \phi_g) + U_F \sin(\omega_F t - \phi_F) \tag{40}$$

The magnitude of the forced vibration amplitude, after the free vibration has been dampened away, is obtained by substituting u_F into (29)

$$U_F = \frac{F/m}{\left[(\omega_n^2 - \omega_F^2)^2 + (\omega_F\, c/m)^2\right]^{1/2}} = \frac{F}{k} \frac{\omega_n^2}{\left[(\omega_n^2 - \omega_F^2)^2 + (\omega_F\, c/m)^2\right]^{1/2}} \tag{41}$$

where F/k is the amount of displacement that a static force would generate. When the frequency of the force approaches the natural frequency of the structure, the displacement amplitude increases rapidly; see Fig. 8. In particular, if the value of the damping coefficient is very small, and the frequency of the force is close to the natural frequency of the structure, even a weak harmonic force generates large displacements (*resonance*).

Forced vibration at frequencies close to a natural frequency causes *beating* in structures whose damping coefficient is negligible. Beating results from the interference of two harmonic signals that have almost equal frequencies. In the formula

$$\sin\alpha - \sin\beta = 2\cos\left(\frac{\alpha+\beta}{2}\right)\sin\left(\frac{\alpha-\beta}{2}\right) \tag{42}$$

the left-hand side is similar to the right-hand side of (40). If the initial conditions of (40) are assumed to be $u_z(0) = \dot{u}_z(0) = F(0) = 0$, the displacement becomes

$$u_z(t) = U_F \left(\sin\omega_F t - \frac{\omega_F}{\omega_d} e^{-\frac{c}{2m}t} \sin\omega_d t\right) \tag{43}$$

When the circular frequencies ω_F and ω_d are close to each other and the damping is small, the multiplier $\omega_F/\omega_d \exp[-c/(2m)t] \approx 1$. Substituting this to (43) and using (42) the displacement can be written in the form

$$u_z(t) = 2U_F \cos\left(\frac{\omega_F + \omega_d}{2}\right) t \sin\left(\frac{\omega_F - \omega_d}{2}\right) t \approx 2U_F \cos\omega_F t \sin\delta t \tag{44}$$

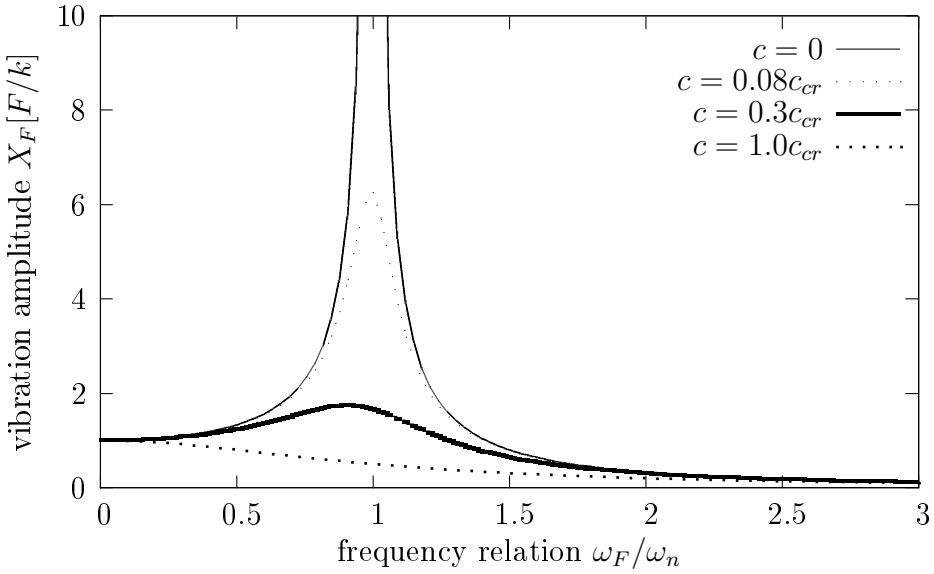

Figure 8 *Relative displacement amplitude as a function of the loading frequency when the damping c increases from 0 to the critical value* c_{cr}.

in which $\delta = 0.5(\omega_F - \omega_d)$ is small. The amplitude of the vibration $2U_F \sin \delta t$ changes slowly with time, and its maximum value is very large; see Fig. 9. If the damping is strong, beating is strongest at the beginning of testing.

Beating can easily be detected in FE analysis if a very small amount of damping is included in the computations. However, in the tests carried out in this work the only possible sign of beating is that the amplitude increases during the first periods to a maximum value that is slightly above the stabilised amplitude. When the bending amplitude is large, structural damping also becomes large, and beating is minimised.

Displacements of component boards and other complex structures are usually computed by employing FEM, in which structures are divided into elements. In this case there are a large number of coupled equations similar to (29), one equation for each direction in every node of an element mesh. The equations of the nodal displacements can be expressed in the matrix form

$$\boldsymbol{K}\boldsymbol{u}(t) + \boldsymbol{C}\dot{\boldsymbol{u}}(t) + \boldsymbol{M}\ddot{\boldsymbol{u}}(t) = \boldsymbol{F}(t) \tag{45}$$

where $\boldsymbol{u}$ is a vector of the nodal displacements, $\boldsymbol{K}$ is the stiffness matrix, $\boldsymbol{C}$ is the damping matrix, $\boldsymbol{M}$ is the mass matrix, and $\boldsymbol{F}$ is a vector of forces applied to the nodes.

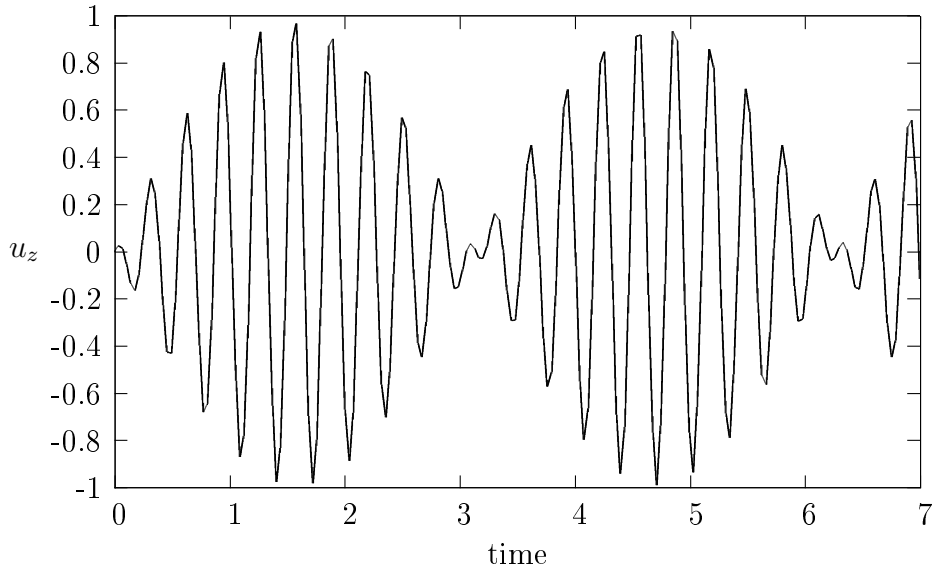

Figure 9 *Beating, calculated by setting* $\omega_F = 21,\ \omega_d = 19,\ U_F = 0.5,\ c = 0.01,$ *and* $m = 1$ *in (43).*

Damping in (29) and (45) depends linearly on the velocity, which is a very idealistic case. Structural damping is often caused by friction, plastic deformation, and the nucleation and propagation of cracks, phenomena that are not affected directly by the velocity itself. In addition, the air drag is usually not linearly dependent on the velocity. However, a high velocity usually implies large strains and displacements, because when a board vibrates at a certain frequency, increasing the velocity increases the amplitude and the strains. Therefore, linear damping with a damping coefficient that is fitted to the test can often be efficiently used in simulations. So-called *Rayleigh damping* is often implemented in FE programs. The damping matrix $\boldsymbol{C}$ is divided into mass-proportional and stiffness-proportional parts [00Aba1, vol. II, p. 12.1.1-2]

$$\boldsymbol{C} = \alpha_R \boldsymbol{M} + \beta_R \boldsymbol{K} \tag{46}$$

where high α_R values cause low-frequency motion to dampen quickly, while high β_R values dampen high frequency vibrations quickly.

4.2 Natural frequencies & modes

The natural modes of structures are determined by assuming no damping and no loading in (45); thus, the modes are the eigenvectors $\boldsymbol{u}$ of the problem

$$\boldsymbol{K}\boldsymbol{u}(t) + \boldsymbol{M}\ddot{\boldsymbol{u}}(t) = \boldsymbol{0} \tag{47}$$

and the corresponding natural circular frequencies are the eigenvalues of the problem.

$$\boldsymbol{u} = \boldsymbol{U}\sin\omega t \tag{48}$$

$$\Rightarrow(\boldsymbol{K} - \omega^2\boldsymbol{M})\,\boldsymbol{U}\sin\omega t = 0 \Rightarrow \omega_i \tag{49}$$

where ω_i are the natural circular frequencies of the structure. In principle, as (47) shows, no force is required for maintaining undamped vibration which is a sum of the natural modes. However, making the initial deformation requires loading; usually the higher the frequency of the mode, the more force is needed for an equally large amplitude. Moreover, in real situations, there is always some amount of damping to deaden the motion.

The natural bending modes of component boards depend on the geometry of the assembly: board geometry, supports, and the distribution of components. The natural frequencies, on the other hand, depend on the mode, the thickness and elastic modulus of the structure, and the mass. In multilayered boards the elastic properties of each layer and their distance from the middle plane also have an effect on the frequencies.

The equation of vertical displacements (z-direction) for isotropic homogeneous plates (assuming no damping) is expressed by

$$K\Delta\Delta u_z(x,y,t) = q_z(x,y,t) - \bar{m}(x,y)\frac{\partial^2 u_z(x,y,t)}{\partial t^2} \tag{50}$$

where $K = Eh^3/[12(1-\nu^2)]$ is the stiffness of a plate, $\Delta = \partial^2/\partial x^2 + \partial^2/\partial y^2$, q_z is a vertical loading, and $\bar{m} = m/A = \rho hA/A = \rho h$ is the mass m per unit area A [76War, page 231]. When the bending is expressed in time-independent and time-dependent parts

$$u_z(x,y,t) = U_z(x,y)U_t(t) \tag{51}$$

the governing equation for the bending modes becomes ($q_z = 0$)

$$\Delta\Delta U_z(x,y) - \frac{\bar{m}\omega^2}{K} U_z(x,y) = 0 \tag{52}$$

Analytical solutions for the static bending of rectangular plates freely supported at their edges (displacements prevented, rotations free) can be calculated by employing a series of sine functions (Navier's solution, [59Tim, page 108])

$$U_z(x,y) = \sum_{i=1}^{\infty}\sum_{j=1}^{\infty} U_{zij} \sin\frac{i\pi x}{L_x} \sin\frac{j\pi y}{L_y} \tag{53}$$

where L_x and L_y are the dimensions of the plate. Substituting (53) into (52) yields

$$\omega_{ij} = \pi^2 \left(\frac{i^2}{L_x^2} + \frac{j^2}{L_x^2} \right) \sqrt{\frac{K}{\bar{m}}} \Rightarrow \omega_{ij} \sim C_{ij} h \sqrt{\frac{E}{\rho}} \tag{54}$$

Thus, the natural frequency ($f_n = \omega_n / 2\pi$) depends linearly on the thickness h of the plate but only on the square root of the elastic modulus E or the density ρ. The natural frequency is the lowest in the case of $i = j = 1$, and the corresponding mode is a half sine wave in the x and y directions. Analytical solutions for plates having point supports, as in the JEDEC drop test setup, have not been calculated, but the effects of the thickness, the elastic modulus, and the density are the same.

4.3 Effects of nonlinearities

The equations above describe the behaviour of structures when displacements and stresses are small. Large displacements and strains generate different kinds of nonlinearities, which complicate the solution of dynamic problems. For example, large strains cause plastic deformation that invalidates the linear dependency of the spring force on the displacement ($F < kx$) and causes damping, thereby reducing the vibration frequency. Major bending during drop tests also generates tensile membrane stresses in boards, because the supports prevent horizontal movement, which changes the bending behaviour of the boards in a similar way to the tightening of guitar strings. The higher the tension, the higher the vibration frequency. He and Fulton [02He] have studied how the computed vibration of a PWB changes, if the geometrical nonlinearities that large displacements generate are taken into account in the FE analysis.

In the case of a beam that is under a tensile force F, the natural frequency depends on the force according to the formula [99Ted, page 458]

$$\omega_i = \left(\frac{i\pi}{L}\right)^2 \sqrt{\frac{EI}{\bar{m}}} \sqrt{1 + \frac{FL^2}{EIi^2\pi^2}} \tag{55}$$

where I is the second moment of area, L is the length, and $\bar{m}$ is the weight per unit length. Thus, a compressive force ($F < 0$) reduces the frequency and a tensile force ($F > 0$) increases it.

4.4 Drop testing

According to the JESD22-B111 standard [03Jed], test boards shall be fastened to a fixture from the corners, the deceleration of the fixture shall be a half sine pulse with the maximum of 1500 g_n, and the duration when the acceleration exceeds 10 % of the maximum shall be 0.5 ms. To generate such a short high-impact pulse, the fixture falls nearly one metre onto a thin rubber sheet on a rigid base. The frequency of the shock pulse is approximately 1 kHz; hence, only the natural modes that vibrate at about that frequency or slower should have an effect on the bending of the board. In principle, when a structure is loaded, all the natural modes take part in the vibration. In practise, the high-frequency modes have a negligible effect because of the effects of the loading frequency and the structural damping. The effect of the pulse shape on the response of a printed wiring board is studied by Suhir [02Suh], who concluded that the shape of the pulse does not have a significant effect on the amplitude of a mode, if the duration of the pulse is shorter than 12 % of the period of the natural mode. Component boards that are in accordance with the JEDEC standard typically have their first natural frequency close to 200 Hz. Thus, not only the energy and duration of the pulse but also its shape have some effect on the vibration.

4.5 Vibration testing

Bending amplitudes and frequencies that are similar to those generated during drop testing can also be generated if a periodic force is applied to test assemblies. The vibration is governed by equation (39), which is rewritten here

$$u_F(t) = U_F \sin(\omega_F t - \phi_F)$$

When the frequency of a periodic force is close to the natural frequency of a test assembly, the bending amplitude U_F increases to multifold values (see (41)) when compared to the value in static tests ($\omega_F = 0$); see Fig. 8 on page 26. At the same time the effect of other vibration modes can be minimised, because the mode whose natural frequency is closest to the loading dominates the vibration. For example, in the case of the ball spring system with damping $c = 0.08\, c_{cr}$, the amplitude reduces to one third of the resonance value when the loading frequency increases by 20 % from the resonance frequency (Fig. 8). Hence, by using the resonance frequency, the number of active modes is, in practise, limited to one, and the loading of the interconnections and the stress analysis are simplified.

4.6 Differences between thermal cycling and drop testing

The reliability of solder interconnections under thermal cycling has been widely studied. There are three major differences between thermal cycling and drop testing: the duration and magnitude of loading and the temperature range. Drop tests are carried out at room temperature, while during thermal cycling the temperature often raises to over 100 °C. High temperatures, together with a long loading time, make microstructural evolution possible during thermal cycling, but the duration of drop testing is too short for that.

In addition to gradual microstructural changes and the effects of temperature and strain rate on the behaviour of solder, the loading situation is somewhat different. Under thermal cycling interconnections are stressed because circuit boards and components expand to different extents when the temperature changes. Differences in thermal expansion generate mainly shear loading in interconnections, see Fig. 10. At low temperatures, where solder is rather strong, some amount of bending is also present. Nevertheless, the primary source of stresses is shearing. When components and board expand different amounts as a function of temperature, the amount of shear is according to a simple formula

$$\gamma = \Delta T(\alpha_{T,comp} - \alpha_{T,PWB})\frac{L}{h_{joint}} \tag{56}$$

where ΔT is the change in temperature, α_T is the coefficient of thermal expansion, *comp* and PWB refer to the component and printed wiring board, L is the distance

from a joint to the centre of the component (half of the component width), and h_{joint} is the height of the interconnection. Here, it is assumed that the solder is extremely soft and has no effect on the behaviour of the structure. In reality, stresses in interconnections prevent the free expansion of boards and components, and reduce shear deformation. In addition, large tensile stresses are also generated in solder bumps as they deform even though the loading is shearing (see (7), page 14).

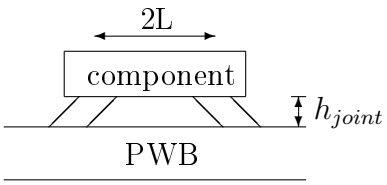

Figure 10 *Idealistic deformation of solder interconnections during thermal cycling.*

From the stress analysis point of view, power cycling (cyclic operational heating of active components) is similar. Stresses in interconnections are generated by the differences in thermal expansion of materials. In power cycling the changes in temperature are often smaller, and temperature is not as evenly distributed as in thermal cycling.

In drop and vibration tests the stresses in interconnections are generated primarily because of bending. The inertia forces of SMT components are typically small when compared to those of circuit boards, and hence, do not have a significant effect on stresses. Under bending the loading of the interconnections differs from that during thermal cycling, as the analysis below shows.

Consider the two-dimensional case in Fig. 11, where is shown a schematic graph of a rigid component mounted on the centre of a circuit board that is bended. In the figure h_{joint} is the height of the interconnections and h_{PWB} is the height of the circuit board. The solder is assumed to be extremely soft and, thus, the bending of the board does not bend the component. Drop tests are usually done in room temperature, and hence, the assumption is not accurate but makes the analysis easier to carry out. Before the board is bended the surface of the board is at level $S_0 = 0$, and during bending the surface follows $S(x)$. Thus, the elongation of the interconnections is $\epsilon(x)h_{joint} = -S(x) + S_0 = -S(x)$, where a positive sign

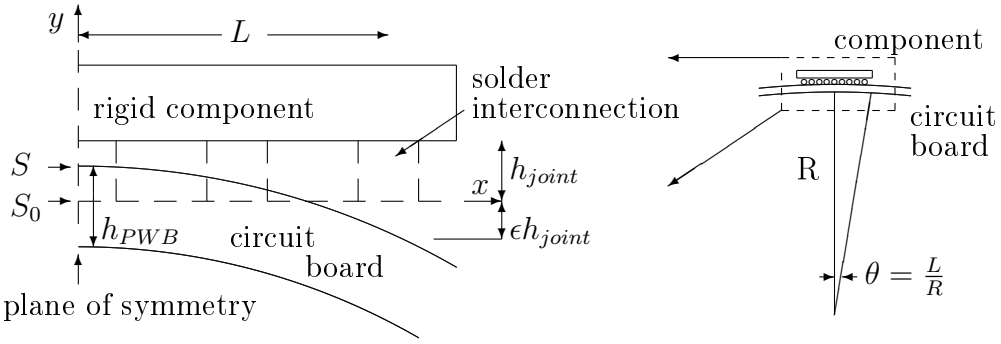

Figure 11 *Elongation of interconnections during bending.*

of $S(x)$ means displacement upward. Assume that *i*) the curvature of the PWB is constant (constant bending moment and soft interconnections), *ii*) the number of interconnections is large, *iii*) the interconnections are evenly distributed, and *iv*) the vertical stress in an interconnection depends on its elongation only. No external force is acting on the component and, therefore, the sum of vertical stresses in the interconnections must be zero $\sum F_y^{BGA} = \int \sigma_y dx = 0$. Hence, the elongation of the edge interconnections can be calculated with the formulae

$$\epsilon(x) h_{joint} = -S(x) + S_0 = -S(x) \tag{57}$$

$$S(x) = \sqrt{R^2 - x^2} + S_1 \tag{58}$$

$$\sum F_y^{BGA} = 0 \Rightarrow \int_0^L \sigma_y dx = \int_0^L \frac{-S(x)}{h_{joint}} E dx = 0 \tag{59}$$

$$\Rightarrow \int_0^L S(x) dx = \int_0^L (\sqrt{R^2 - x^2} + S_1) dx = 0 \tag{60}$$

$$\Rightarrow S_1 = -\frac{R}{2}\left(\sqrt{1 - \left(\frac{L}{R}\right)^2} + \frac{R}{L} \arcsin \frac{L}{R}\right) \tag{61}$$

$$\Rightarrow S(L) = \frac{R}{2}\left(\sqrt{1 - \left(\frac{L}{R}\right)^2} - \frac{R}{L} \arcsin \frac{L}{R}\right) \approx -\frac{1}{3}\frac{L^2}{R} \tag{62}$$

$$\text{where } \sqrt{1+x} = 1 + \frac{1}{2}x - \frac{1}{8}x^2 + \frac{1}{16}x^3 \cdots \tag{63}$$

$$\text{and } \arcsin x = x + \frac{1}{2}\frac{x^3}{3} + \frac{1 \cdot 3}{2 \cdot 4}\frac{x^5}{5} + \frac{1 \cdot 3 \cdot 5}{2 \cdot 4 \cdot 6}\frac{x^7}{7} + \frac{(2n-3)!!}{(2n-2)!!}\frac{x^{2n-1}}{2n-1} \tag{64}$$

$$\Rightarrow \epsilon(L) = \frac{-S(L)}{h_{joint}} = \frac{1}{3}\frac{L^2}{R}\frac{1}{h_{joint}} \tag{65}$$

where ϵ is the vertical tensile strain of the interconnections, $S(x)$ is the location of the PWB surface during bending, S_1 is a constant that depends on R, R is the bending

radius, F_y^{BGA} are the vertical loads acting on the component, L is the distance from the component centre to the the interconnection, and h_{joint} is the height of the interconnections. Here, as in the case of thermal cycling, the interconnections are assumed to be extremely soft, and $R \gg L$. In addition to elongation there is also shear deformation γ. If the middle plane of the board does not elongate during bending, which is usually the case, then the upper surface elongates for ΔL

$$\theta = L/R \;\Rightarrow\; L = \theta R \qquad \text{(the middle plane)} \tag{66}$$

$$L + \Delta L = \theta(R + \frac{1}{2}h_{PWB}) \qquad \text{(the surface)} \tag{67}$$

$$\Rightarrow \Delta L = \frac{1}{2}\theta h_{PWB} = \frac{1}{2}\frac{L}{R}h_{PWB} \tag{68}$$

$$\gamma = \frac{\Delta L}{h_{joint}} = \frac{1}{2}\frac{L}{R}\frac{h_{PWB}}{h_{joint}} \tag{69}$$

where θ is the bending angle and h_{PWB} is the thickness of the board. Thus, the relation between the shear deformation and the elongation of the edge interconnection in a 10-mm-long component on a 1-mm-thick board would be

$$\frac{\gamma}{\epsilon} = \frac{3}{2}\frac{h_{PWB}}{L} = 0.3. \tag{70}$$

In other words, the loading of interconnections on component perimeters in drop testing is more tensile than shearing. However, the differences between the maximum computed shear and tensile components of strain and stress are significantly smaller than the one calculated with (70); see Chapter 9.5.

5 Finite element method

Carrying out finite element analyses (FEA) is essential when the reliability of solder interconnections under shock loading conditions is studied, because the behaviour of component boards during a drop test is complex. FE analyses give information about the behaviour of component boards and the stresses in the interconnections, thereby helping to understand why different changes in tests lead to the observed changes in the failure modes and in the number of cycles to failure.

The finite element method (FEM) has been used successfully since 1960s to obtain numerical solutions in various problems. FE analyses can be divided into two parts: building up a model and computation. First, the structure to be analysed is discretised into a number of smaller parts, elements; secondly, the material behaviour (stress-strain relationship) of each element is defined. Then the boundary conditions and the loading conditions are given, after which stress distributions can be computed. FE programs compute the displacements of the nodes, which define the volumes of the elements, by minimising the total work (internal work + external work), and from the computed displacements the strains and stresses within the elements are obtained. A large number of books considering the finite element method are available (see [87Hug, 83Zie], for example).

When an FE model is constructed, the amount of information available is usually limited. Typically, the mechanical behaviour of materials is not well known. On the other hand, the geometry of structures is too full of details to be included in the model in its entirety. Therefore, an FE analysis is often a series of calculations, in which some modelling parameters are adjusted. The results from different simulations are compared with each other in order to find out how sensitive the analysis is to the adjusted parameters. The more sensitive the results, the more the analyser needs to consider what values to use. Measuring the behaviour of the structure and comparing the computed results to the measured ones helps making the model more accurate. For example, in the current work the behaviour of the screw joints between the test boards and the fixtures is not well known and could not be measured. However, their role is significant as the studies in the following chapters will show.

5.1 Finite elements

In the finite element method the analysed structure is discretised into smaller areas or volumes: (finite) elements. Elements are defined by the geometry and the interpolation functions. In two-dimensional cases the elements are usually triagonal or quadrilateral, in three-dimensional cases tetragonal or cube-like. Elements are usually linear or quadratic, which means that the boundaries of an element are defined by first- or second-order polynomials. For example, the geometry of a linear element (first-order polynomials as the interpolation functions) is defined by its corner nodes and the straight lines connecting the nodes. For quadratic or second-order elements there is an additional node between the corner nodes, and the interpolation polynomials, as well as the edges of the elements, are quadratic. In addition, the displacements within an element are usually interpolated using the same polynomials and the computed values of the displacements at each node. Since the total strains ϵ_{ij}^{tot} are derivatives of the displacements u_i in directions i and j,

$$\epsilon_{ij}^{tot} = \frac{1}{2}(\frac{\partial u_i}{\partial x_j} + \frac{\partial u_j}{\partial x_i}) \tag{71}$$

the interpolation also defines how total strains change within an element. In order to compute the stresses the total strain is divided into different types of strains according to the data provided by the user. The user decides what models of material behaviour are to be used and inputs values of the model parameters. The accuracy of an FE analysis depends heavily on the accuracy of the material models used.

There is a large number of different element types, and the choice depends on the problem to be solved. In this work shell, beam, continuum, and mass elements are used. Shell elements are formulated to give accurate results with a small number of elements for long, wide and thin structures, like circuit boards. Beam elements are good for long and narrow structures, like the standoffs. Continuum elements are suitable for all geometries, but the number of elements usually needs to be large. A mass element increases mass in a specific location only.

Shell elements are efficient when the in-plane dimensions of a plate are more than ten times its thickness. In such structures the displacements and rotations of the middle plane define the bending of the structure. In shell elements the strains parallel to the middle plane are usually assumed to depend linearly on the shell curvature

and the distance from the middle plane. The strains perpendicular to the plane are zero, unless they are used to control volumetric changes in the shell elements. Thus, the shell elements try to compute the response of a plate by considering only the deformation of the middle plane. Beam elements are similar to shell elements, but they take into account only the strains parallel to the beam axis. Thus, in shell elements one dimension is reduced and in beams two dimensions.

5.2 Submodelling

When stresses in solder interconnections are analysed, the reduction of the dimensions used in shell elements leads to problems in the vicinity of interconnections. The submodelling method is often used to solve such problems. In the method the bending of the whole assembly is first computed using a global model, which does not contain details usually, and the displacements are stored. Next, the stored displacements are used as the boundary conditions in a submodel of a specific detail (a component in this case), and the displacements determined with the submodel of a component are stored. Finally, the displacements from the component-level model are given as the boundary conditions to the interconnection-level model, which is used to compute the stress distributions in the interconnections (Fig. 12). With the help of the submodelling, a large amount of computing time can be saved, and the amount of computer memory required can be reduced. As a drawback, when submodelling is used, the details included only in submodels do not have any effect on the global behaviour. Therefore, the analyser has to carefully consider which details do not influence the global behaviour of the structure and which do.

5.3 Solving the equations of motion

Under dynamic loading the displacements of nodes are expressed by the equation of motion (45), which is rewritten here

$$\boldsymbol{K}\boldsymbol{u}(t) + \boldsymbol{C}\dot{\boldsymbol{u}}(t) + \boldsymbol{M}\ddot{\boldsymbol{u}}(t) = \boldsymbol{F}(t)$$

In dynamic problems the solution of (45) depends on the history of the loading. Therefore, in addition to solving $\boldsymbol{u}$ at the time t_n, which can be tedious if material nonlinearities exists, $\boldsymbol{u}$ must be computed for each time step before time t_n, and

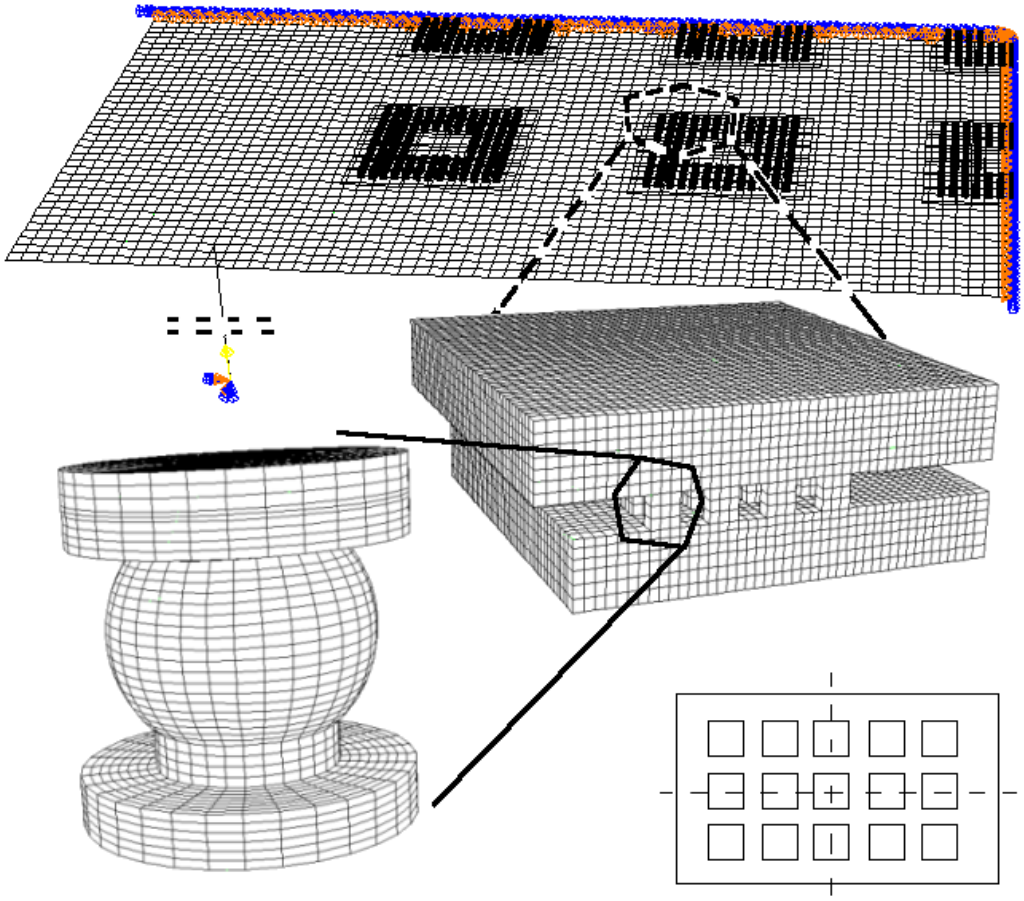

Figure 12 *Element meshes used in the finite element analysis employing the sub-modelling technique.*

the number of the steps may be large. Hence, analysing problems where dynamic forces are significant requires computing resources more than problems that can be solved by static analysis. In some cases, modal analysis can be employed to significantly reduce the amount of work, but that requires periodic loading, elastic material behaviour, and also an otherwise linear response. In the case of vibration tests modal analysis could be used to compute stresses, but that it is not an accurate method when drop tests are analysed. On the other hand, the analysis can be made using only a set of natural modes, as Syed *et al.* have done successfully [05Sye]. In this case the FE program is restricted to use only a predefined set of natural modes when computing the solution, which makes the analysis much faster.

There are two principal types of methods for solving $\boldsymbol{u}(t)$: explicit and implicit methods. In explicit methods the state at time t_{n+1} is computed by using only the known state at t_n (and possibly earlier states $t_0 \ldots t_n$), but in implicit methods the

state at t_{n+1} depends on the known state at t_n and the unknown state at t_{n+1}. The explicit method in Abaqus uses the explicit central difference rule [00Aba2, p. 6.2.1-2]. The displacements at time t_{n+1} are computed by first solving the acceleration at time t_n

$$\ddot{\boldsymbol{u}}(t_n) = \boldsymbol{M}^{-1}\left(\boldsymbol{F}(t_n) - \boldsymbol{K}\,\boldsymbol{u}(t_n) - \boldsymbol{C}\,\dot{\boldsymbol{u}}(t_n)\right) \tag{72}$$

and then the velocity in the middle of the step

$$\dot{\boldsymbol{u}}(t_{n+1/2}) = \dot{\boldsymbol{u}}(t_{n-1/2}) + \frac{\Delta t_n + \Delta t_{n+1}}{2}\ddot{\boldsymbol{u}}_n \tag{73}$$

where $t_{n+1/2}$ is the time at the middle of the step, and $\Delta t_{n+1} = t_{n+1} - t_n$ is the length of the step. Finally, the displacements at time t_{n+1} are computed

$$\boldsymbol{u}(t_{n+1}) = \boldsymbol{u}(t_n) + \Delta t_{n+1}\dot{\boldsymbol{u}}(t_{n+1/2}) \tag{74}$$

In the algorithm the acceleration is assumed to be piecewise constant. Explicit methods are conditionally stable, and, for accurate results time steps must be short when compared to steps during implicit calculations. Hence, there are more time steps in explicit calculations. However, each step in explicit methods is computationally less laborious. In explicit methods time steps are usually limited to the smallest period of time that it takes for a shock wave to travel through an element in a model [99Ted, page 570]

$$\Delta t_{crit} = \min \frac{L_e}{\sqrt{(\lambda + 2G)/\rho}} \tag{75}$$

where L_e is the length of the element e, $\lambda = \nu E/[(1+\nu)(1-2\nu)]$ is the Lamé constant, ν is the Poisson ration, G is the shear modulus and ρ is the density. Thus, the time step is very short. To make the computation faster, a lumped mass matrix is employed (non-zero terms only on the diagonal); thus, inverting the mass matrix in (72) is trivial, which makes the computation of one step very fast.

In implicit methods the equation of motion (45) is solved at time t_{n+1} or at some other point $t_{n+\alpha}$ ($\alpha > 0$) by using the previously computed results at time t_n and the estimated values at t_{n+1}. If the equality in (45) is not obtained with the estimated values, new estimations are calculated and tried with (45). In practise, the left-hand side of (45) is never equal to the right-hand side, and some accuracy criteria must be used to end the iteration.

In Abaqus the implicit computation is carried out by employing the Hilber-Hughes-Taylor method, where the displacements and velocities are computed by

$$\boldsymbol{u}(t_{n+1}) = \boldsymbol{u}(t_n) + \Delta t \dot{\boldsymbol{u}}(t_n) + \Delta t^2 \left[\left(\frac{1}{2} - \beta_1 \right) \ddot{\boldsymbol{u}}(t_n) + \beta_1 \ddot{\boldsymbol{u}}(t_{n+1}) \right] \tag{76}$$

$$\dot{\boldsymbol{u}}(t_{n+1}) = \dot{\boldsymbol{u}}(t_n) + \Delta t[(1-\beta_2)\ddot{\boldsymbol{u}}(t_n) + \beta_2 \ddot{\boldsymbol{u}}(t_{n+1})] \tag{77}$$

where β_1 and β_2 are parameters that affect the numerical behaviour of the method. The equation of motion (45) is modified slightly in order to improve the numerical behaviour of the method:

$$\begin{aligned} \boldsymbol{M}\ddot{\boldsymbol{u}}(t_{n+1}) + (1+\beta_3)\boldsymbol{C}\dot{\boldsymbol{u}}(t_{n+1}) - \beta_3 \boldsymbol{C}\dot{\boldsymbol{u}}(t_n) + (1+\beta_3)\boldsymbol{K}\boldsymbol{u}(t_{n+1}) \\ -\beta_3 \boldsymbol{K}\boldsymbol{u}(t_n) = (1+\beta_3)\boldsymbol{F}(t_{n+1}) - \beta_3 \boldsymbol{F}(t_n) \end{aligned} \tag{78}$$

where $-\frac{1}{3} \leq \beta_3 \leq 0$. Parameters β_1 and β_2 in (76) and (77) depend on β_3: $\beta_1 = \frac{1}{4}(1-\beta_3)^2$, and $\beta_2 = \frac{1}{2} - \beta_3$. In Abaqus the lengths of time increments in implicit analysis can be automatically controlled. For that purpose Abaqus uses a half-step residual control. The half-step residual is the equilibrium residual error (out-of-balance forces) halfway through a time increment. If the error is small, it indicates that the time step can be increased safely, and *vice versa*. The user sets the value of the acceptable half-step residual tolerance (`haftol`), if the automatic time incrementation is used.

With implicit methods time steps can be longer, the equation system becomes more complex, and a few iterations in each step are required for good accuracy. Explicit methods are found to be more efficient when the problem is strongly non-linear, includes contacting surfaces, and the time period is short. In the case of drop testing, when the loading is defined by the measured acceleration, implicit methods are more efficient. However, if the impact that is generated when the drop table hits the strike surface is to be calculated, explicit methods may give results faster.

6 Plastic properties of the SnAgCu solders

The stress-strain curves of three SnAgCu alloys under a large range of strain rates ($10^{-5} - 10^{2}$ %/s) were measured at room temperature by carrying out shear tests using grooved lap joint (GLJ) specimens [98Rei]; see Fig. 13. The effect of temperature on strain rate was determined by carrying out additional tests at 70 °C and 110 °C. From the measured data the parameters of the plastic deformation models (13) and (14) (page 16) were determined. Three SnAgCu solders (Sn2.0Ag0.5Cu, Sn3.4Ag0.8Cu, and Sn4.0Ag0.5Cu) where chosen for the measurements.

6.1 Measurement system

The measurement apparatus used in this work was the MTS 858 Table Top System, which is a servohydraulic machine for loading specimens in one direction (tension/compression). An MTS 661.18 force sensor (-1 kN - +1 kN) and an MTS 632.31 extensometer (-10 % - +20 % strain, gauge length 20 mm) were used in the measurements. Either the extensometer or the force sensor was used to control the test. In order to obtain a steady state in reasonable time, the loading force was held constant when the behaviour of the solders under strain rates of less than 10^{-3} %/s was to be measured. At higher strain rates the strain rate was controlled and the evolution of the force was recorded. The hydraulic system had problems in keeping the strain rate constant when high strain rates ($>$ 30 %/s) were wanted. During the rapid tests the rate was first too low and then increased over the set value, and before the constant rate was reached, the solder joints broke. In these cases an average value of the strain rate was calculated from the data that included the points from the end of the test to the moment when the stress increased to values approximately 70 % of the maximum value. The maximum strain rate was typically about 40 % higher than the average value. The maximum stress was used as the steady state stress value.

The stress-strain measurements at elevated temperatures were carried out in an environmental chamber (MTS CE42). At 110 °C the temperature varied approximately ± 5 °C in cycles of about one hour, and this had a clear effect on the measured strains. The extensometer was attached to the steel rods of the GLJ spec-

imens (Fig. 13), and when the rods expanded the measured strain value changed. The error that the ± 5 °C change in temperature caused in the measured value of strain was approximately

$$\Delta\epsilon = \pm\Delta L_{steel}/h_{joint} = \pm\Delta T\alpha_{T,steel}L_{ext}/h_{joint} = \pm 0.004 \tag{79}$$

where the coefficient of thermal expansion of steel $\alpha_{T,steel} = 11.5 \cdot 10^{-6}$ 1/°C, $\Delta T =$ 5°C, $L_{ext} = 20$ mm is the gauge length of the extensometer, and $h_{joint} = 0.3$ mm. When the deformation rate was slow, the temperature variation resulted in sinuous variation in the stress-strain curve, the magnitude of which was about 5 % of the maximum stress. During the tests the measured strain rate was constant, but the plastic strain rate changed with the rate of the thermal expansion rate

$$\dot{\epsilon}^{pl} = \dot{\epsilon}_{measured} - \dot{\epsilon}_T,\ \dot{\epsilon}_T \in \left[-\frac{0.4\%}{0.5\,\mathrm{h}}, +\frac{0.4\%}{0.5\,\mathrm{h}}\right] \tag{80}$$

The magnitude of the force depends on the rate of plastic strain rate, and thus, the measured force values reduced as the temperature in the oven increased and vice versa. When the parameters of the models were determined, the measured value of the total strain rate was used as the value of the plastic strain rate and the value of the stress was obtained by filtering out the sinuous variation in the stress.

6.2 Grooved lap joint specimen

The geometry of the grooved lap joint (GLJ) specimens [98Rei] is derived from Iosipescu's proposal [67Ios]. The GLJ specimen was designed to produce a nearly uniform distribution of shear stresses in the solder joint with minimal bending stresses and to be easy to manufacture. In addition to the uniform stress state, the solder microstructure in the GLJ specimens is close to that in actual solder interconnections [05Rei]. The grain size in interconnections is close to the interconnection size, and this has a significant effect on solder behaviour. Elastic and plastic properties depend on the lattice orientation, and grain boundaries affect both plastic deformation and crack propagation, as explained earlier in Chapter 3. Therefore, it is important that the microstructure of the solder in the test specimens is similar to that in actual interconnections.

Different types of specimen have been developed in order to obtain a microstructure that is similar to that in solder interconnections. Single lap joint specimens are

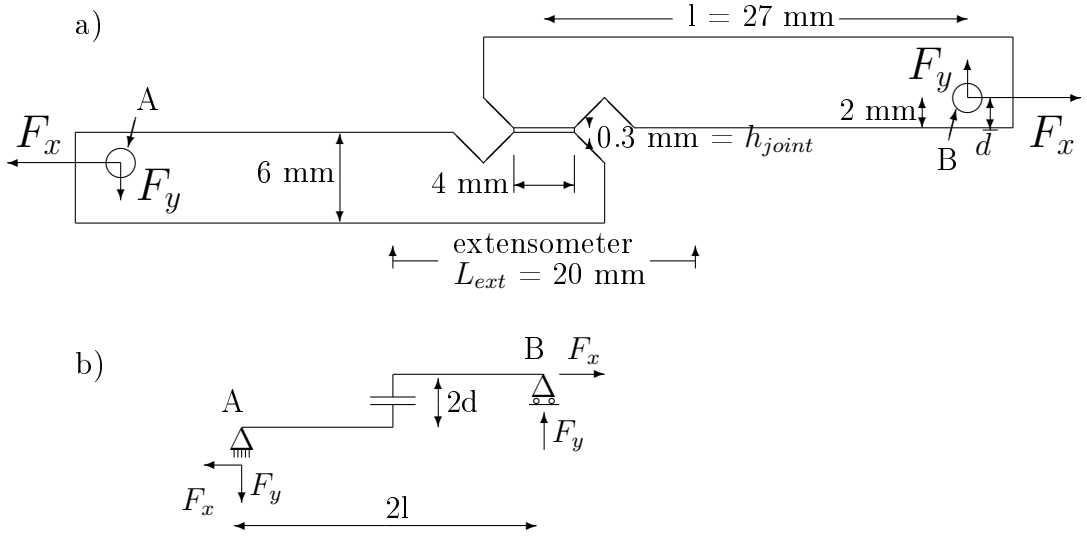

Figure 13 *a) Dimensions of the grooved lap joint specimens used in this work, and the forces applied. b) Free-body diagram.*

similar to grooved lap joint specimens but without the groove. Double lap joints have two solder joints and the geometry is symmetric across the longitudinal axis. In both single and double lap joints strains are strongly concentrated at the corners of the joints, which is not good for obtaining accurate results. Researchers have also used a BGA type of specimen, in which two rigid plates are soldered together using an array of solder interconnections, [92Dar]. In this type of specimen the same microstructure as in real interconnections can be obtained, but the distributions of strains and stresses are even less uniform than in single lap joints. When the microstructure, the stress distribution, and the ease of specimen preparation are being considered, the grooved lap joint specimens are a very good option.

There is a small asymmetry in GLJ specimens that causes additional tensile stress in the joint; see Fig. 13. As a result of the vertical distance $2d$ between the applied force F_x (point B) and the fixed end of the specimen (point A) a vertical force F_y is generated. The frictional forces between the holes and the pins are insignificant; thus, the moment around the hole A is zero and the relation between the vertical and horizontal forces is

$$F_x 2d = F_y 2l \tag{81a}$$

$$\Rightarrow F_y = F_x d/l \tag{81b}$$

In addition, the moment at the centre of the joint is zero:

$$M_{joint} + F_y l - F_x d = 0 \;\Rightarrow\; M_{joint} = 0 \tag{82}$$

The average shear and tensile stresses acting in the joint are

$$\tau_{xy} = \frac{F_x}{A},\; \sigma_y = \frac{F_y}{A} = \tau_{xy}\frac{d}{l} = 0.080\tau_{xy} \tag{83}$$

where $d = 2.15$ mm and $l = 27$ mm. Thus, the effect of the average vertical tensile stress on the von Mises stress σ_{vm} is very small

$$\frac{\sqrt{\sigma_y^2 + 3\tau_{xy}^2}}{\sqrt{3\tau_{xy}^2}} = \frac{\sqrt{3.006}}{\sqrt{3}} = 1.001 \tag{84}$$

and is not taken into account in the determination of the values of the material parameters.

6.3 Preparation of GLJ specimens

The GLJ specimens used in this work were made of hardened steel in order to reduce plastic deformation in the groove tip. With copper specimens the stress concentration at the tip caused extensive plastic deformation under high loads, which reduces strain measurement accuracy. The steel pins were electrolytically coated with nickel (a layer about 2 μm thick), on top of which an electrolytic copper coating (about 3 μm thick) was applied.

The desired amounts of tin, silver, and copper were measured on a high sensitivity scale, after which the components were put in a jar into an oven at 300 °C, which is well above the liquidus points of the alloys. After the solders had melted, the jars were shaken to ensure the homogeneous distribution of silver and copper. The jars were taken out of the oven to cool down in air. The solidified solder plates, which were 5 mm thick, were cold rolled to sheets 0.3 mm thick. The sheets were cut into 4 mm × 4 mm squares and dipped into HCl acid in order to clean their surfaces. The solder squares were put between two GLJ pins in an aluminium jig. The jig was lowered into a jar filled with glycerol (240 °C). After the solder between the pins had melted, the jig was kept in the glycerol for 30 seconds, after which the jig was lifted onto a steel table for cooling. The solder joints cooled down to 50 °C in 30 seconds. After the solidification the thickness of each solder joint was measured at opposite sides, and the average value was used when strain rates were calculated.

6.4 Processing the measured data

After the strain and force measurements the cross-sectional area of each grooved lap joint specimen was measured. The GLJ pins were detached from each other, the cross-sections of the solder joints were photographed, and from the pictures the cross-sectional area was calculated. In this way, the amount of voids, as well as other geometrical defects, could be taken into account. In most samples the amount of voids was less than 5 %.

FE programs usually compute plastic strains using the von Mises yield criteria; therefore, the plastic properties need to be described by using the von Mises stress and strain. Hence, the measured data (the force F_x and the extensometer value $\epsilon_{measured}$) are first converted to shear stress τ_{xy} and shear strain γ_{xy} values using formulas

$$\tau_{xy} = F_x/A \tag{85a}$$

$$\gamma_{xy} = \epsilon_{measured} L_{ext}/h_{joint} \tag{85b}$$

where A is the joint area and L_{ext} and h_{joint} are shown in Fig. 13. From (85) the von Mises stresses and strains are calculated:

$$\sigma_{vm} = \sqrt{3}\,\tau_{xy} \tag{86a}$$

$$\epsilon_{vm} = \sqrt{1/3}\,\gamma_{xy} \tag{86b}$$

Then the amount of plastic deformation is calculated by subtracting the elastic strain from the total strain

$$\epsilon_{vm}^{pl} = \epsilon_{vm} - \frac{\sigma_{vm}}{E} \tag{87}$$

where E is the elastic modulus at the test temperature. In practice, the amount of elastic strain is very small ($\sigma_{vm}/E < 0.2$ %) and has a small effect on the stress-strain graph only when the load is increasing.

In addition to the above-mentioned good properties of GLJ specimens, there is one more benefit: when dog bone type tensile test specimens are used one should take into account two changes in the specimen geometry that occur during loading: *i*) the reduction of the cross-sectional area that is caused by plastic deformation and *ii*) the increasing length of the specimen. Under pure shear loading, as in the case of

a GLJ specimen, the area and height of the specimen do not change, and additional data modification is not needed.

6.5 Determining the parameters of the plastic deformation models

The parameters for the Anand's model (14), which is rewritten here

$$\begin{aligned} \dot{\epsilon}_{ef}^{pl} &= C_5 \sinh^n(C_6\sigma_{ef}) \exp(-Q/kT) \\ C_6 &= \xi/s \\ \dot{s} &= \left[h_0 \left|\left(1 - \tfrac{s}{s^*}\right)\right|^a \operatorname{sign}\left(1 - \tfrac{s}{s^*}\right)\right] \dot{\epsilon}_{ef}^{pl} \\ s^* &= \hat{s} \left[\frac{\dot{\epsilon}_{ef}^{pl}}{C_5} \exp\left(\tfrac{Q}{kT}\right)\right]^{\zeta} \end{aligned}$$

were obtained by following the instructions in [87Ana]. First, a linear least squares fit was carried out to obtain the values of a, ch_0, $c = \bar{\sigma}^*/s^*$ and $\tilde{\sigma}_0$ by inputing measured stress and strain values to equation (88), which describes strain-hardening under a specific strain rate.

$$\sigma_{vm} = \bar{\sigma}^* - \left[(\bar{\sigma}^* - \bar{\sigma}_0)^{(1-a)} + (a-1)ch_0(\bar{\sigma}^*)^{-a}\epsilon_{vm}^{pl}\right]^{1/(1-a)} \tag{88}$$

where σ_{vm} and ϵ_{vm}^{pl} are the measured stress-strain pairs and $\bar{\sigma}^*$ is the saturated (maximum) stress of the same curve. The initial value of the deformation resistance $s_0 = \bar{\sigma}_0/c$. When values for the parameters C_5, Q, n, ζ, and $(\xi/\hat{s})$ as well as those for the parameters of the model (13) were determined, the sum of the squares of the relative error e_r in the predicted saturated stress was minimised:

$$e_r = \sum_i \left(\frac{\bar{\sigma}_{model,i}^* - \bar{\sigma}_{measured,i}^*}{\bar{\sigma}_{model,i}}\right)^2 \tag{89}$$

where i refers to the test sample and $\sigma_{model,i}^*$ is the calculated steady state stress value for the measured strain rate.

There are nine parameters in the Anand's model ($C_5, n, Q, \xi, h_0, a, \hat{s}, \zeta$, and the initial value of the deformation resistance s), but only four variables are measured: stress, strain, temperature, and time. Hence, the material parameters are dependent on each other, which makes obtaining the "right" values difficult. Therefore, when comparing the determined values with values from other studies, one should compute stress-strain graphs and compare those, instead of comparing single parameters.

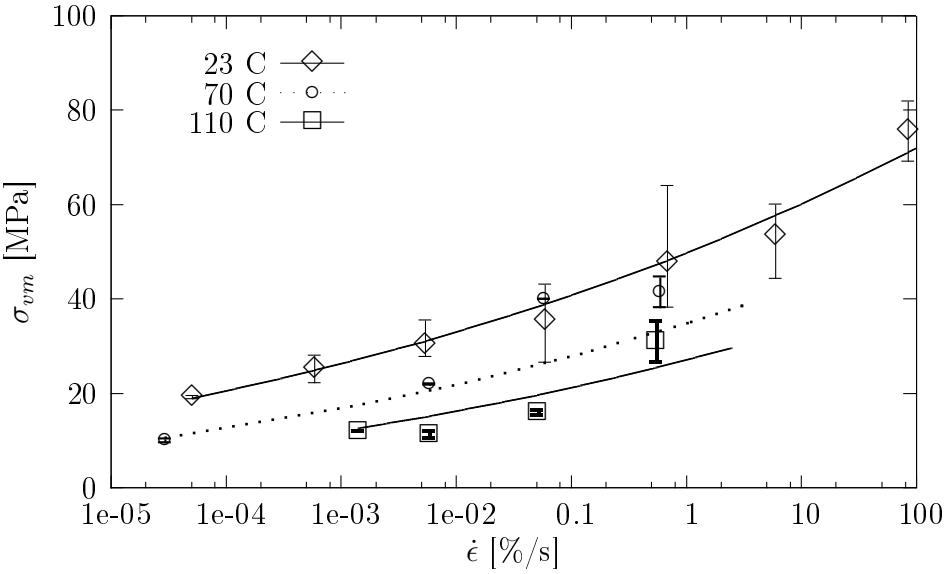

Figure 14 *Maximum von Mises stresses σ_{vm} as functions of the effective strain rate for Sn2Ag0.5Cu solder at 23, 70, and 110 °C.*

6.6 Sn2.0Ag0.5Cu specimens

A total amount of 49 Sn2.0Ag0.5Cu specimens were tested: 33 of them at room temperature, 7 at 70 °C, and 9 at 110 °C. The average values of saturated von Mises stresses at different effective strain rates (see (86)) are shown in Fig. 14 together with error bars showing the maximum and minimum values and the model (14) prediction. Each data point is given in Table A-I in Appendix A. The parameters determined for the model (14) are presented in Table I. The values change rather much from one alloy to another even though the changes in the compositions are small (especially between Sn3.4Ag0.8Cu and Sn4Ag0.5Cu), which we believe is not realistic. The values are not independent on each other, and errors in one value affect the values of the other parameters. However, these values were obtained with the described process.

The model prediction fits well with the average values at room temperature and

Table I *Parameters of Anand's model (14) determined from the measurements in this work.*

	C_5	n	ξ	Q/k	h_0	a	$\hat{s}$	ζ
Sn2Ag0.5Cu	500	6.3	4.3	8500	6100	1.3	28.7	0.04
Sn3.4Ag0.8Cu	500	3.3	7.1	9000	5900	1.4	39.4	0.03
Sn4Ag0.5Cu	600	8.3	3.3	9000	9300	1.2	36.7	0.03

at 110 °C but not at 70 °C. At elevated temperatures the number of test samples were smaller than at room temperature. Hence, the rather poor fit is propably due to random scatter in the measurements and specimens. At room temperature a straight line would also fit almost as well as the Anand's model. Thus, there seems to be only one mechanism controlling the deformation at room temperature. However, the highest value is clearly off a line connecting the points of lower strain rates, which indicates that a change in the mechanism is possible, but insufficient data is available for making conclusions.

The strain-rate-hardening of the solder is significant. At room temperature the maximum stress increases from 20 MPa at the rate of $5 \cdot 10^{-5}$ %/s to 75 at 100 %/s. At higher temperatures the relative increase seems to be even larger.

6.7 Sn3.4Ag0.8Cu specimens

Fig. 15 shows the measured values and the model prediction for the Sn3.4Ag0.8Cu alloy. The highest strain rate for this alloy is an order of magnitude smaller than that for Sn2.0Ag0.5Cu solder. The model prediction fits well with the measurements and only one mechanism seems to be controlling the deformation, as in the case of Sn2.0Ag0.5Cu. A total amount of 49 specimens were tested: 31 at room temperature, 12 at 70 °C, and 6 at 110 °C (Table A-I). The determined parameters of the model (14) are presented in Table I, and those of the model (13) are presented in Table II.

If the model prediction is extended to strain rate of 1 000 %/s (1 % strain in 1 ms), which is close to the strain rates in the drop tests, the strength of the solder increases to values over 100 MPa.

Table II *Determined parameters of the plastic deformation model (13) for Sn3.4Ag0.8Cu.*

	C_1	m	C_2	Q/k
Sn3.4Ag0.8Cu	650	2	0.12	7500

6.8 Sn4.0Ag0.5Cu specimens

Fig. 16 presents the measured values and the model prediction for Sn4.0Ag0.5Cu solder. Significant strain-rate-hardening is evident as in the case of the other com-

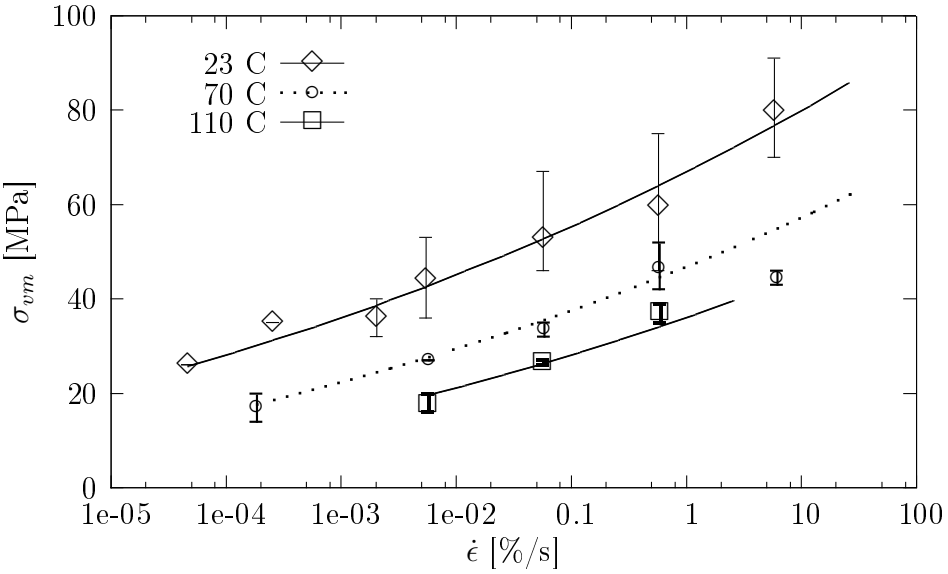

Figure 15 *Maximum von Mises stresses as functions of the effective strain rate for Sn3.4Ag0.8Cu solder at 23, 70, and 110 °C.*

positions, and an increase in temperature reduces the strength of the solder. A total amount of 43 specimens were tested: 23 at room temperature, 14 at 70 °C, and 6 at 110 °C (Table A-I). The determined parameters are presented in Table I.

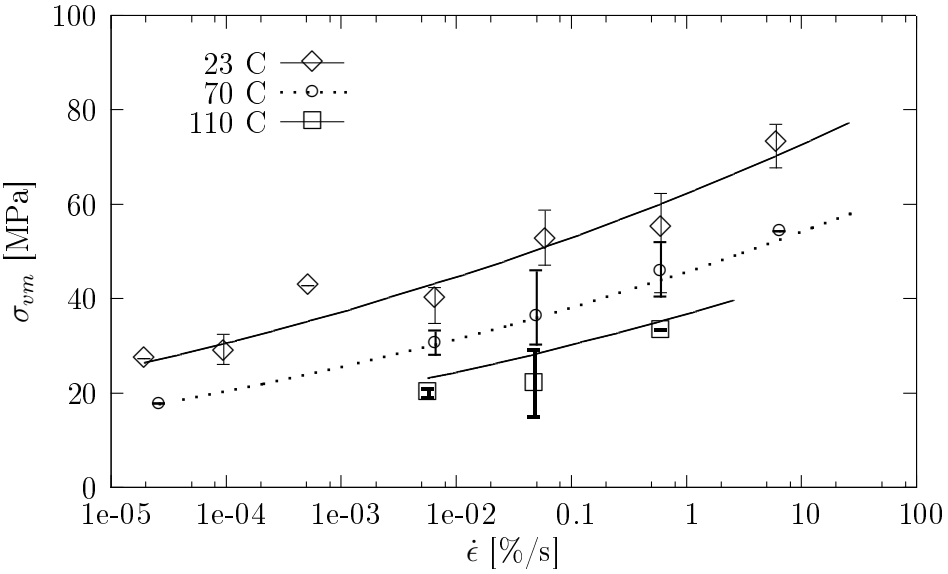

Figure 16 *Maximum von Mises stresses as functions of the effective strain rate for Sn4Ag0.5Cu solder at 23, 70, and 110 °C.*

6.9 Comparison of the alloys

The alloys Sn3.4Ag0.8Cu and Sn4.0Ag0.5Cu are equally strong and stronger than the Sn2.0Ag0.5Cu because of the strengthening effect of silver; see Fig. 17. From the model predictions it can be estimated that if Sn2.0Ag0.5Cu is deformed at a rate that is more than 10 times that of the other solders, the steady state stresses become equal. At slow strain rates even larger increase in the strain rate is required for the same stress. Increasing the temperature from room temperature ($\sim$ 298 K) to 110 °C (383 K) decreased the maximum von Mises stress of each alloy by approximately one half.

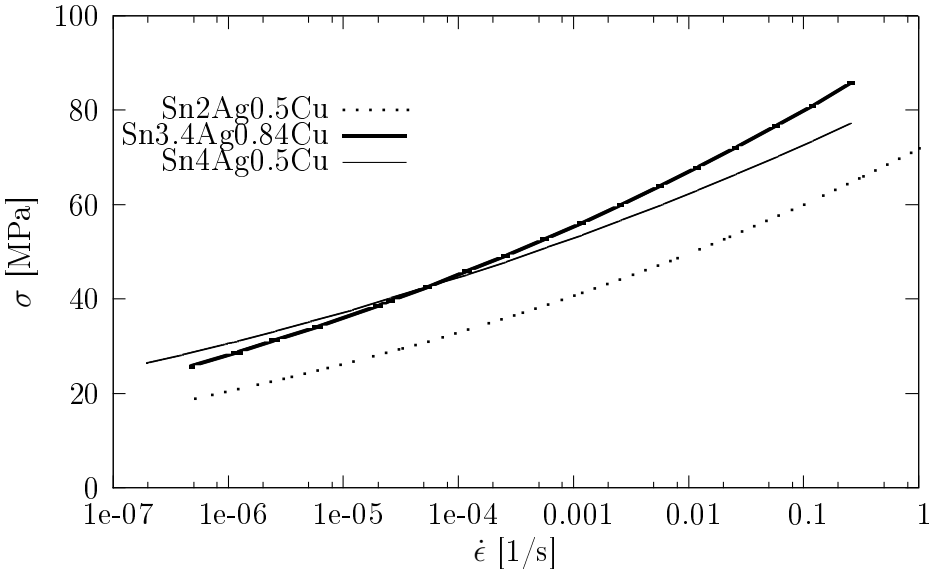

Figure 17 *Comparison of the three alloys at room temperature.*

6.10 Strain-hardening

The typical evolution of the measured flow stress is presented in Fig. 18. The solder strain-hardened to a saturated value, and the Anand's model (14) predicts the behaviour well. However, occasionally the evolution of the solder's strength was clearly different; see Fig. 19. The reason for the difference was not studied, but it is expected to result from the small number of grains in the joint.

When interconnections are loaded for several hundred of cycles, which is common in thermal cycling tests, solder is expected to harden during the first cycles, and the strain-hardening phase is often ignored. But, if the loading lasts for several cycles

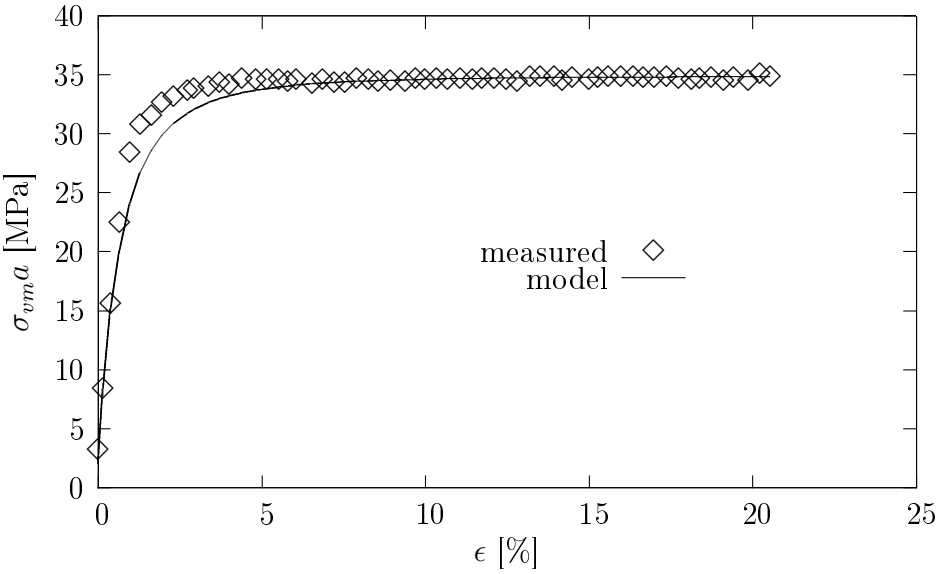

Figure 18 *Typical evolution of the von Mises stress as a function of plastic strain (Sn3.4Ag0.8Cu, 70 °C, $\dot{\epsilon} = 5.7 \cdot 10^{-2}$%/s) and the prediction by Anand's model (14).*

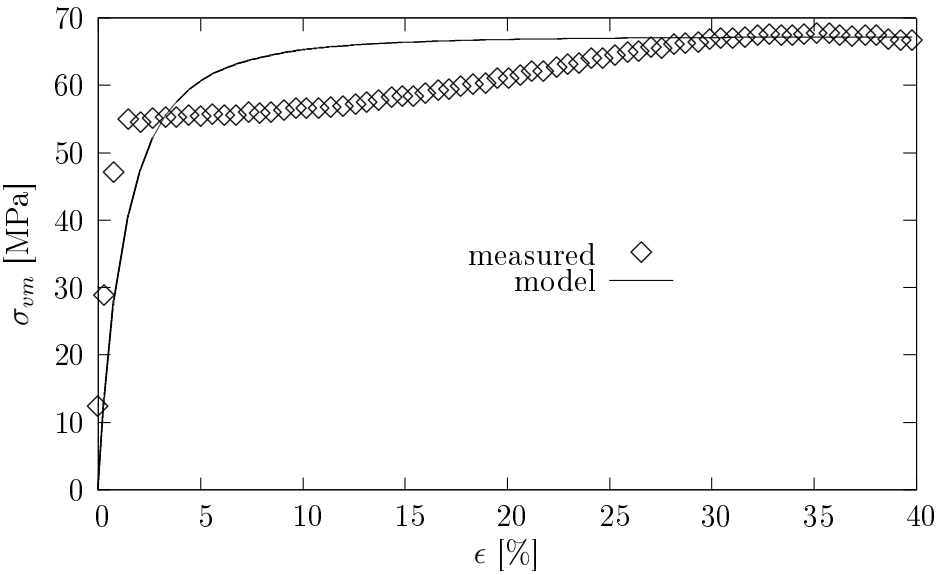

Figure 19 *Less typical stress-strain relation (Sn3.4Ag0.8Cu, 23 °C, $\dot{\epsilon} = 5.8 \cdot 10^{-2}$ %/s) and the computed evolution.*

only, as is rather common in drop tests, the strain-hardening has a significant effect on the generated stresses. On the basis of the computations presented in Chapter 9.5, the magnitude of plastic strains in solder interconnections does not exceed the value of 1 %, except in a very narrow area close to the corners, where the strain is as high as 1.5 %. With the determined parameters Anand's model (14) predicts that

when the solder is elongated by 2 %, the yield stress reaches 60 % of its maximum value, and the plastic strain of over 5 % is required to strain-harden the solder to 90 % of its maximum strength. In cyclic deformation metals often harden slowly from cycle to cycle up to some value but not as quickly as in monotonous loading. Therefore, when the "reliable enough" limit is set to 30 drops, as in the drop test standard, it may be so that the solder does not reach its full strength during the test. Therefore, in the stress analysis of drop tests strain-hardening should be taken into account to avoid the overestimation of the stresses in interconnections.

6.11 Comparison with other studies

The parameters of the Anand's model (14) were compared to those reported earlier by Amagai *et al.* [02Ama] and Cheng *et al.* [00Che] (Cheng *et al.* used the measurements from [92Dar]). The comparison was done by calculating the steady state stress values at different strain rates using the parameters from the different sources. The calculated values are plotted in Fig. 20. The solders that were used in the comparison were: Sn3.4Ag0.8Cu in this work, Sn3.5Ag0.75Cu in [02Ama], and Sn3.5Ag in [00Che]. In both papers [02Ama] and [92Dar], tests were carried out using solder joints. Amagai *et al.* used dog-bone samples made of copper; they cut the samples in two pieces from the centre and then electroplated and soldered them back together. Thus, the stress state was tensile. Darveaux and Banerji used a setup in which two ceramic substrates were soldered together using an area array of solder interconnection, and later the backs of the ceramic substrates were glued to steel rods for applying the loading. They used solder-mask-defined ball-shaped interconnections that were 0.4 to 0.45 mm high, and annealed the samples for 100 h at 100 °C or several months at room temperature. The samples were loaded both in shear and in tension.

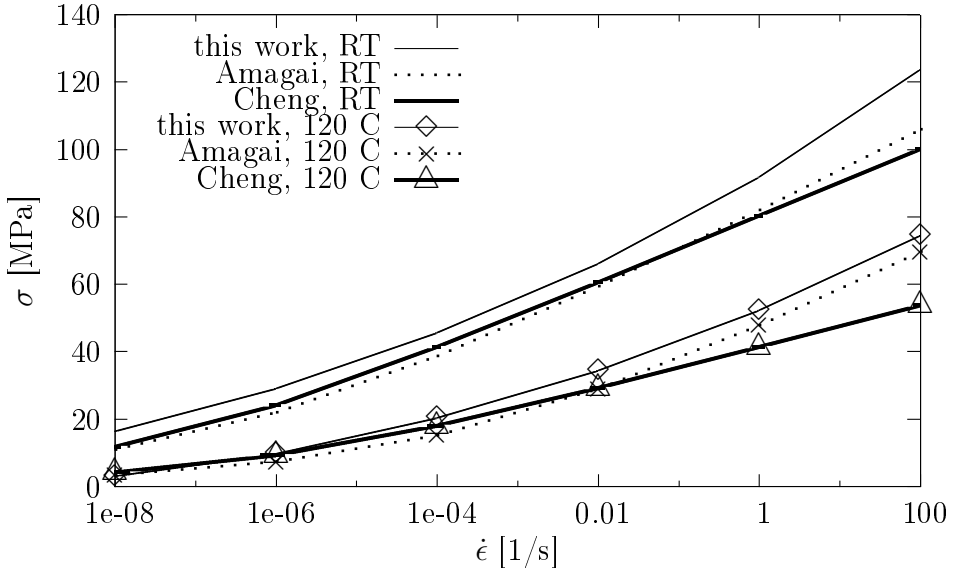

Figure 20 *Calculated maximum von Mises stress as a function of strain rate at room temperature (RT) and at 120 °C according to this work and articles [02Ama, 00Che].*

7 Bending of the component boards during the tests

The bending of component boards in the vibration test should be similar to that in the drop test in order to produce similar stresses in interconnections. The strains on the component boards during the vibration and drop tests were measured in order to compare the bending of the boards during the tests, and to evaluate how strong excitation is required in the vibration test to produce a similar bending as the drop test does. In addition, the measurements were used to verify and improve the FE analysis. The natural modes of the test boards were measured in order to help understanding the behaviour of the test boards during the tests. When the natural modes are measured, the strains and displacements are very small and rapid, thus plastic deformation and other nonlinearities should not affect the measurements. Therefore, the natural mode analysis was also used when the parameters of the FE analysis were adjusted.

7.1 Drop and vibration test assemblies

The test assemblies consisted of a 1+6+1 multilayer board and up to 15 surface-mounted BGA components. The test assembly was made according to the JESD22-B111 standard. The layout of the board is presented in Fig. 21, and the layers of the board and their copper coverages are presented in Table III. During the tests the test board is attached either to the drop table or to the vibration test apparatus with four screws through the holes in the corners of the board. There are fifteen component locations in the test board, C1 - C15. On the basis of the geometrical symmetry of the board, it is assumed that the loading of the components is also symmetric. Thus, the loading is assumed to be identical within the following groups: *i*) C1, C5, C11, and C15, *ii*) C2, C4, C12, and C14, *iii*) C3 and C13, *iv*) C6 and C10, *v*) C7 and C9. This grouping is used when the times-to-failure and the computed stresses are studied.

There are three minor differences between the JESD22-B111 board and the test board of this study: *i*) the locations of the components, *ii*) the copper coverage of the layers, and *iii*) the daisy chain connections on the micro-via side of the board. The first two of them have a small effect on the mechanical behaviour of the board.

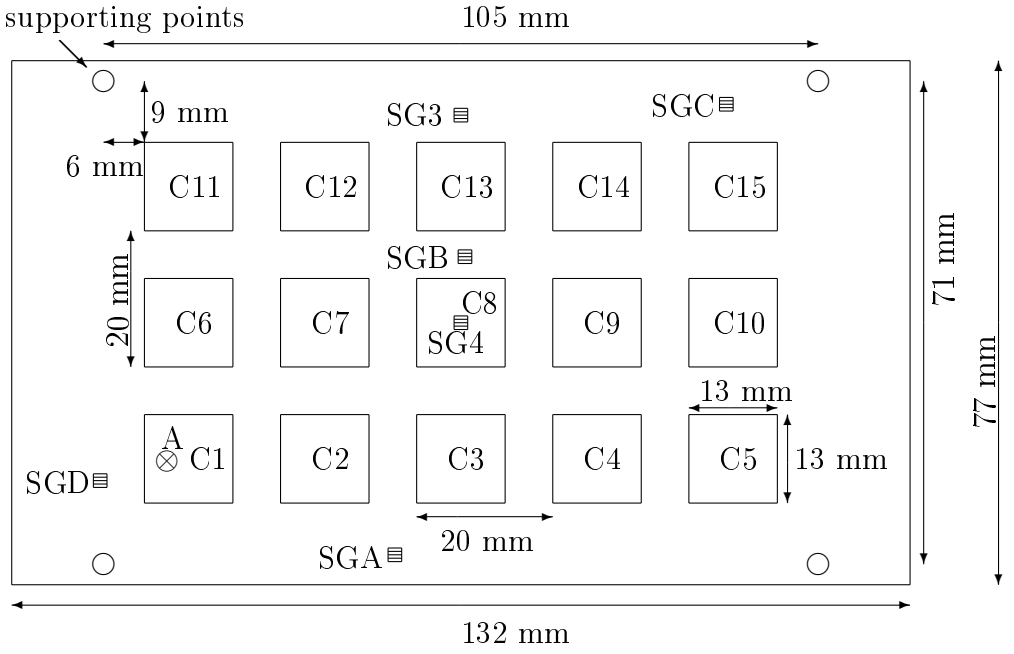

Figure 21 *Board layout: the dimensions and the locations of the components (C1-15), the strain gauges (SGA-D,3,4), and the accelerometer (A).*

The component locations C1 to C5 and C11 to C15 were 4 mm too far from the long board edges, and the column 1 (locations C1, C6, and C11) and the column 5 (locations C5, C10, and C15) were 1.5 mm too far from the short board edges. The difference in the corner component locations can have a significant effect on the lifetime of the components at locations C1, C5, C11, and C15, but the effect is insignificant on the lifetimes of the components in the middle column. The amount of copper has a small effect on the stiffness and mass of the board. The third difference may affect the time when a failure is detected only. The daisy-chain connections between the interconnections on the microvia-side of the board should be on layer 2, but they are on layer 1. Thus, failures in the microvias were not detected electrically. However, in the drop tests and the vibration tests the same board was used, and hence, the differences do not affect the comparison of the tests.

The measurements were carried out with component boards having 0, 1 or 15 components mounted on them (identified as 0BGA, 1BGA, and 15BGA). Nine of the 1BGAs were annealed at 120 °C for 500 h before testing for evaluating the effect of the Kirkendall voids. The components were either ball grid arrays (BGA) or

Table III *Measured layer thicknesses of the PWB. Numbers in parentheses refer to the layer number. LPI - solder mask material, RCC - resin coated copper, FR4 - flame retardant no. 4*

PWB outside components		component areas	
layer	thickness [μm]	layer	thickness [μm]
LPI	18	LPI	39
(1) Cu-40%	45		
RCC	57	RCC	76
(2) Cu-70%	19		
FR4	145	FR4	145
(3) Cu-70%	19	RCC	19
FR4	145	FR4	145
(4) Cu-70%	19	RCC	19
FR4	145	FR4	145
(5) Cu-70%	19	RCC	19
FR4	145	FR4	145
(6) Cu-70%	19	RCC	19
FR4	145	FR4	145
(7) Cu-70%	19		
RCC	57	RCC	76
(8) Cu-40%	45	LPI	39
LPI	18		
total thickness	1.1 mm		

leadless leadframe packages (LLP). The components were daisy chain components, which means that all the interconnections of one component are connected in series. Thus, if any of the interconnections fails, an open is detected. The BGAs (Figs. 22 and 24) were 12 mm × 12 mm × 0.9 mm and had 144 bumps (Sn0.2Ag0.5Cu) in a 13 × 13 array with a 5 × 5 clearance in the centre. The silicon chip inside the BGA was 7.5 mm × 7.5 mm × 0.27 mm in size. Between the chip and the bumps, there was an interposer 0.11 mm thick. The weight of the BGAs was 0.32 g, and the height without the bumps was 0.9 mm. No additional metallisation was used under the bumps on the component side; thus, the solder was in direct contact with the copper pads of the interposer. Cross-sections of the BGA components and the interconnections are presented in Figs. 22 and 23. Two types of LLPs were used: LLP48 and LLP8 (Fig. 24). LLP48s were 7 mm × 7 mm in size and had 12 interconnections along each edge. The silicon chip in LLP48 was 5 mm × 5 mm × 0.1 mm in size, and there was a copper die attachment pad (DAP) beneath the

chip. The DAP was equal to the chip in size. LLP8s were 2.5 mm × 2.5 mm in size and had 4 interconnections along edges parallel to the short edges of the board. The DAP of LLP8 was 1.5 mm × 1 mm in size. In addition to the interconnections on the edges, the die attachment pad was also attached to board by soldering. LLPs were used only when the effect of the location of the component on the number of cycles to failure was being investigated in the case of the vibration test (Chapter 8).

7.2 Natural frequency analysis

The natural frequencies and modes of the 15BGA boards were measured at the VTT Technical Research Centre of Finland in the Laboratory of Automation. In addition, the effects of the components on the natural frequencies were measured at Helsinki University of Technology in the Laboratory for Mechanics of Materials by employing two boards with different amounts of components: a board with 15 components and one without components.

7.2.1 Measurement system

During the measurements at VTT, the board was attached to an aluminium fixture, which was similar to that in the drop test vehicle, using four screws. The board was given a short and light impact, and the generated vibration was measured and analysed. The estimates of the natural modes were obtained by repeating the measurement at ten different locations; see the white rings in Fig. 26, page 60. The vibration was measured optically with a vibrometer (Polytec OVD-01, OFV-302/3000), and an instrumental hammer (Brüel & Kjær, Type 8203) was used to generate a short and light impact. The measurements were analysed using Fast

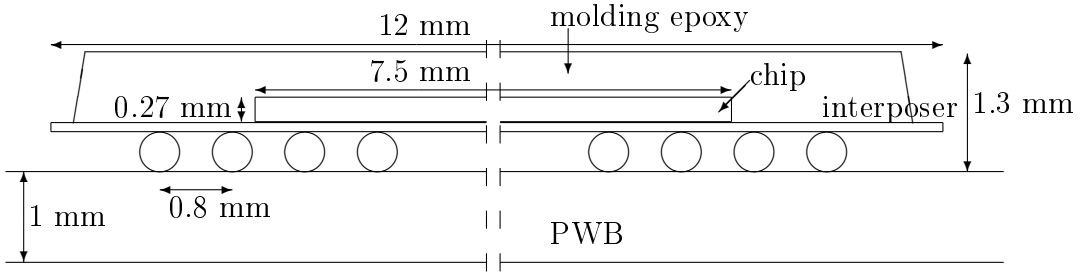

Figure 22 *Cross-section of the BGA component.*

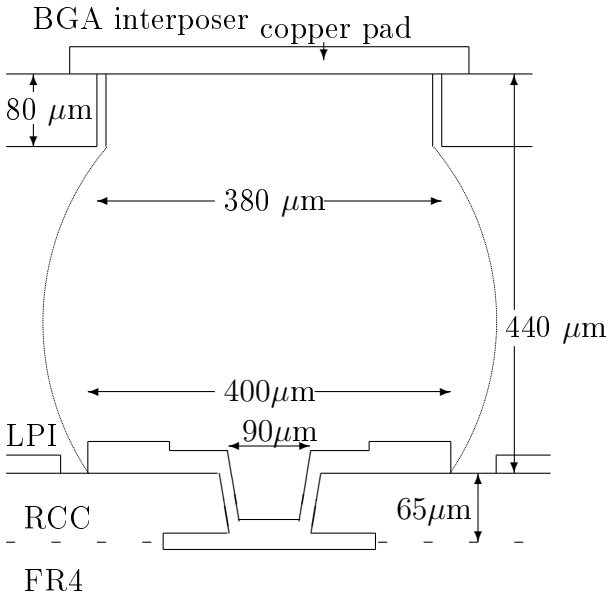

Figure 23 *Cross-section of the interconnections in the BGAs with micro-vias in pads.*

Fourier Transformation (Hewlett-Packard 3566A/67A FFT-analyser), and the natural frequencies were determined from the frequency response graph (see Fig. 25) as the frequencies of the peak values. The measured natural bending modes at different frequencies were computed from the measurements at different board locations (modal analysis program LMS Cada-X, ver. 3.5E SL1).

The measurements in the Laboratory for Mechanics of Materials were carried out with an accelerometer (Brüel & Kjær, Type 4383, 2.5 g) that was attached to the boards with beeswax at location A shown in Fig. 21. The short and light impact was

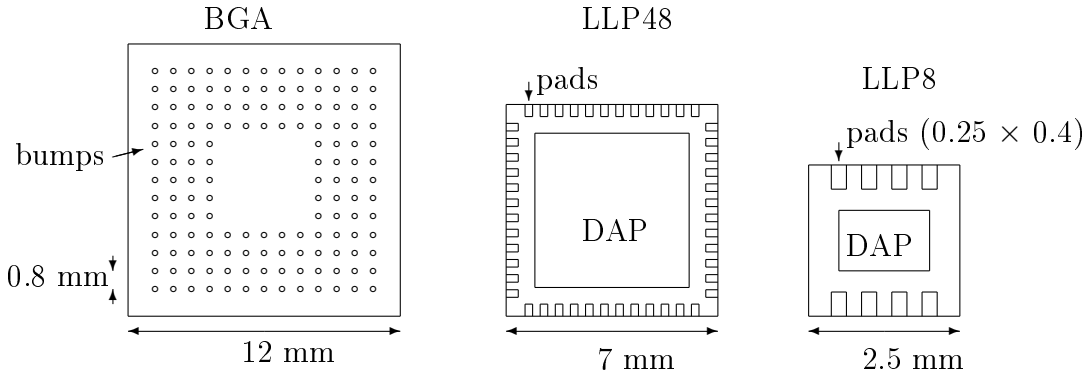

Figure 24 *Bottom views of the BGA, LLP48, and LLP8 components.*

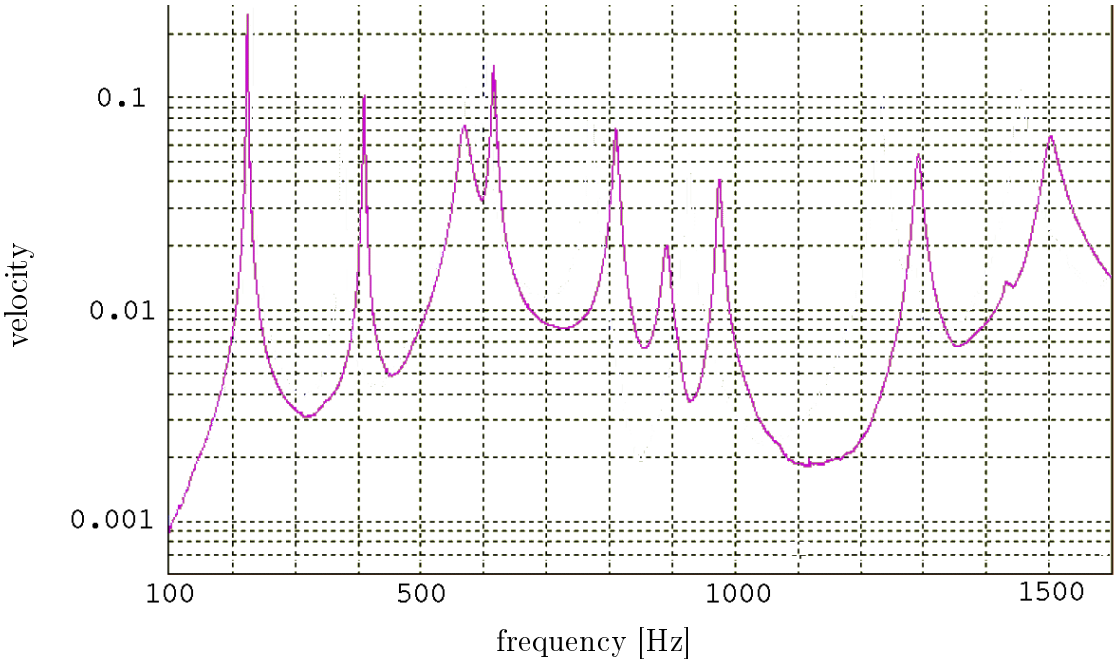

Figure 25 *Vibration velocities at different frequencies.*

Table IV *Measured natural frequencies [Hz] of the 0BGA and 15BGA boards with and without the accelerometer.*

	mode							
	1	2	3	4	5	6	7	8
15BGA	223.5	409.3	568.6	615.8	810.3	891.3	974.8	1291
15BGA + accel.	226.8	413.0	484.8	578.4	768.8	882.9	926.4	
0BGA + accel.	235.5	387.6	475.7	586.6	728.7	783.6	876.4	1035

generated with an instrumental hammer. Using a contact-free vibrometer instead of an accelerometer would have been preferable, but in this case the vibrometer was employed only when the natural modes of the 15-component boards were being measured.

7.2.2 Measured frequencies & modes

The measured natural frequencies of the 0BGA and 15BGA boards up to 1 kHz are printed in Table IV. The components increase the mass of the component board, which results in the reduction of the natural frequencies, as predicted by (54).

The measured and computed modes are presented in Figs. 26 and 27. The colours in the computed modes represent the vertical displacement. The vertical displacement in the figures is scaled to values between -1 to 1. The modes do not tell the magnitude of the vibration (i.e. U_{zij} in (53) on page 29) but only the shape

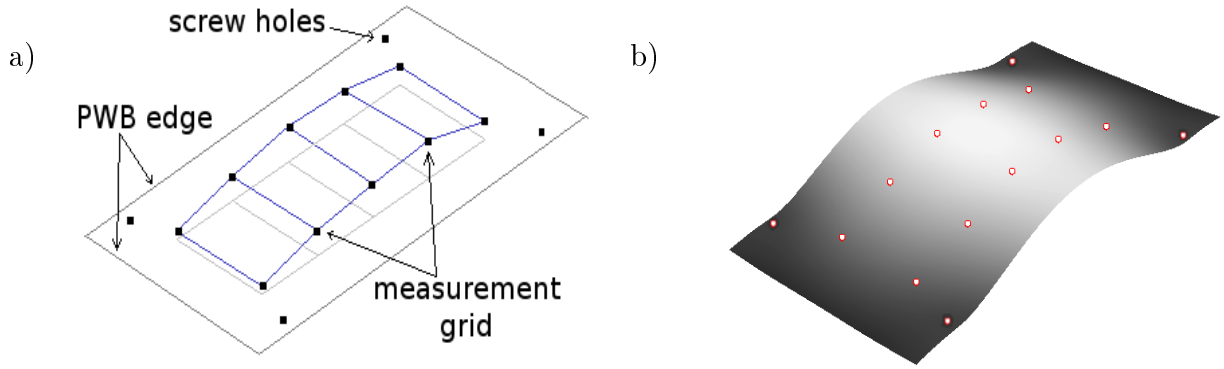

Figure 26 *First natural mode, a) measured, $f = 223.5$ Hz, b) computed, $f = 213.9$ Hz. The white circles in the computed plot refer to the black ones in the measured plot. The four black spots outside the measurement grid are the locations of the supports.*

(i.e. $\sin\frac{i\pi x}{L_x}\sin\frac{j\pi y}{L_y}$). In the JEDEC drop test the duration of the acceleration pulse is about 0.5 ms, which corresponds to about 1 kHz frequency. Therefore, if the natural frequency of a mode is about 1 kHz or less, the mode is expected to affect the bending during the drop test. Hence, the modes from 1 to 7 are important. The frequency of the mode 8 may be so high that the the loading does not excite it significantly. The first mode is the same as the static bending due to gravity, but the higher modes are less intuitive.

7.3 Measurements during the vibration testing

When a component board bends, the loading of the interconnections depends strongly on the curvature of the board, as expressed in (65) on page 33. The curvature can be evaluated by measuring the elongation on the board surface, see (68). Hence, the strains of the board during a test give a good impression of the magnitude of the loading. The bending amplitude is not as good measure, because the relation between the bending amplitude and the curvature depends on the vibration mode and the dimension of the board. However, the bending can be measured easily with contactless methods, which do not influence the bending.

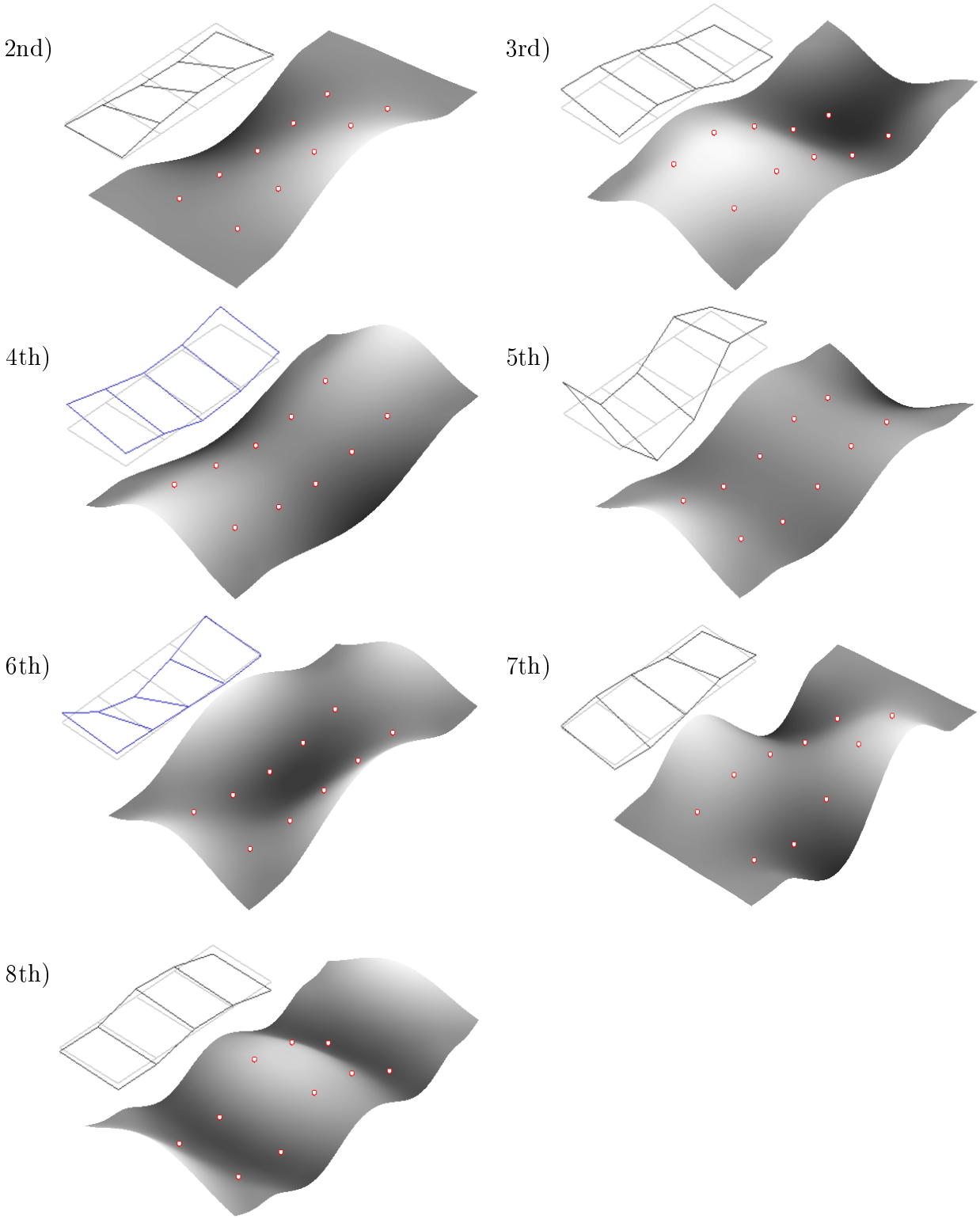

Figure 27 *Measured and calculated natural modes from the 2nd to the 8th mode.*

7.3.1 Measurement system

The vibration of a board in the vibration test was measured either by laser or by strain gauges. The vibration was generated using a system consisting of a computer with a signal generator (Microstar DAP 5200a), a signal amplifier (Brüel & Kjær, type 2700, 700 W), and a shaker (Brüel & Kjær, permanent magnet body type 4805, mode study head type 4814). The laser measurements were carried out by using a computer, a signal generator and measurement unit (Microstar DAP 5200a), and a laser system (SUNX, HL-C1C-M, HL-C105B-8K). 200 data points per period were recorded, with the exception of the laser, which recorded 10 data points per millisecond. Strain gauge measurements were carried out by using biaxial strain gauges (strains in the x and y directions, size 2 mm $\times$ 2 mm) that were attached to the surface of the board. The strain gauge measurements were carried out with the 0BGA boards. The locations of the strain gauges SGA-SGD, SG3 and SG4 are shown in Fig. 21 on page 55. The gauges were on the microvia side of the test board except at location SGA, where a gauge was also attached on the no-microvia side. Three or four gauges were used simultaneously for collecting the strain data. Strain readings were stored 50 times in a millisecond with the measurement system consisted of a data acquisition card (National Instruments PCI-6052e) and a strain measurement card (National Instruments SCXI-1520/SCXI-1314).

The bending of the assemblies was measured by using one or two laser heads. One head recorded the vertical displacements of the centre of the assembly, and the optional second head recorded the vertical displacements of one of the screw joints. The phase difference of the displacements was not measured, and thus accurate bending amplitude values could not be measured.

7.3.2 Shaker

The shaker consists of a set of permanent magnets and a coil, through which the amplified excitation current is conducted, see Fig. 28. The magnets are attached to the body of the shaker, while the mounting table and the coil are suspended from the springs. According to the shaker manual [Brü], the force generated between the

magnets and the coil is

$$F_B = BL_c I_e = BL_c \frac{U_e}{R} = \frac{BL_c}{R} U_e \tag{90}$$

where F_B is the magnetic force, B is the magnetic field of the permanent magnet, L_c is the length of the coil, I_e is the excitation current, R is the resistance of the coil, and U_e is the excitation voltage. Thus, the magnetic force and, hence, the acceleration of the mounting table (i.e. the excitation of the test structure) depends linearly on the excitation voltage.

The test assemblies were fastened from the four corner holes to a fixture that was made of four steel bolts and a sandwich plate (Fig. 28c). The fixture was connected to the shaker from the centre of the plate using a bolt and two washers. The washer above the plate was 10 mm and the washer below the plate was 40 mm in diameter.

7.3.3 Properties of the sandwich plate

The sandwich plate has two thin sheets on its surfaces and a honeycomb structure to keep the sheets apart from each other, see Fig. 28b. The structure is effective when lightweight and rigid plates are needed. The size of the plate was 126 mm × 90 mm, the thickness 4.6 mm, and the mass 13 g. There were four steel bolts in the corners of the plate to which the board was attached. The ends of the bolts were 10 mm above the surface of the plate, and the bolts were 6 mm in diameter. The total mass of the plate and the bolts was 44.1 grams.

In order to determine the apparent elastic modulus of the sandwich plate the resonance frequency of the plate was measured and compared to the one computed with the FE method. In the measurement no circuit board was attached to the sandwich plate. In the FE analysis the sandwich plate was assumed to be isotropic and homogeneous to reduce the number of variables. The strain amplitudes measured at different vibration frequencies are shown in Fig. 29. The amplitude of the excitation signal was 0.2 V. The natural frequency is approximately 375 Hz. According to the FE analysis this corresponds to the apparent elastic modulus value of 8.5 GPa.

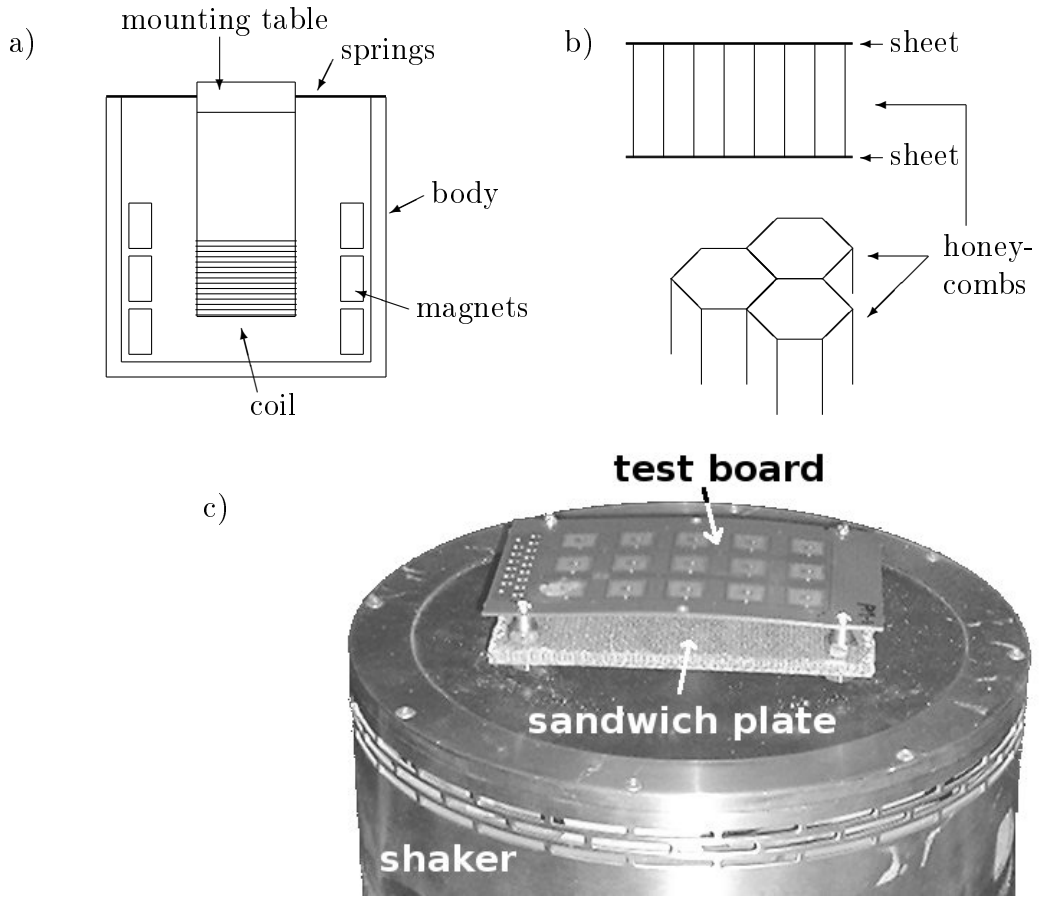

Figure 28 *a) Schematic picture of the shaker. b) Cross-section of the sandwich plate. c) Test board attached to the shaker.*

7.3.4 Measured vibration amplitudes

In order to evaluate how large vibration amplitude is generated at different frequencies, the vertical displacement of the 1BGA board was measured as a function of the excitation frequency. The excitation frequency was changed from 190 Hz up to 790 Hz, while the excitation amplitude was 0.2 V. The frequency scanning was carried out in 5-Hz to 10-Hz steps, and at each frequency the loading lasted for 30 periods in order to stabilise the vibration amplitude. Fig. 30 shows the measured displacements during the frequency scanning. The frequency that generated the first peak in the measurements is 230 Hz. The second peak is at 430 Hz and the third is at 650 Hz. The frequencies are somewhat different from the measured natural frequencies because: *i)* the component board was attached to the sandwich plate during the vibration; *ii)* the displacements were measured in the centre, and thus only the modes that generate vertical displacement in the centre are recognised, and

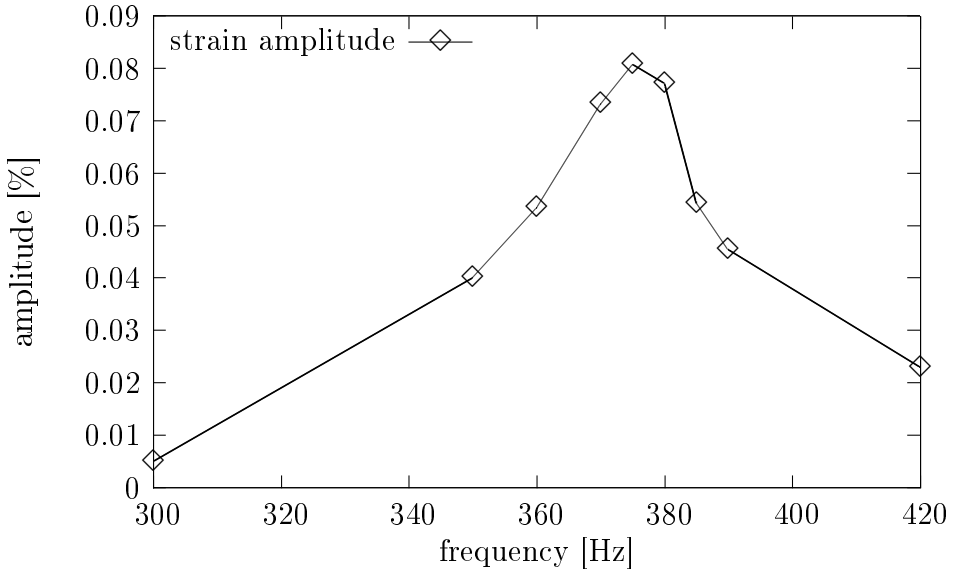

Figure 29 *Measured strain amplitudes of the sandwich plate at different loading frequencies with the 0.2-V excitation signal.*

iii) only one component was mounted on the board. The amplitude diminishes as the frequency increases because the higher-frequency modes require more energy for the same amplitude. The first mode is also the simplest mode, and using that in the vibration test results in a rather uniform loading of the interconnections along the outermost row parallel to the short board edge of the component C8. In addition, the first mode dominates bending during the drop tests (see Chapter 7.4). Therefore, the first peak frequency was chosen for the vibration tests.

The effect of the excitation amplitude on the displacement amplitude was evaluated next. The excitation amplitude was increased from 0.2 V to 0.6 V and to 1.8 V, and at each excitation level the frequency was changed from 190 Hz to 240 Hz in 5-Hz steps. After excitation at 1.8 V the board was excited again with a 0.2-V signal to detect possible changes in the board during the test. The results are plotted in Fig. 31. When the bending amplitude increases, both the internal damping and the membrane stresses in the board increase. The former reduces the resonance frequency and the latter increases it. In the current test structure the increasing damping has a stronger influence, and the frequency generating the largest displacement diminishes. The effect is rather small, and more importantly, does not affect the vibration mode. Therefore, it is not necessary to change the excitation frequency as a function of the excitation amplitude.

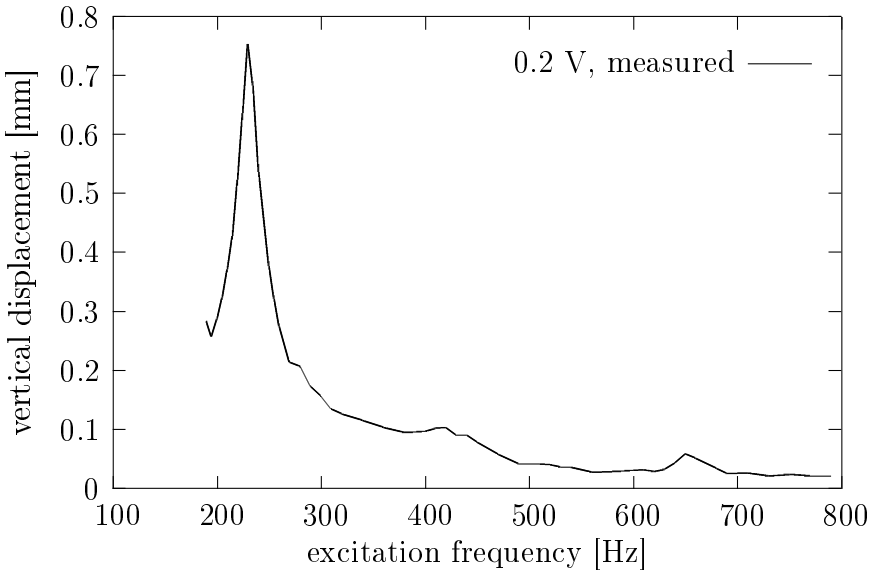

Figure 30 *Measured displacement amplitude at the centre of the 1BGA board as a function of the excitation frequency. Excitation amplitude 0.2 V.*

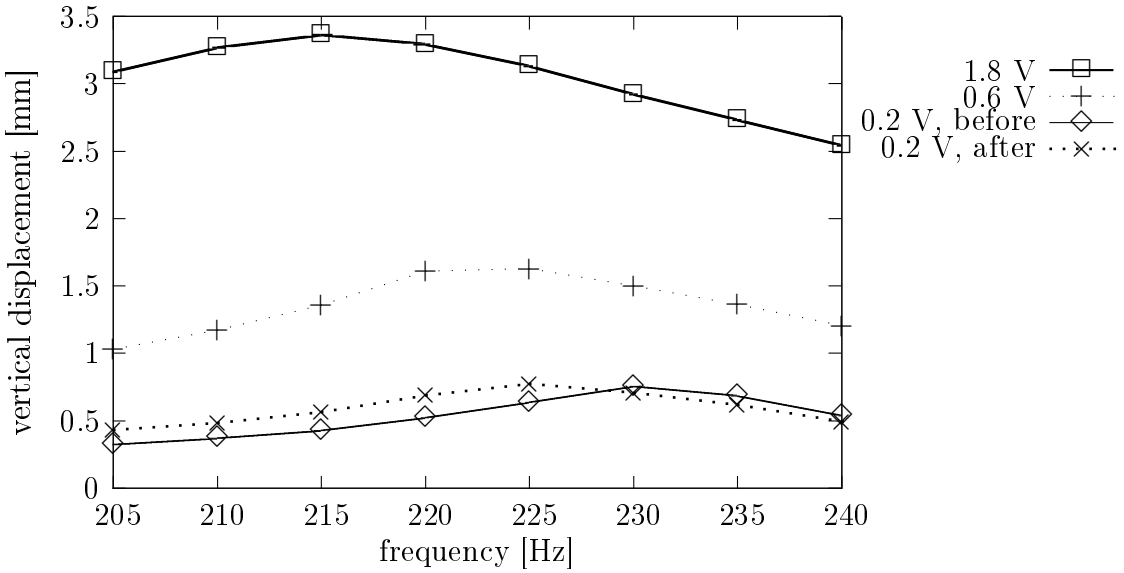

Figure 31 *Measured displacement amplitudes of the board centre when the excitation amplitude is 0.2 V, 0.6 V, 1.8 V, and 0.2 V again (1BGA board).*

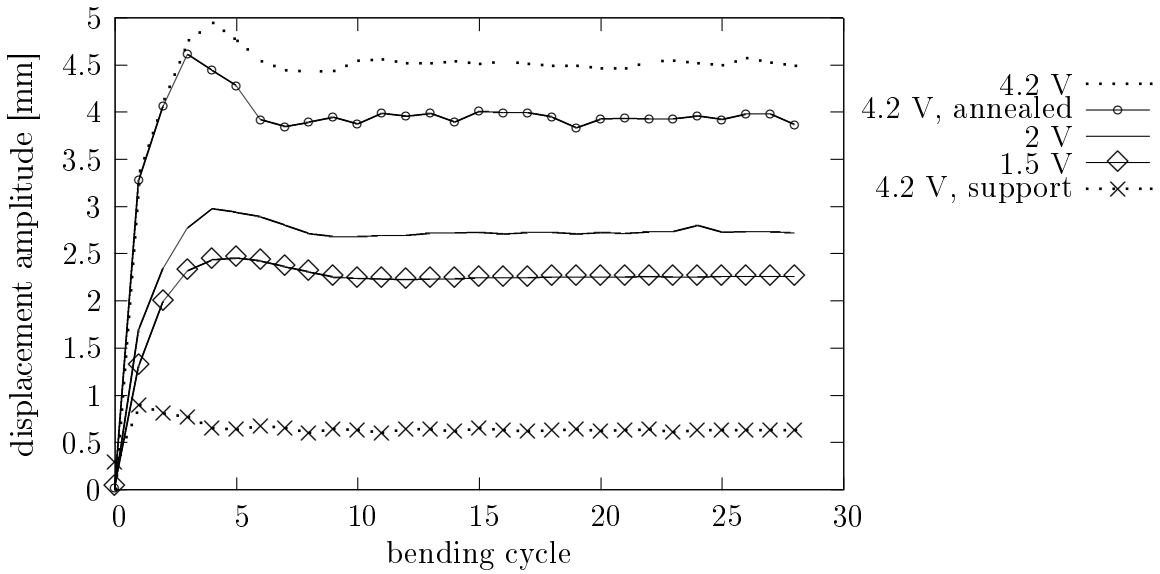

Figure 32 *Measured displacement amplitude values as a function of cycle number with excitation voltages 1.5 V, 2 V, and 4.2 V (1BGA board).*

During the reliability analysis part of the work, the test assemblies were loaded until there was an interconnection failure using a 233-Hz excitation frequency and three excitation amplitudes: 1.5 V, 2.0 V, and 4.2 V. Typical measured displacement amplitude histories at the centre of the board are plotted in Fig. 32, together with the measured vertical displacement of the screw joint during the 4.2-V loading. The displacement amplitudes increased during the first couple of periods, after which the amplitude stabilised to a slightly smaller value than the maximum one. After the first few cycles the amplitude remains constant providing constant loading cycles. The annealing seems to change the properties of the boards possibly by continuing the curing processes of the polymers. The amplitude of the screw joint is approximately 15 % of that at the centre, and hence, there is only a small difference between the bending and displacement amplitudes. The measured amplitudes for each tested component board are given in Table B-I in Appendix B.

7.3.5 Measured strains in the vibration test

The strains on the 0BGA board were measured when it was vibrated using different excitation signal amplitudes and frequencies. Fig. 33 shows the strains measured with a 230-Hz frequency and 2.5-V excitation amplitude. The strain amplitudes in drop tests (Chapter 7.4) and in vibration tests are close to each other, from 0.2 %

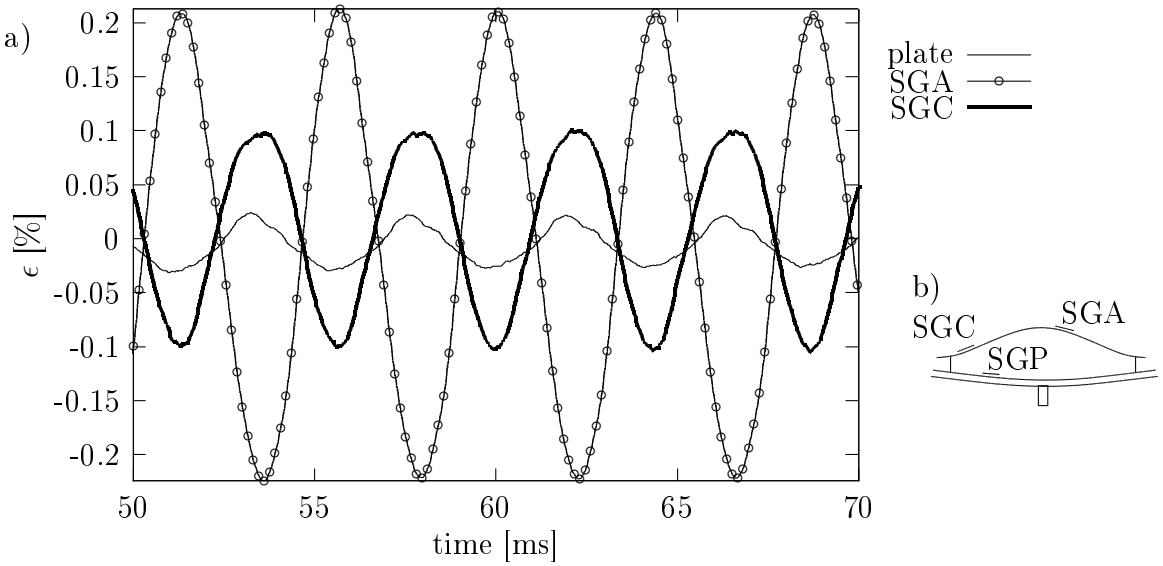

Figure 33 *a) Measured longitudinal strains of the 0BGA board (SGA and SGC, upper surface) and the sandwich plate (SGP, upper surface) when excitation signal amplitude was 2.5 V and frequency 230 Hz. b) Schematic plot of the board and the sandwich plate during the vibration.*

to 0.3 %, but in vibration tests a smooth harmonic strain history can be achieved.

The strain gauges used for Fig. 33 were on the upper surfaces of the plate and the board. From the plot it can be seen that the phase difference between the board and the plate is approximately zero. Hence, the supports and the centre of the board are at their uppermost positions almost at the same time. Thus, the bending amplitude of the board can be computed by subtracting the displacement amplitudes of the supports from those of the centre.

When the bending amplitude is small, the response of the board is accurately described by a sine function, but under strong loading the response is not as close to the wanted response; see Fig. 34, where a higher frequency vibration has a rather significant effect on the measured strains. It seems that the strain energy in the board increases to such a high value that another vibration mode is activated. Small asymmetries in the test structure and the asymmetrical placement of the strain gauge cables make the structure more prone to this kind of behaviour. An interesting point is that the oscillation is very close to what is measured in the drop tests.

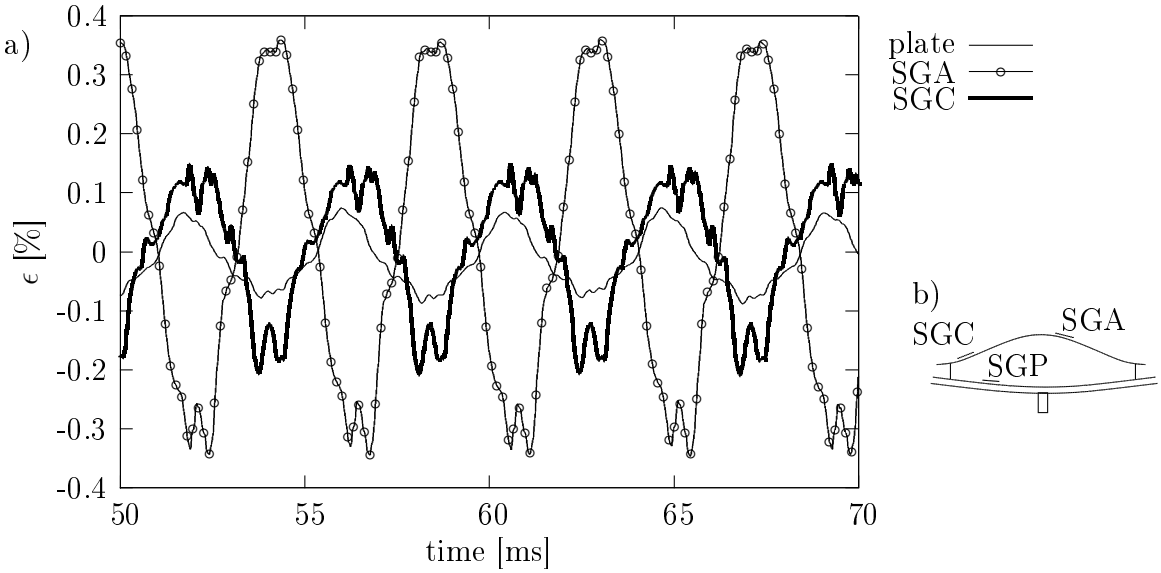

Figure 34 *a) Longitudinal strains of the 0BGA board (SGA and SGC, upper surface) and the sandwich plate (SGP, upper surface) when excitation signal amplitude was 4.5 V and frequency 230 Hz. b) Schematic plot of the board and the sandwich plate during the vibration.*

7.4 Measurements during the drop tests

Contactless measurement of the bending during the drop test could not be carried out because the drop table falls about 80 cm before the impact, and the range for the laser used in the vibration tests was ± 5 mm only. Therefore, the deformation of the drop tested component boards could only be measured with strain gauges, which have a small influence on the bending behaviour. The strains were measured with the equipment described in Section 7.3, and the acceleration of the drop table with an accelerometer (Kistler, type 8704 B5000) and a data acquisition card (National Instruments PCI-4474).

7.4.1 Measured strains in the drop test

The maximum strains occurred 1.5 ms after the impact started; see Fig. 35, where a typical deceleration history is plotted together with strain history graphs at location SG4 on the top and lower surfaces of a 0BGA board. When the sledge hits the strike surface, a stress wave is generated and the test board starts to vibrate. The delay is approximately a quarter of the period of the first natural mode, as predicted by dynamic analysis.

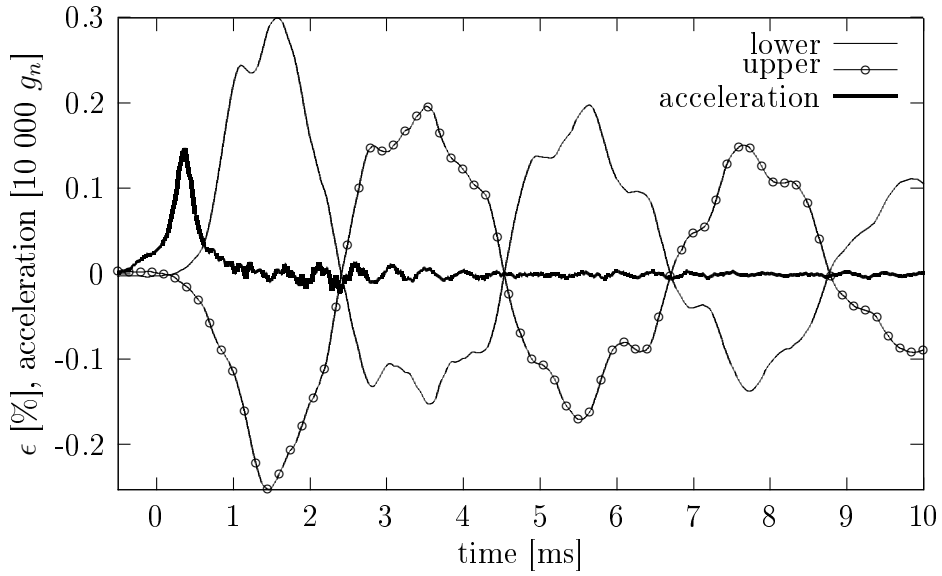

Figure 35 *Longitudinal strains on the upper and lower surface of the 0BGA (at the centre) after the impact, and the acceleration of the drop table.*

The strains in the x and y directions on the 0BGA at locations SGD, SGA, SGC, and SGB are plotted in Fig. 36. The first natural mode; see Fig. 26 on page 60, generates large tensile strains in the central area of the board on the surface facing down and large compressive strains near the supports, if the supports prevent rotations. The measurements at locations SGA and SGB in the central area and at locations SGC and SGD show similar results, which indicates that the rotations at the supports are very small.

The measured strains at both sides of the 0BGA board at locations SG3 and SG4 were compared in order to detect how much the board elongates during bending. If boards bend significantly and the supports are rigid, the bending generates large tensile stresses in the middle plane of the board, which results in considerable differences between strain magnitudes at opposite sides. In addition, the elongation of the middle plane increases the vibration frequency; see (55). In Fig. 35 the tensile strains are approximately 20 % larger than the compressive strains, thus the boards elongate considerably during the bending.

Fig. 37 shows strains in 0BGA when 16 and 4 measurement cables were used (one cable per strain direction). During the first 10 drops 16 cables were used, and during the next 10 only 4 cables. The graph shows strains in the x direction at the beginning of the 10th and the 11th drop. The number of cables chiefly affects the

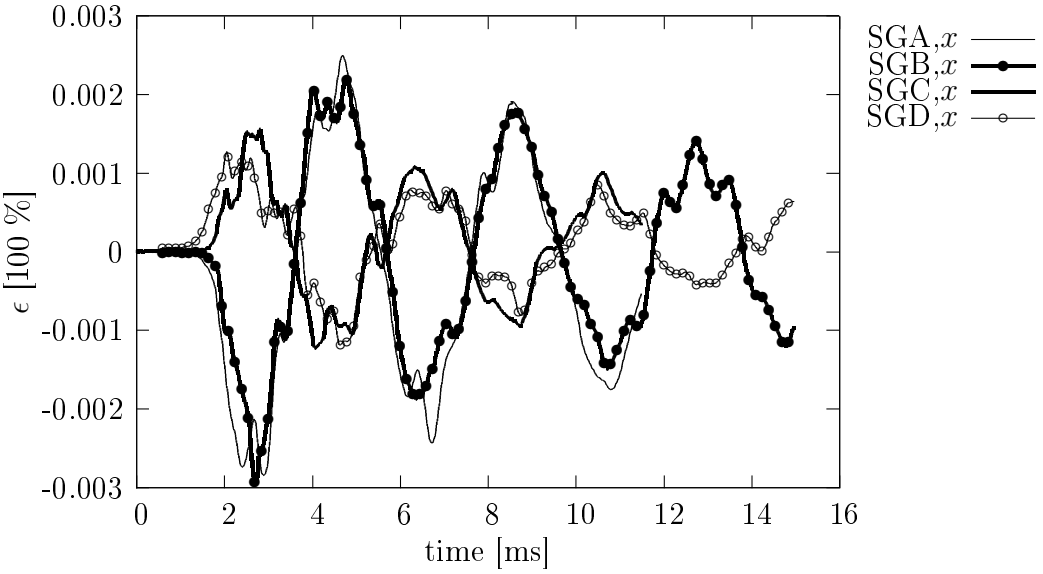

Figure 36 *Longitudinal strains on the upper surface of the 0BGA during the drop test.*

damping after the first bending cycle but not at the vibration during the first half bending cycle.

To evaluate how strong an effect the number of components mounted on the boards has on the board behaviour, the strains measured on the boards 0BGA, 1BGA and 15BGA at locations SG3 and SG4 are compared in Fig. 38. The measurements at location SG3 show that a single component has a negligible effect on the behaviour of the board outside the component location, but 15 components have a small effect. However, there is no marked difference in the loading of the middle component, whether 15 components or only one are mounted, according to the strain measurements.

In the drop test the component boards bend significantly and high stresses are generated in both the interconnections and the boards. The resulting cracks change stress distribution locally, but it is not known how significantly they affect the bending behaviour at the board level. Therefore, the measured longitudinal strains at locations SG5 and SG4 on the 1BGA board during the first, the fourth, and the 20th drop are presented in Fig. 39 together with strains at SG4 in the 0BGA board during the fist, the fourth, and the 10th or 20th drop. There seems to be no differences during the first bending, but vibration seems to dampen slightly faster after few drops. However, there is no change in the magnitude of the strain from the

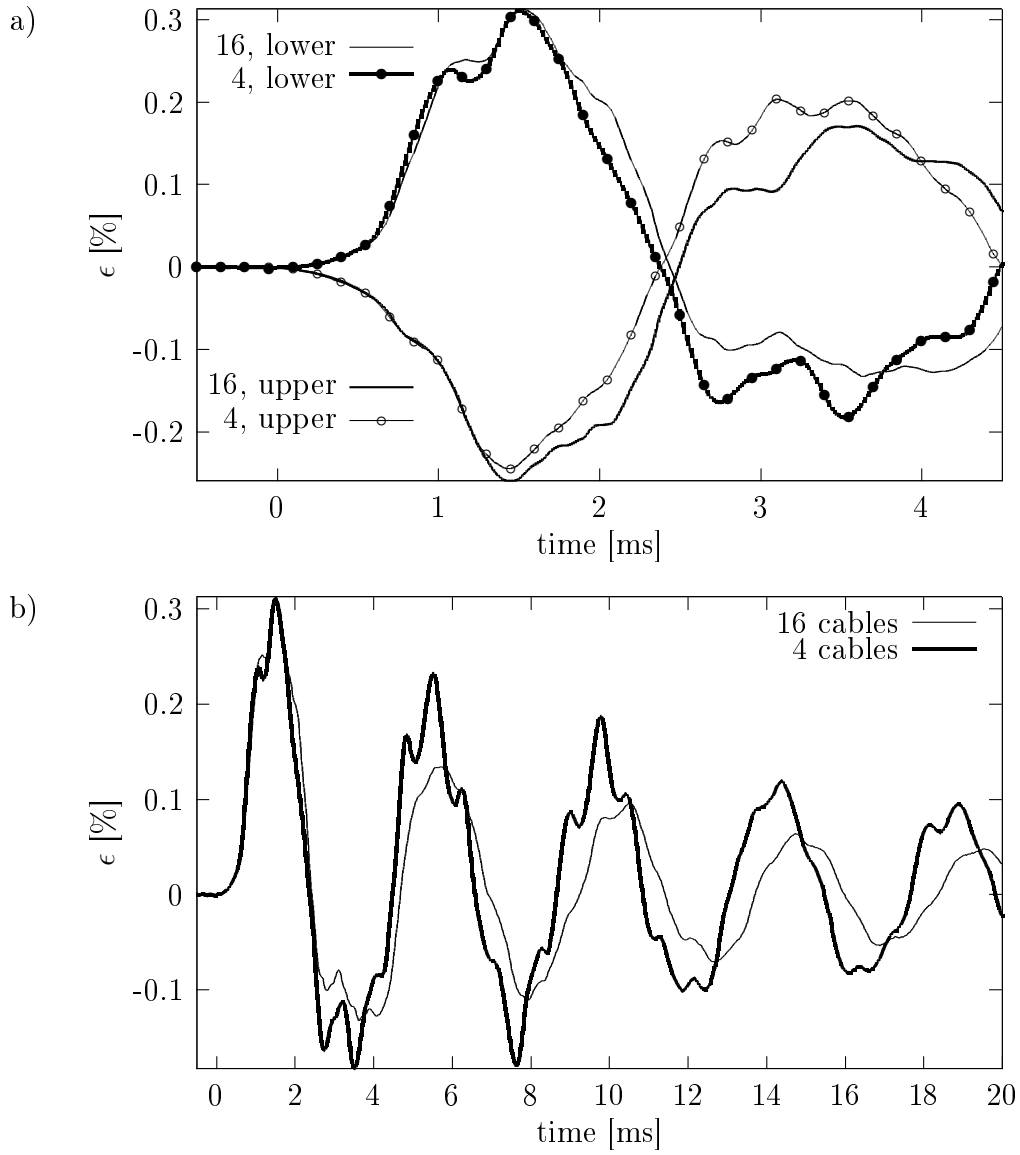

Figure 37 *Longitudinal strains on 0BGA when 4 and 16 cables were attached: a) the first period, b) the first 20 ms.*

first drop to the 20th drop, which indicates that during the 30 drops of the JESD22-B111 standard the loading of the interconnections does not change markedly. It was also detected that the daisy chain had failed during the measurements, but the failure did not affect the magnitude of the first bending.

7.4.2 Effect of drop height

The effect of the drop height on the vibration of the board was evaluated by using drop heights of 30 cm, 53 cm, and 95 cm. The measured strains of SGA are plotted in Fig. 40. The generated accelerations were 200 g_n, 500 g_n, and 1800 g_n. The

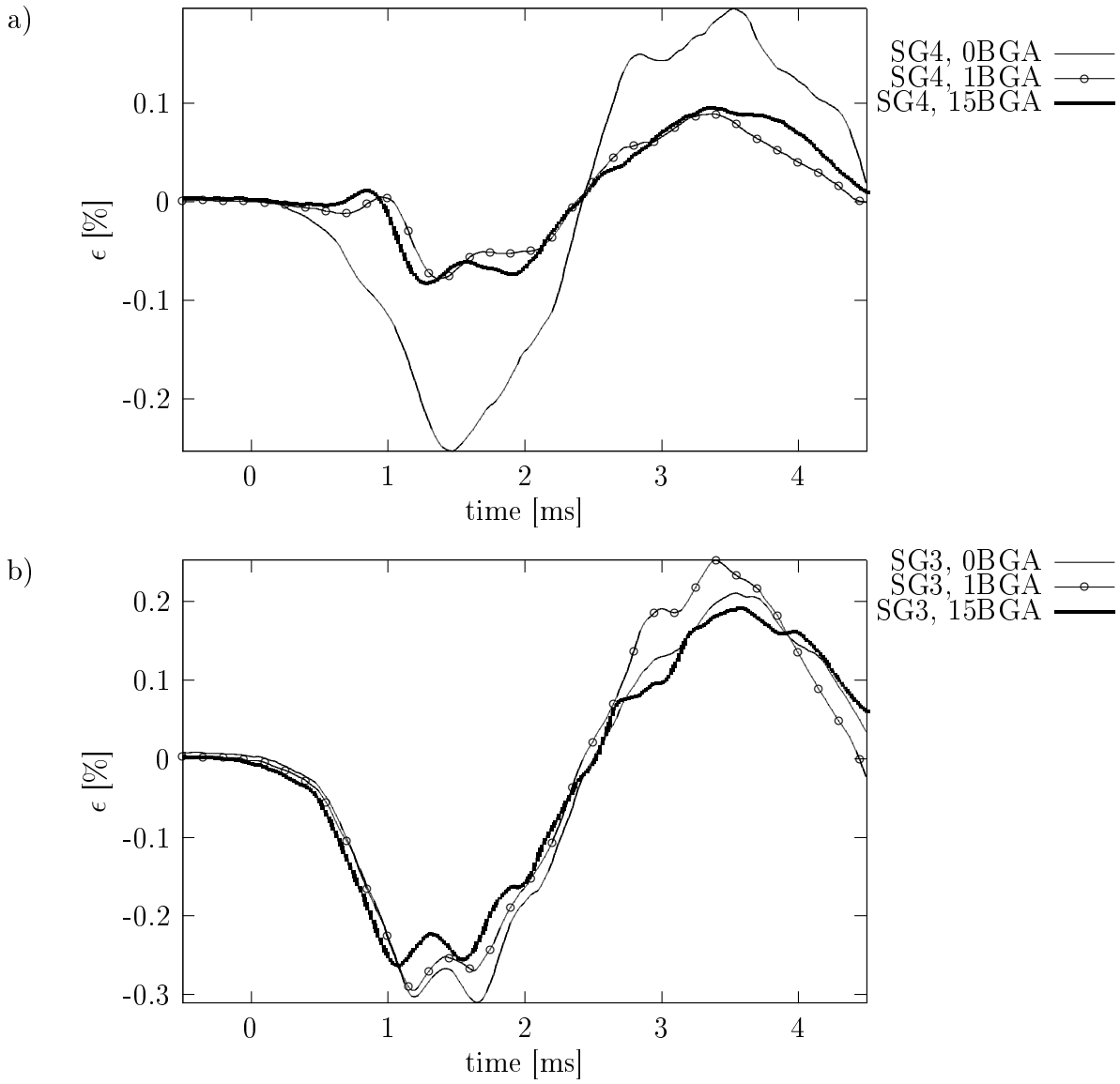

Figure 38 *Measured longitudinal strains on the 0BGA, 1BGA and 15BGA boards at locations a) SG4 (at the centre) and b) SG3 (in the middle of the long edge).*

reduction in the amplitude of the impact reduces the effect of the higher modes, and only the first mode could be observed when the 200-g_n impact was generated. The magnitude of the strains is not strongly dependent on the acceleration: the reduction of the deceleration from 1800 g_n to 200 g_n (by 89 %) reduced the strain amplitude from 0.31 % to 0.18 % (by 42 % only). A shorter falling distance also changed the acceleration generated: the 200-g_n pulse widened and lasted approximately 3 ms instead of 0.5 ms, which mainly explains the small reduction in the strains. From the half period length of the 200-g_n impulse one can calculate that the frequency

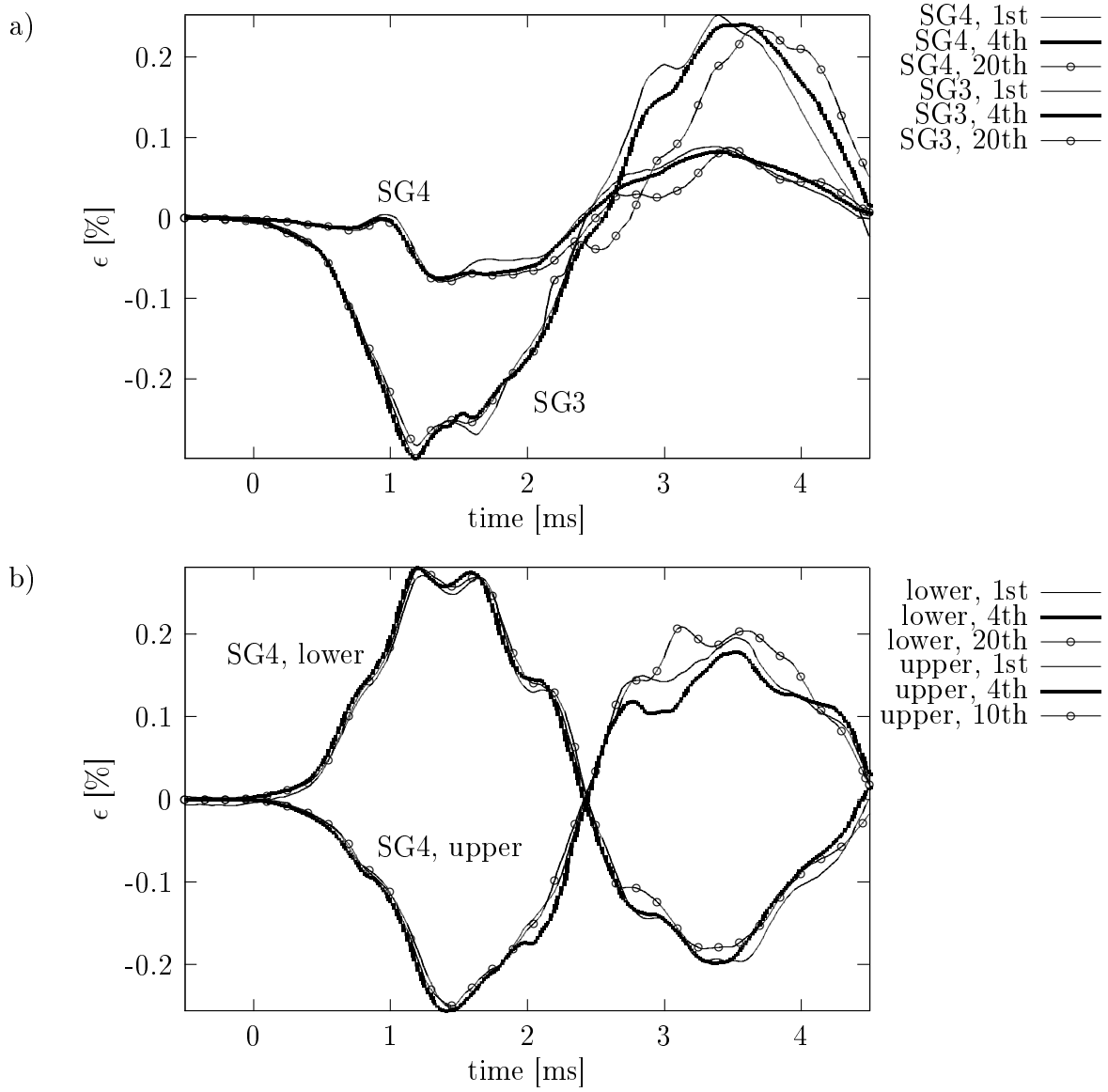

Figure 39 *Longitudinal strains a) on 1BGA at locations SG3 (in the middle of the long edge) and SG4 (at the centre) during the 1st, 4th and 20th drops, and b) on 0BGA on both surfaces at location SG4.*

of the impulse is approximately 170 Hz, which is below the first natural frequency of the board. Thus, the strain history is smooth and does not contain components from the higher frequency modes.

During the failure analysis - see Chapter 8 - it was noticed that the vibration with a 2-V excitation amplitude resulted in cracks in the intermetallic layers, but with a 1.5-V amplitude cracks propagated in the bulk solder. Fig. 41 shows strains in SGA during drop testing from a 30-cm height and during vibration with a 1.5-V amplitude at 232 Hz. The maximum strain amplitude of the drop tested board is

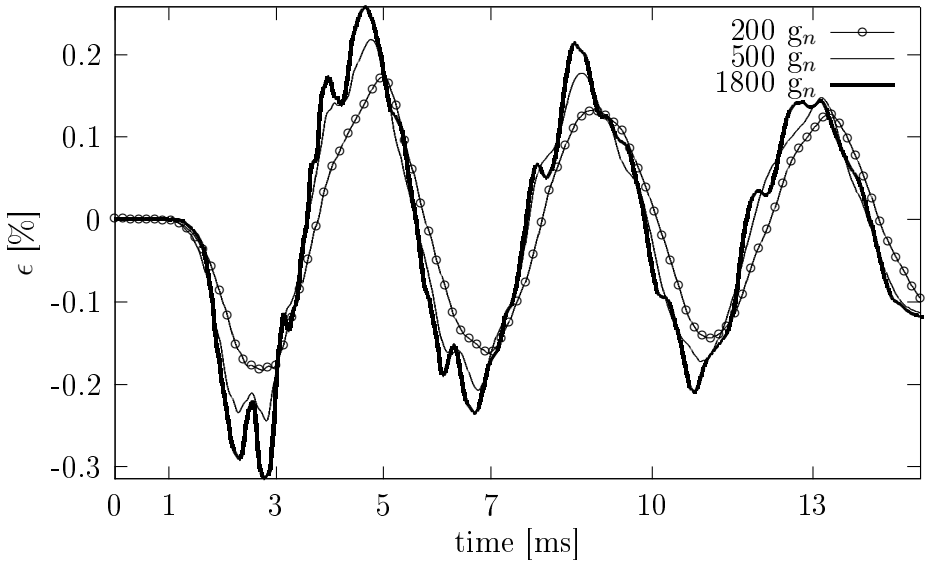

Figure 40 *Longitudinal strains on a board at different drop heights.*

slightly larger than that of the vibrated one; thus, it seems that for generating bulk solder failures in the component boards the drop height needs to be very low.

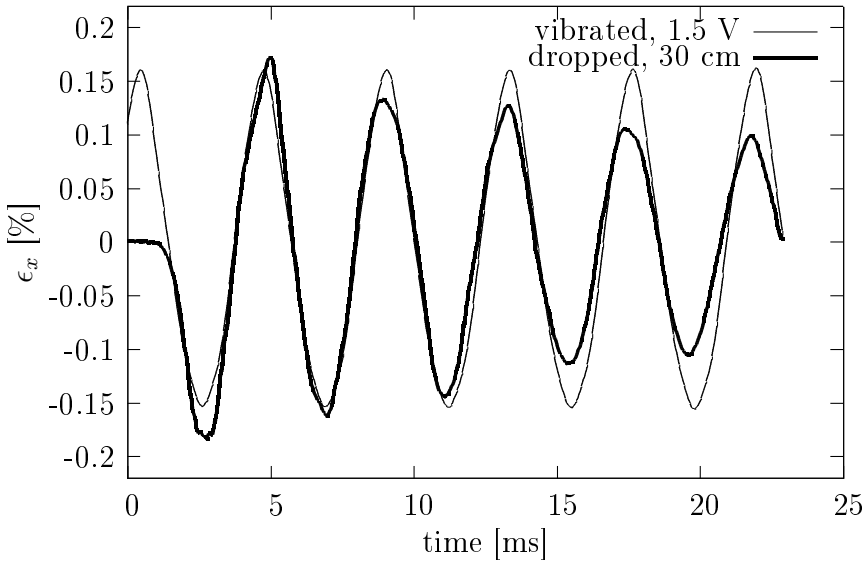

Figure 41 *Longitudinal strains in SGA during drop test from 30 cm and vibration test with 1.5-V signal.*

8 Results from the reliability tests

The failure modes of the vibrated component boards (layout in Fig. 21 on page 55) were inspected and compared to those observed in drop tests. If the vibration test method is going to be used in addition to or instead of the drop test, the same failure modes should be found.

The frequency of the excitation signal during the tests was 233 Hz and the amplitude was 4.2 V. Three different surface finishes were used in the BGA boards: OSP, Ni(P)|Au, and matte Sn. The number of the 1BGA boards was 45: 21 Sn, 12 OSP, and 12 Ni(P)|Au. Nine of the tin finished 1BGAs were annealed at 120 °C for 500 h before testing for evaluating the effect of the Kirkendall voids. In the vibration tests the number of the fully populated boards was smaller: 3 BGA boards, 2 LLP48 boards, and 3 LLP8 boards. The failure modes of the BGA boards were analysed, but those of the LLP boards were not.

The number of bending cycles to failure for each vibrated 1BGA board are presented in Table B-I in Appendix B and for the vibrated fully populated boards in Table C-I in Appendix C. The number of drops to failure are presented in Table C-II in Appendix C in the case of the drop-tested 15BGA boards. The pictures of the failure modes (Fig. 43 - 50) were taken from the vibrated component boards. Detailed studies of the failure modes in the drop-tested boards, where the same BGA component was used, are presented by Mattila *et al.* [06Mat1, 06Mat2, 06Mat3]. Failure modes found in other studies are in [05Ala, 02Arr, 05Cho, 04Lal], for example.

8.1 Failure detection method

In the vibration tests the resistance across the daisy chain components was measured by employing a system consisting of a constant volt source and an external 1-kΩ resistor (see Fig. 42). By measuring the resistance one can observe when a crack has created an open in the daisy chain by propagating through an interconnection or a trace. The daisy chain component and the external resistor were connected in series, and a voltage of 5 V was applied across them. By measuring the voltage across the resistor, the changes in the resistance of the daisy chain could be detected. The

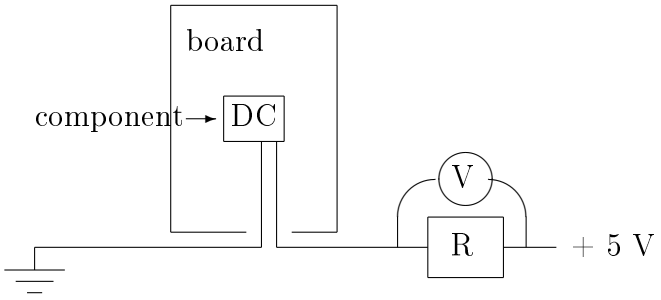

Figure 42 *Measurement system used to detect failures during the vibration test. DC - daisy chain component, R - external resistor, V - volt meter.*

resistance can be calculated by using the formula

$$R_{DC} = R_R \frac{U_0 - U_R}{U_R} \tag{91}$$

where R_{DC} and R_R are the resistance of the daisy chain and that of the external resistor, and U_0 and U_R are the voltages across the whole circuit and the external resistor. The voltage across the external resistor was measured 200 times per each cycle. The measurement system was able to measure 8 channels only; hence, in the case of the fully populated boards, the resistance of the components C1-C4 and C6-C9 only was measured.

Two methods were used to limit the duration of the measurements and signal generation: *i)* the number of cycles was given, or *ii)* loading and measuring were stopped when the voltage across the external resistor went down to 2.0 V, which corresponds to 2.3 kΩ in the daisy chain. With the first option the loading could be continued without interruption to verify that the resistance limit has been exceeded more than once during the loading. On the other hand, the number of bending cycles must be defined before the loading.

Changes in the daisy chain resistances during the drop tests were measured with an event detector (Analysis Tech's Event Detector, model 128/256 STD) that detects when the resistance exceeds a threshold value for a period longer than 200 nanoseconds. The threshold value was set to 1.5 kΩ.

8.2 Failures in the OSP-finished assemblies

In the assemblies where OSP was used as the surface finish, the solder was in direct contact with the copper pads on both sides of the interconnection, resulting in the layers of: *i)* solder; *ii)* solder + Cu_6Sn_5 protrusions; *iii)* Cu_6Sn_5, *iv)* Cu_3Sn, and *v)* copper. According to the thermodynamic equilibrium there should be a layer of Cu_3Sn between the Cu_6Sn_5 and the copper, but due to the slow growth of the Cu_3Sn layer it was not detected unless the interconnections were annealed.

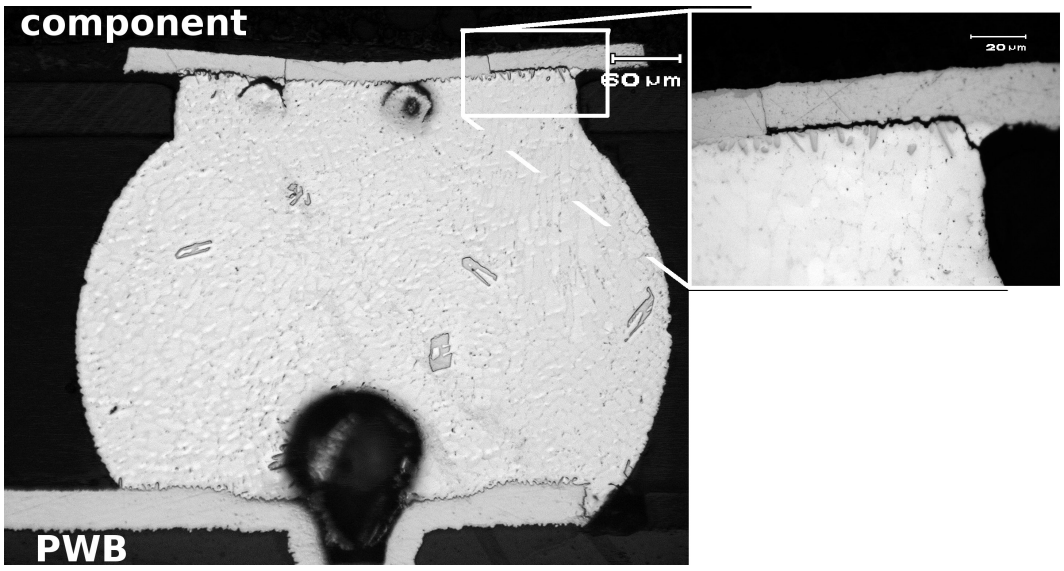

Figure 43 *Crack on the component side in an OSP specimen (excitation 4.2 V, 233 Hz).*

Fig. 43 presents a cross-section of an interconnection from a component board that was vibrated with a 4.2-V excitation. The crack propagated in the IMC layers on the component side near the bump edges. Then, closer to the centre of the bump, the crack jumped through the copper pad, propagated between the pad and the interposer, and returned back to the IMC layer. Cracks were detected most often in layers *ii)* or *iii)* on the component side, where the highest stresses are also located (see Fig. 67, page 110). Cracks often nucleated in solder near the corners, and sometimes also in the solder + Cu_6Sn layer, and propagated in the IMC layers. In some samples the crack path moved into the bulk solder for a short distance but remained mainly in the IMC layers. There was also a few interconnections where cracks propagated through the component side copper pad, as shown in Fig. 43. In

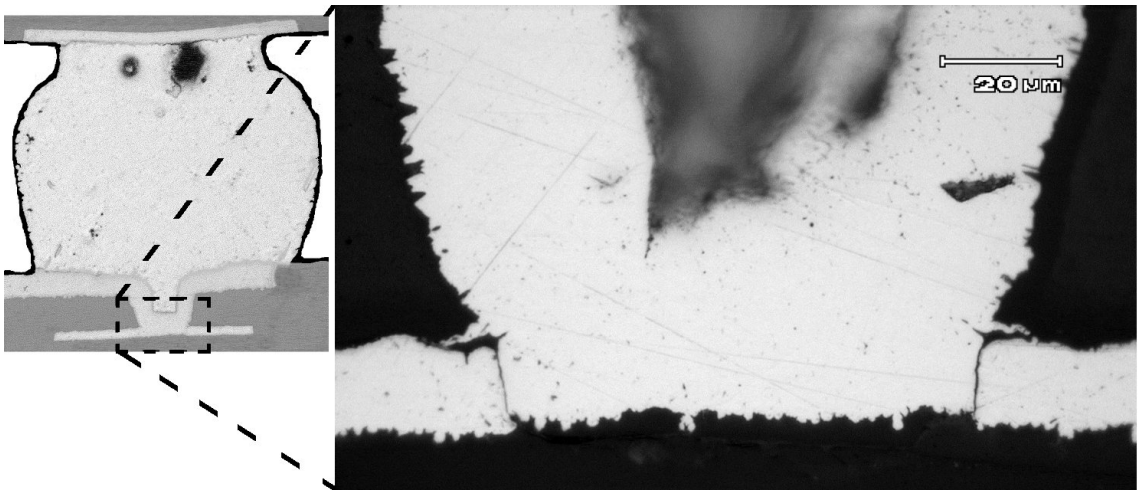

Figure 44 *Crack in the micro-via of the soldering pad in an OSP specimen (excitation 4.2 V, 233 Hz).*

almost every interconnection with microvia-in-pad, there was a relatively large void sitting on top of the via. Voids did not seem to influence the propagation of cracks, unless they were near the paths of the cracks. In that case the cracks deviated from their original planar paths only for a short distance as they propagated through the voids.

There were also cracks on the board side. Cracks in the RCC layer were very common. A fracture in the RCC layer does not cause electrical failure, unless it leads to trace failure, but it changes the stress distribution in the interconnection, making mechanical analysis more demanding and increasing scatter in the results. Occasionally RCC failure led to failure in the microvia. Fig. 44 shows a typical crack in microvias. The terminal pad failed where the via meets the pad. This type of interconnection failure leads to electrical failure, but in the test boards the daisy chain did not go through the vias, and this type of failure was not detected electrically. Cracks in the IMC layers on the board side were not as common as those on the component side. However, there were more such cracks on the board side that detached bumps clearly from the soldering pads than on the component side. Because the stresses on the board side should be smaller than those on the component side (see Chapter 9.5), the failures on the board side imply that occasionally the interface on the board side was weak. The same modes were also found in the drop tested boards.

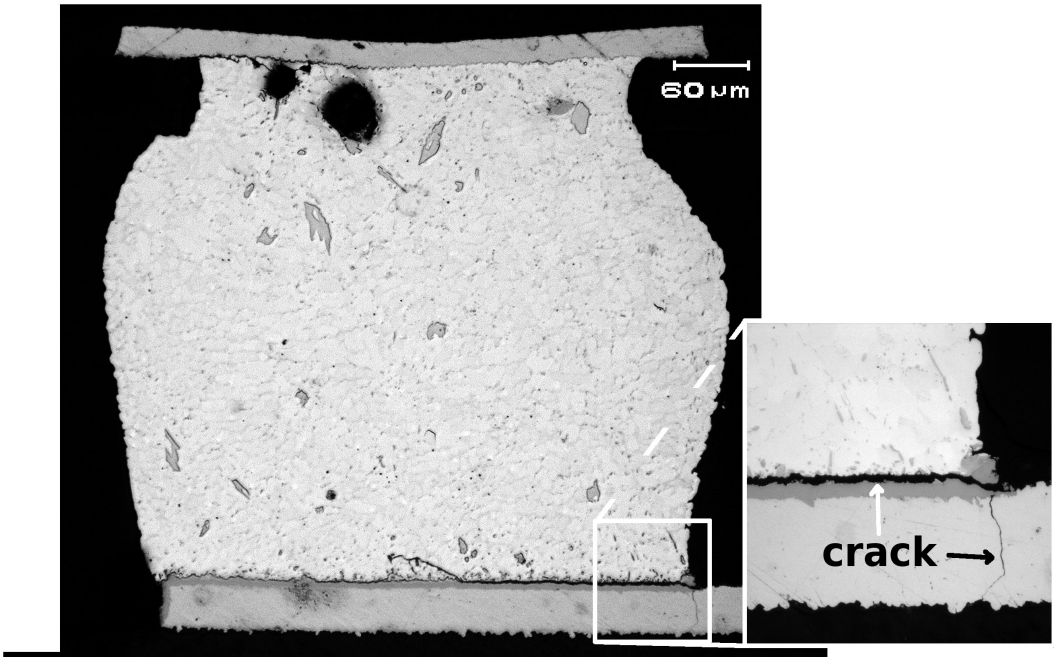

Figure 45 *Crack in a NiAu specimen in the reaction layer on the board side, and through the copper trace (excitation 4.2 V, 233 Hz).*

8.3 Failures in the NiAu-finished assemblies

On the component side the same reaction layers were found as in the OSP-finished assemblies, but on the board side the layers were different. The phosphorus in the Ni(P)|Au finish makes the reaction layers complex [05Laur, 02Mats, 06Vuo]. On the board side the layers are *i)* bulk solder, *ii)* $(Cu,Ni)_6Sn_5$, *iii)* porous NiSnP, *iv)* Ni_3P + Sn, and *v)* Ni(P).

Cracks in the NiAu assemblies on the component side were similar to those in the OSP assemblies: cracks propagated through the IMC layers occasionally visiting the solder. On the board side cracks were located in the RCC layer, in the solder/pad reaction layer (Fig. 45), and in the copper traces.

It has been found out that during the soldering process a thin layer containing nickel, phosphorus, tin, and a large amount of microvoids forms on the board side [05Laur, 02Mats, 06Vuo]. In drop-tested NiAu assemblies cracks in this layer were very common, and the crack propagation within this layer was found to be the primary failure mechanism [05Cho, 06Mat1]. However, in the vibration tests cracks in the reaction layer on the board side were not found to be more common than cracks on the component side.

Cracks in copper traces were located where the trace leaves the pad and the bulk solder comes into contact with the pad, a location where stresses concentrate.

8.4 Failures in the Sn-finished assemblies

Cracks in the Sn-finished assemblies were located in the IMC layers, RCC, and traces; like in the OSP samples. The reaction layers in the Sn and OSP assemblies should be the same because there are no additional elements. In the Sn assemblies the small amount of additional tin has no practical effect on the composition of the solder, and in the OSP assemblies the OSP finish should evaporate during the soldering process, leaving the copper in contact with the tin-rich solder. However, cracks in the IMC layers on the board side were more common in Sn assemblies than in the OSP assemblies.

8.4.1 Effects of the annealing

When the Sn assemblies were annealed (500 h at 120 °C), the thickness of the intermetallic layers was increased, and a large number of tiny voids (presumably Kirkendall voids [05Zen]) formed in the Cu_3Sn layer on the component side; see Fig. 46b. The voids formed a weak layer, along which cracks propagated quickly. The crack paths in the annealed samples remained within this weak layer, except near the corners, as in the drop tested samples. No propagation of cracks in other layers was observed except in corner areas. On the board side such voids were not observed, and cracks were detected only in the RCC layers and occasionally also in the copper traces. The RCC failure was common, but trace failures were not.

8.4.2 Effects of the bending amplitude

Three different loading amplitudes (4.2 V, 2.0 V, and 1.5 V) were used to find out the effect of the bending amplitude on failure modes. The resulting displacement amplitudes were 4.5 mm, 2.7 mm, and 2.3 mm. Cracks on the component side remained mainly within the reaction layers when the displacement amplitude was 4.5 mm or 2.7 mm, but reducing the amplitude to 2.3 mm caused a new failure mode: cracks propagated within the bulk solder; see Fig. 47. On the board side the

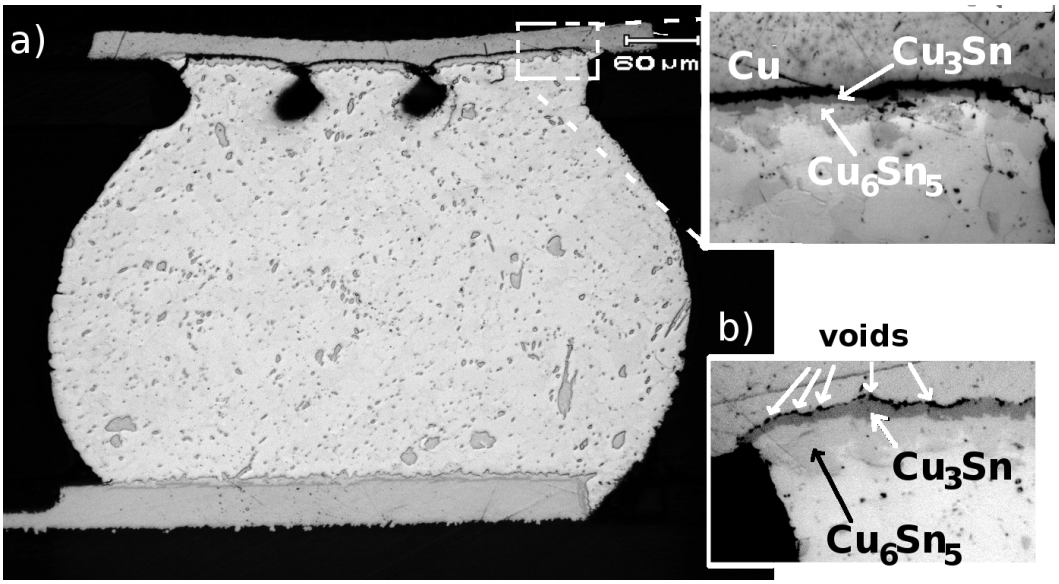

Figure 46 *a) Crack through the porous Cu_3Sn layer (excitation 4.2 V, 233 Hz) in an annealed specimen. b) Voids in an inner bump.*

only difference was that no trace failures were detected in the cases of 2.7-mm and 2.3-mm amplitudes. RCC failures and IMC failures on the board side were detected regardless of the bending amplitude. RCC failures were common and IMC failures occasional.

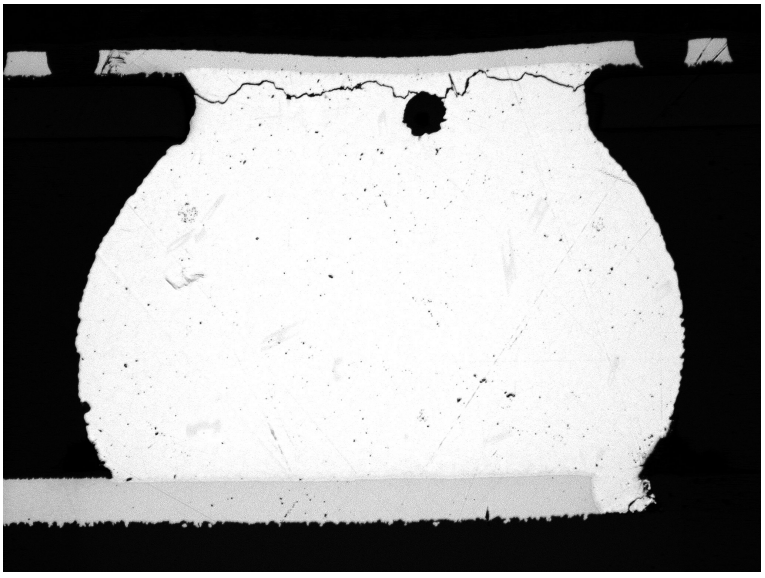

Figure 47 *Crack through solder in a Sn specimen (excitation 1.5 V, 233 Hz).*

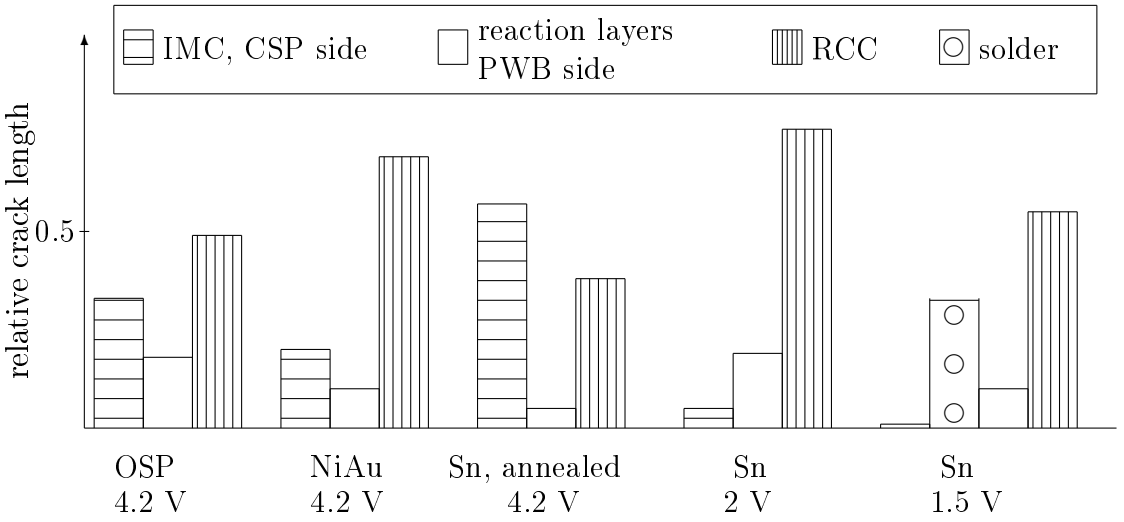

Figure 48 *Relative lengths of cracks in the outmost interconnection rows of component C8.*

8.5 Relative crack lengths in the interconnections

The lengths of cracks in different parts of interconnections were measured with optical microscopy from the cross-sectional samples. In Fig. 48 the relative lengths of cracks in the central component are given, the sum of different types being 1. The crack lengths were measured from the outermost row of interconnections (13 interconnections per row). For each assemby type four or five components were studied. Half of the rows were parallel and half perpendicular to the short board edge. There were significantly more cracks in the interconnections on the row parallel to the short edge than on the other.

8.6 Microstructures of the solder joints

There are usually only a couple of colonies in interconnections after solidification; see Fig. 49. In thermal cycling solder has been found to recrystallise, thereby generating grain boundaries along which cracks can propagate [06Mat2]. In drop-tested or vibrated samples recrystallisation has not been observed. When recrystallisation is considered, there are two important differences between thermal cycling tests and drop and vibration tests: temperature and loading time. Drop and vibration tests are usually carried out at room temperature, while temperature changes during

thermal cycling (between -40°C and 125 °C in [06Mat2]). Typical durations of loading cycles in vibration tests are 4 ms (0.8 s for 200 cycles), in drop tests 8 s (5 min for 40 drops), and in thermal cycling 0.5 h (3 weeks for 1000 cycles). Thus, in drop and vibration tests there is very little time for recrystallisation. In addition, temperature has strong influence on the recrystallisation and the recovery; therefore, cyclic thermal loading may initiate recrystallisation easier than isothermal loading at room temperature.

Figure 49 *Polarised light image of an interconnection. Areas of similar grey have a similar crystal orientation.*

When the excitation amplitude was reduced to 1.5 V (2.3 mm displacement) cracks propagated through the bulk solder. Fig. 50 shows polarised light images of a joint in such a component board. There seems to be 6 areas of different orientation, one of which is clearly distinguished, and no sign of recrystallisation is visible along the crack path.

8.7 Effect of the component location

The effect of the component location on the time to failure was studied by carrying out vibration tests with fully populated boards. The boards were loaded for 600 or 1200 cycles. The lifetimes of the vibrated ones are presented in Table C-I in Appendix C and those of the drop tested ones in Table C-II. To compare the

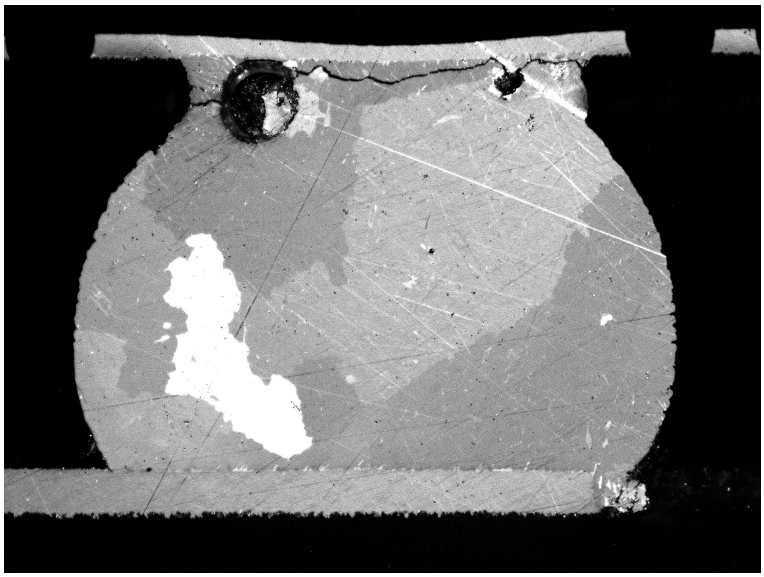

Figure 50 *Polarised light image of a specimen vibrated with 1.5-V excitation amplitude.*

lifetimes of components in different boards, the lifetimes were normalised by dividing the lifetime of each component by the lifetime of the centre component (C8) of the board. The average normalised lifetimes of different assemblies in the drop and vibration tests are presented in Fig. 51 together with the percentage of the failed components. The components that did not fail are not taken into account in the normalised lifetime except in the case of the component C6, where no components failed. The value was calculated by dividing the total amount of bending cycles by the average lifetime of C8. The components were grouped into the six groups defined earlier on the basis of the component locations (grouping: *i)* C1, C5, C11, and C15, *ii)* C2, C4, C12, and C14, *iii)* C3 and C13, *iv)* C6 and C10, *v)* C7 and C9, and *vi)* C8). In both test methods the order of the component locations was the same: the components to fail first are in column 3 (groups *iii* and *vi*), then in column 2 (*ii* and *v*), and the last ones to fail are in column 1 (*i* and *iv*). The components in columns 1 and 2 have shorter relative lifetimes in the drop test than in the vibration test, but otherwise the effect of the location is similar. This supports the assumption that the first mode generates the highest stresses and is the primary cause of failures. If higher modes were important, the distribution in the vibration test at the first frequency would produce a different distribution from that in the drop test.

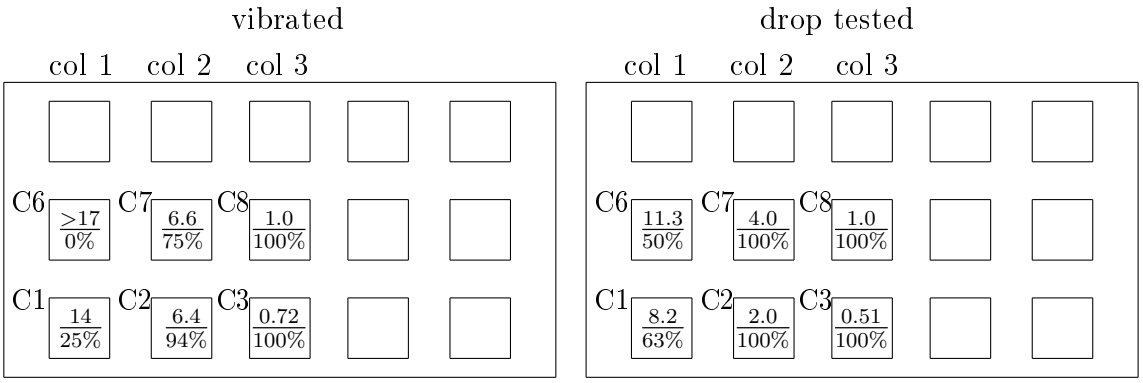

Figure 51 *Relative lifetimes and the percentage of the failed components in the vibrated and drop tested component boards. The lifetimes are given in Tables C-I and C-II.*

8.8 Comparison of the lifetimes to those in the drop tests

The number of cycles to failure in the vibration test was compared to those in the papers [06Mat2] and [06Mat3], where the same components and boards were used. The parameters of the widely-used Weibull distribution ([95Jen, page 65], [98Oco, page 74]) were determined for the vibrated 1BGA boards with the Weibull++-program, assuming that the failure-free time $\gamma = 0$. The values of the parameters are shown in Table V. The relative reliabilities of the interconnections are similar to those in the drop tests. The NiAu assemblies with no via-in-pads are almost equally reliable to the OSP assemblies with via-in-pads in both tests. In addition, the Kirkendall voids that were formed during the annealing reduced the number of cycles to failure by half or more. In both tests the scatter in the number of cycles to failure is large also. The characteristic lifetimes η of the vibtated 1BGA boards are nearly 10 times those determined for the drop-tested component boards in the papers. However, in Appendix C the average lifetimes of the vibrated 15BGA boards are more close to three times those of the drop-tested ones.

Table V *The determined Weibull parameters for the vibrated 1BGA component boards (4.2 V excitation).*

	OSP, via-in-pads	NiAu, no via	annealed
η	129	98	64
β	1.3	1.4	1.8

9 Finite element analyses

The simulations in this work are carried out by employing the submodelling method with three different levels of geometric details: the assembly level, the component level, and the interconnection level. The computed strains are compared to the measured values in order to verify the models, and the computed stresses are used to compare the vibration test with the drop test. In addition, FE analysis is used also to evaluate the sensitivity of the test methods.

9.1 FE models

Two assembly-level models were used: one of the drop test and one of the vibration test, but on the component and interconnection level the same model was used for both tests. The acceleration measured in the drop test (Fig. 35 on page 70) was applied to the lower ends of the standoffs in the assembly-level model to avoid problems related to calculating the shock impulse generated when the drop table hits the strike surface. In the vibration test the displacement of the centre of the sandwich plate was controlled.

9.1.1 Assembly-level models

The drop test model consisted of a quarter of the assembly and one standoff, while the vibration test model consisted of a quarter of both the assembly and the sandwich plate and one bolt; see Fig. 52. Symmetric boundary conditions were applied along the symmetry axes. The assumption of the symmetry was verified by simulations with full models. In addition, the whole board was included in the model when the natural modes were computed. The natural frequency analysis was done using a model with only the component board, not the supports.

The model of the PWB was made of linear quadrilateral shell elements (element type `s4r` [00Aba1]). The `s4r`-elements are linear, general purpose, quadrilateral shell elements that can be used for thin (Kirchhoff shell theory) and thick (Mindlin shell theory) structures, and for multilayer cross-sections. The elements in the PWB were 1 mm $\times$ 1 mm in size and 1.079 mm in thickness. Shell elements (2 mm x 2 mm) were also used in the components, and linear continuum elements (`c3d8`)

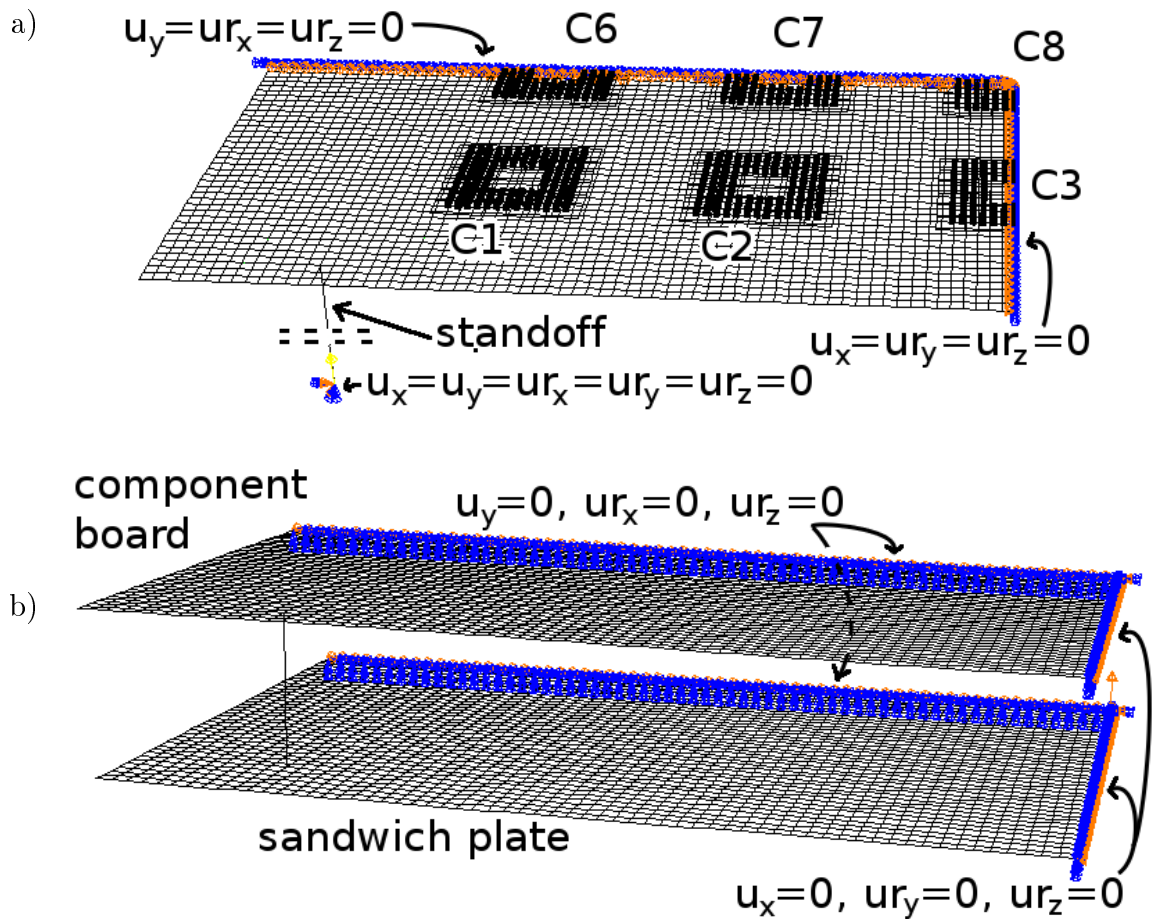

Figure 52 *FE models of a) the 15 BGA board in the drop test, and b) the board in the vibration test. Boundary conditions are also shown.*

were used in the solder interconnections. Linear beam elements (`b31`) were used in the standoffs. The `b31`-elements are formulated according to the Timoshenko beam theory: the planes normal to the beam's axis remain plane, and transverse shear strain is allowed. The diameter of the standoff was adjusted in order to fit the measurements to the simulations better. Because the screw hole in the PWB is 3.2 mm in diameter and the screw is only 3.0 mm, it is expected that some sliding will occur in the joints during testing, which explains the need for the reduction of the standoff diameter.

The model of the sandwich plate was made of shell elements also. The size of the elements were 6 mm × 6 mm, and the thickness was 4.55 mm. The bolts were modelled by using beam elements (`b31`) and point masses. The diameter of the bolts was 6 mm. The excitation was given by defining the acceleration of the nodes within a 20-mm distance from the centre of the plate.

The automatic time incrementation of Abaqus was utilised during the implicit calculations. Abaqus compares the equilibrium residual error (out-of-balance forces) at halfway through a time increment to the `haftol` parameter. If the error is too large or significantly smaller, it adjusts the length of the time increments. The `haftol` parameter was set to 23 in this work. In addition, the maximum step time was set to 0.1 ms, which limited the step size after the acceleration peak.

9.1.2 Screw joints

Defining boundary conditions is very important part of FE analysis. In the case of the component boards the boundary conditions describe how the boards are connected to the test fixtures. In the drop and vibration tests four screws were used to fasten the boards to the fixtures. The most simple way to model the screw joints between the board and the standoffs is *i)* to assume the joints as point connections, i.e. to use only one node in the board model for each connection, and *ii)* to assume that the connections are rigid, i.e. to set the displacements and the rotations of the nodes equal to those of the end points of the standoffs. However, applying loads or boundary conditions on single nodes overestimates the deformations near the nodes.

The connection between the standoffs and the board, i.e. the screw joints, was modelled as follows: the end node of the beam element in the standoff was connected to one node, the support node, in the PWB by using a connector element (`conn3d2`, type `join`) to make the displacements in the x, y, and z directions equal. The rotations of the support node were either set to zero or made equal to those of the endpoints of the standoff (additional option `align`). In addition, the shell elements of PWB within a 2.5-mm radius around the support node were enforced ($E = 1000$ GPa) in order to take into account the contact area of the screw head (diameter 5 mm).

In the model of the vibration test, reinforced elements were used also in the sandwich plate near the bolts. The reinforcement was similar to that in the model of the circuit board, and the reason for the reinforcement was the same. In the real structure, each bolt (diameter 6 mm) was attached to the sandwich plate by two nuts (diameter 12 mm).

9.1.3 Component-level model

The component-level model consisted of the component and a piece of PWB (13 mm × 13 mm × 1 mm). At locations C3, C6, and C7 only a half of the component was used and at location C8 only a quarter. The model was made of linear continuum elements (`c3d8`). The board was modelled using seven element layers (1 for both RCC layers and 5 for the FR4 layers), the interconnections were made of 3 × 3 × 3 rectangular elements, and the component was made of six layers (1 for the interposer, 2 for the chip, and 3 for the package above the chip). A quarter of the model was made of a single piece, which means that no multi-point constraints or `tie`-options were used in the quarter-model, but at the locations C1-C3, C6, and C7 two or four quarter-models were `tie`d together.

In the current case, the global model is made of shell elements, and the submodel is made of continuum elements. In Abaqus the boundary conditions of the submodel in such a case are determined from the displacements and rotations of the middle plane of the shell element. At the location C1 unrealistically large stresses were generated in the component-level model when the displacements of all nodes in the model edges were run by the global model. Therefore, an alternative method was tried: only the vertical displacements of the nodes in the middle plane of the component-level model within a 1-mm distance from the edges were run by the board-level model. The latter method is expected to include the effects of bending but to leave out membrane stresses. Symmetry boundary conditions were applied to symmetry planes at the locations C3, C6-C8 ($u_x = 0$ or $u_y = 0$). The model of a quarter of the component is shown in Fig. 53, together with the interconnection-level model.

9.1.4 Interconnection-level model

Stress distributions in the interconnections and the effects of the deformation rate and temperature were computed with the interconnection model. The model was made according to the geometric details shown in Fig. 23, except that the solder masks on the component and board side were not included; the masks are not in contact with the solder according to the cross-sectional pictures. Only continuum elements (`c3d8r`) were used, the sizes of which were approximately 20 μm × 20 μm

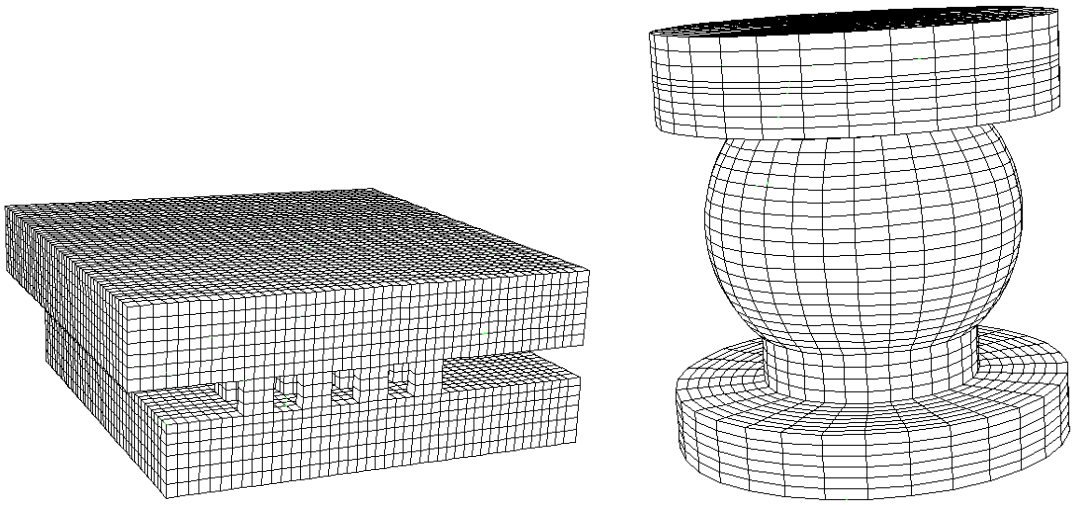

Figure 53 *Component and interconnection level models.*

$\times$ 20 μm. Despite the number of details and the round shape of the interconnection, the elements were not strongly distorted, except for the solder elements around the soldering pad on the PWB side. The model of the interconnection is shown in Fig. 53, together with the component-level model.

9.1.5 Materials

Under fast deformation solders become stronger because of strain-rate-hardening. In addition, the total solder volume in the component boards is small. Therefore, it is assumed that the plastic deformation of solders during the drop and vibration tests has negligible effect on the deformation history of the whole board. Hence, the plastic properties of solder are not included when the behaviour of the board is computed. However, the plastic properties have a strong influence on the stresses generated in interconnections; hence, they are included in the interconnection models when the stress distributions in the interconnections are computed.

The material properties used in this work are presented in Tables II (page 48), VI, and XI (page 108). The elastic property values of near-eutectic SnAgCu solders are expected be close to those of pure tin, because of the large amount of tin ($\sim$96 %). The value of the elastic modulus of tin at room temperature varies between 50 and 55 GPa according to publications [87Dra, 83Kam, 06Win]. The elastic modulus reduces by one fourth when the temperature rises to 120 °C [87Dra]. The value of the Poisson constant is about 0.35. In Table VI the values of the elastic modulus and

Table VI *Material parameters used in the FE models. The values in parentheses are from the providers of the materials.*

	LPI	Cu	Cu40	Cu70	RCC	FR4
E [GPa]	4	120	21.2	38.4	5.9 (3.5)	22 (18)
ν	0.3	0.3	0.35	0.37	0.4	0.25
ρ [kg/dm^3]	2.16	2.16	2.16	2.16	2.16	2.16

	solder	encapsulant	interposer	Si	steel	sandwich plate
E [GPa]	50.5	4	8	106.8	210	8.5
ν	0.36	0.3	0.3	0.42	0.3	0.3
ρ [kg/dm^3]	7.2	1.96	1.96	1.96	7.8	0.25

Poisson constant of the solder are calculated by multiplying the corresponding values of pure metals from [06Win] by their volume fraction in the eutectic composition. The values of LPI, encapsulant, and interposer are "good guesses", because reliable data was not available. The values for the sandwich plate are determined in this work by assuming an isotropic homogeneous cross-section for the plate and by fitting the computed values of the first natural frequency to the measured one.

Polymers have usually viscous properties; hence, it was assumed that the values of the elastic moduli given by the material providers are too small to be used during the rapid loading in the drop and vibration tests (see [95Tay], for example). Therefore, the values of the elastic modulus of RCC and FR4 were adjusted. The new values were obtained by fitting the calculated and measured values of the natural frequencies. The modified material parameters are presented in Table VI, together with the values given by the material providers. The component board is a multilayer printed wiring board, what makes determining the values difficult; hence, the adjusted values are probably not accurate either. However, when the adjusted values were used, the computed natural frequencies were close to the measured ones. Hence, the adjusted values should result also in more accurate simulations of the drop and vibration tests. For determining accurate values of elastic modulus, specimens made of one material and high-frequency loading should be used.

9.2 Natural frequencies and modes

The measured and computed natural frequencies are shown in Table VII. To take into account the effect of the accelerometer in the computations, a point mass of

Table VII *Computed natural frequencies [Hz] and their errors when compared to the measured ones.*

	15 BGA						0 BGA		
	measured		FEM		error		meas.	FEM	error
1.	223.5	(226.8)	213.9	(212.4)	-4 %	(-6 %)	(235.5)	(221.4)	(-6 %)
2.	409.3	(413.0)	405.3	(403.4)	-1 %	(-2 %)	(387.6)	(373.7)	(-4 %)
3.	568.6	(484.8)	526.4	(500.0)	-7 %	(+3 %)	(475.7)	(499.5)	(+5 %)
4.	615.8	(578.4)	599.7	(587.5)	-3 %	(+2 %)	(586.6)	(574.8)	(-2 %)
5.	810.3	(768.8)	772.9	(772.2)	-5 %	(+0 %)	(728.7)	(739.1)	(+1 %)
6.	891.3	(882.9)	926.9	(902.0)	+4 %	(+2 %)	(783.6)	(816.9)	(+4 %)
7.	974.8	(926.4)	937.1	(928.3)	-4 %	(+0 %)	(876.4)	(858.1)	(-2 %)
8.	1292		1243		-4 %		(1035)	(1053)	(+2 %)

2.7 g (accelerometer + cable) was included in the FE model at the location A. The errors in the computed values are small, but there is one strange difference in the influence of the accelerometer. According to the FE computation, the addition of the accelerometer reduces the first natural frequency (213.9 Hz $\rightarrow$ 212.4 Hz $\sim$ -0.7 %), but the measurements show an increase in the frequency (223.5 Hz $\rightarrow$ 226.8 Hz $\sim$ +1.5 %). Analytical solutions (38) and (54) on pages 24 and 29 support the FE solution: increasing the weight reduces the frequency. However, the differences are small and can rather easily be caused by small differences during the measurements. For example, a 2-% difference in the thickness of the board causes equally large difference in the frequencies according to (54). Small differences in the screw joint attachments may also cause small differences between the measurements.

The computed natural modes and the measured vibration of the ten locations are shown in Figs. 26 and 27 on pages 60 and 61. Here again, the computations and the measurements fit well together. However, the natural frequency analysis computes the eigenvalues and eigenvectors of (47), but it does not take into account the effect of the bending amplitude. Neither can it evaluate the amplitudes. Therefore, frequency analysis cannot be used to evaluate how much the tensile stresses generated by major bending affect the resonant frequency, but a dynamic analysis has to be made.

9.3 Measured and computed bending

During the drop and vibration tests, stresses in the interconnections are generated mainly by the bending of the boards. Therefore, it is necessary that the computed

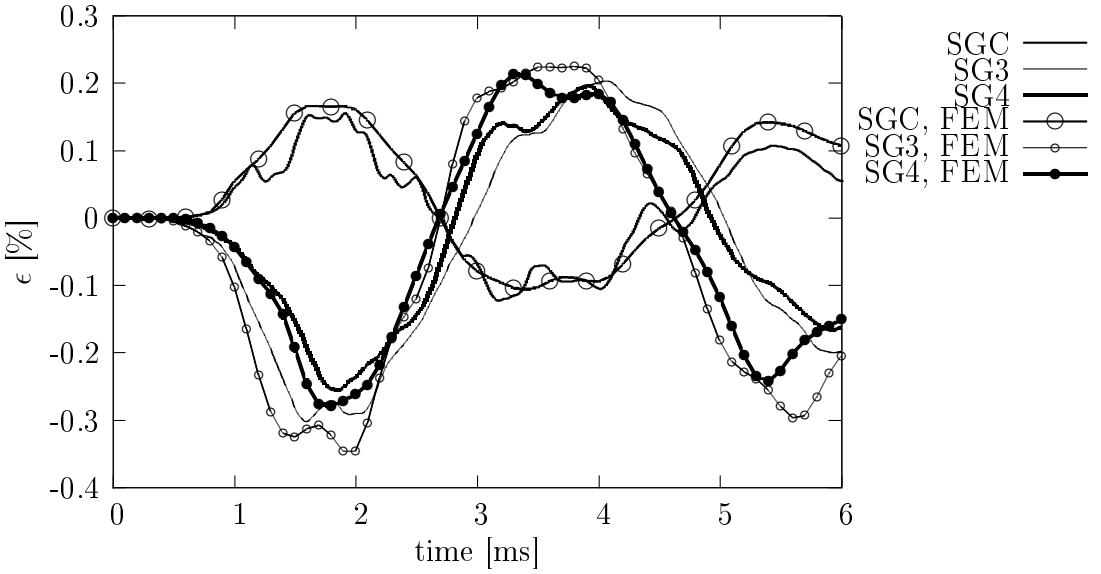

Figure 54 *Measured and computed strains of the 0BGA board at locations SG3, SG4 and SGC in the drop test.*

strains fit well to the measured ones when the stresses in the interconnections are being studied. The computed and measured strains during the first bending cycle at the locations SG3, SG4, and SGC of the 0BGA board during the drop tests are shown in Fig. 54, and those at SGA and SGC during the vibration test are plotted in Fig. 55. The values fit well: the computed amplitude and frequency of the primary vibration are close to the measured ones. Likewise, the amplitude and frequency of the secondary vibration are of the same magnitude as in the drop test. But the measured higher-frequency vibration in the vibration test is clearly stronger than the computed one. Measurements with the 15BGA board were carried out only during the drop tests, and they are shown in Fig. 56. The effect of the component on the strains at the board centre (SG4) is predicted well. The computed frequency is higher than the measured one in the case of the 15BGA board. This is probably due to the measurement cables: in the 15BGA board there were 6 strain gauges having thick cables, while in the 0BGA board only 3 gauges were used, and the cables were thinner.

9.3.1 Bending amplitude during the vibration tests

Fig. 57 plots the measured and computed displacement amplitudes during the frequency scanning. The height of the peaks and their locations are close to each other.

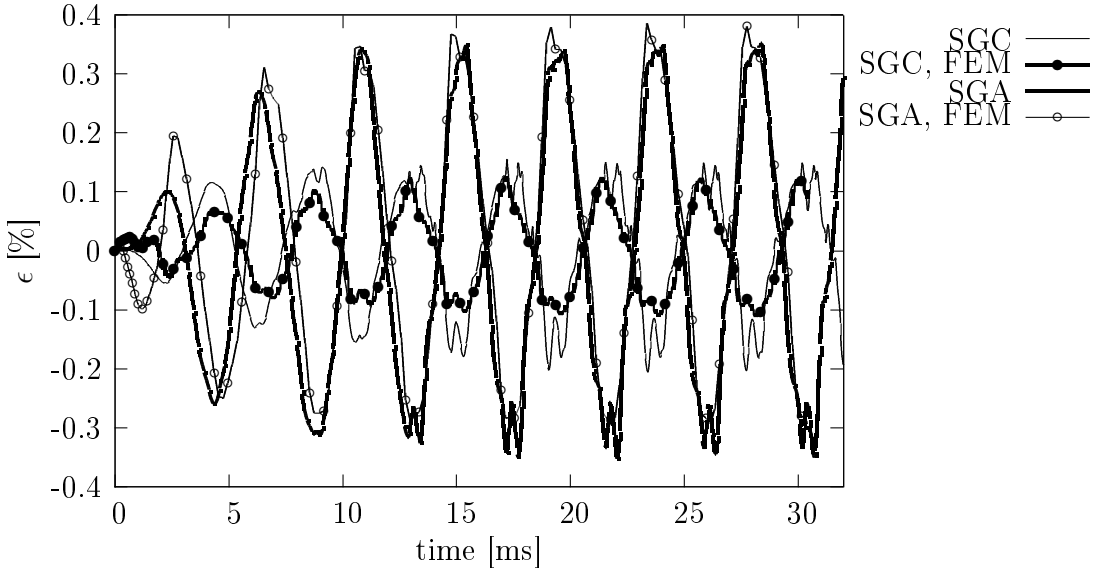

Figure 55 *Measured and computed strains of the 0BGA board at locations SGA and SGC in the vibration test (4.5 V).*

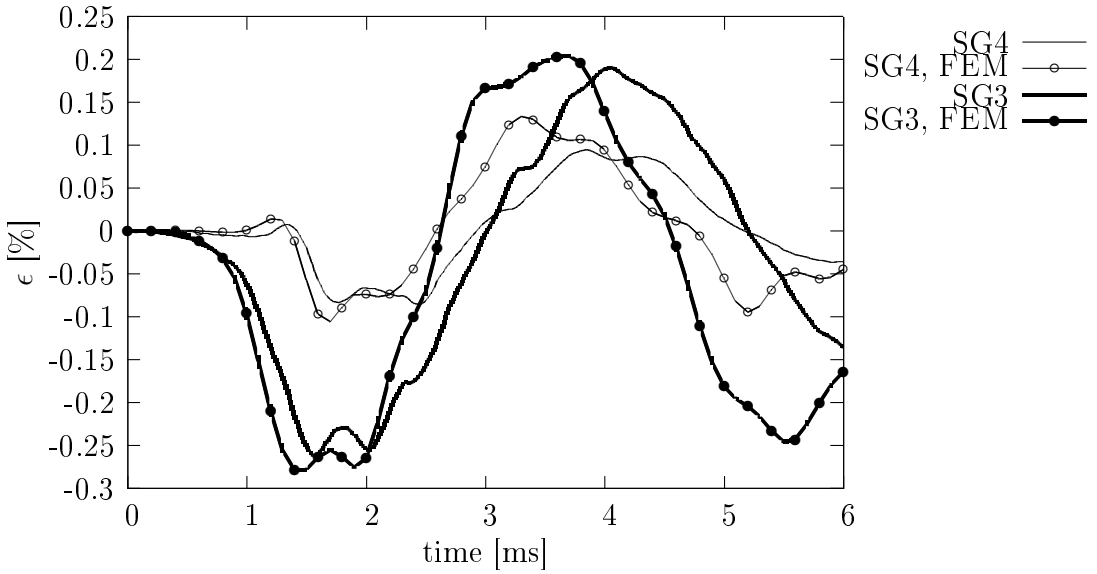

Figure 56 *Measured and computed strains of the 15BGA board at locations SG3 and SG4 in the drop test.*

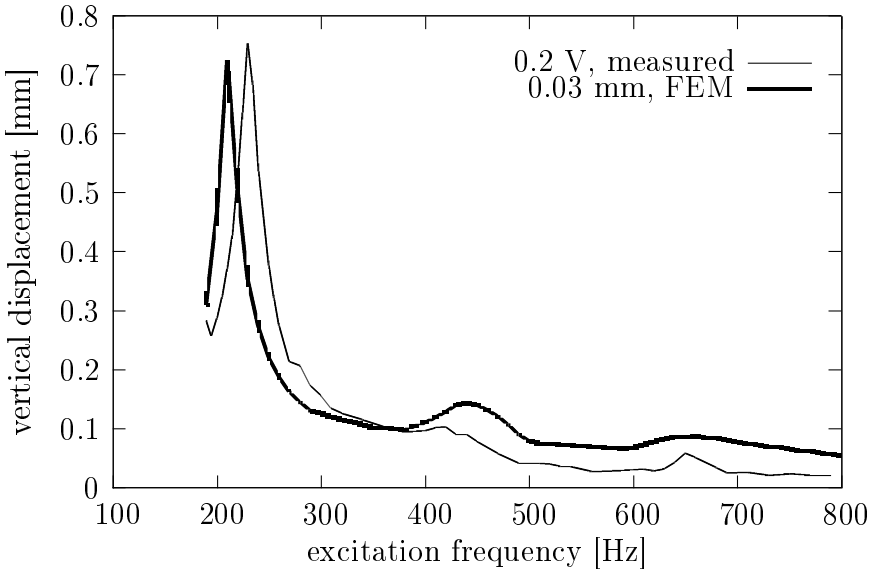

Figure 57 *Computed displacement amplitude at the centre of the 1BGA board as a function of the excitation frequency, together with the measured one. Excitation amplitudes 0.03 mm in the simulation and 0.2 V in the measurement.*

In the computations the displacement amplitude of the sandwich plate centre was set to a fixed value (0.03 mm), while in the measurements the loading force amplitude was fixed (0.2-V signal). This leads to a large relative difference at high frequencies, because the displacement amplitude of the attachment point of the sandwich plate depends on the frequency. If we assume that the vibration of the board does not have any effect on the vibration of the exciter head, then the excitation force

$$F = F_0 \sin \omega_F t = m_{eh} \ddot{x}_{eh} \tag{92a}$$

$$\Rightarrow x_{eh} = -F_0/(m_{eh}\omega_F^2) \sin \omega_F t \tag{92b}$$

where the subscript eh refers to the exciter head. Thus, when the excitation force is constant, as during the scanning, the displacement of the head diminishes as the frequency increases. In the FE analysis, however, the displacement of the exciter head was constant, resulting in an increasing excitation force.

Next, the response of the board with one component was computed. The frequency used in the experiments was 232.6 Hz, which is very close to the location of the first peak in Fig. 57. In the FE analysis the excitation frequency should be equally close to the first natural frequency of the FE model, which is about 6 % smaller than the measured one. Using the 232.6-Hz excitation in the simulation

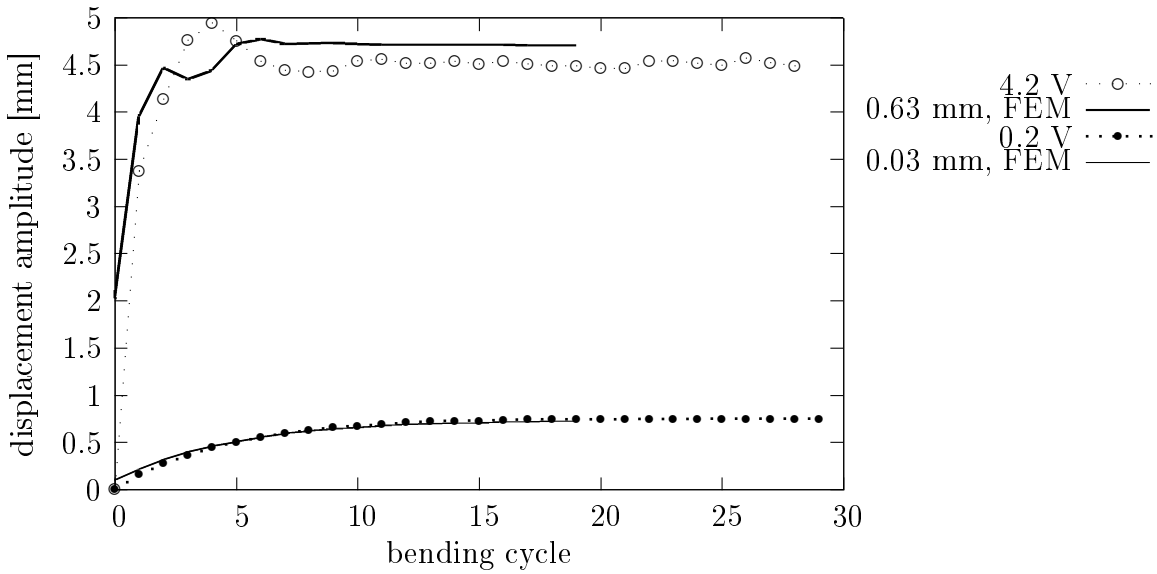

Figure 58 *Development of the displacement amplitude in the vibration test with two excitation amplitudes and in the simulations.*

is expected to cause considerable difference between the computed and measured vibration amplitudes. However, that does not change the excited bending mode because the 232.6-Hz frequency is within the first peak in both the measured and computed response. Hence, the difference in the frequency ratio ω_n/ω_F should affect the relation between the magnitudes of the excitation force and the bending amplitude only.

The computed displacement amplitudes of the board centre as a function of the period and the excitation amplitude are shown in Fig. 58, together with the measured ones. The frequency during the excitations was 232.6 Hz. In both cases, the smaller the excitation amplitude, the more time it takes for the displacement amplitude to increase to its maximum value.

9.4 Sensitivity of the model

In order to evaluate how sensitive the test system, the measurements, and the FE models are, a few changes were made in the models, and the results are presented below. First, it was verified that the plastic deformation of solder joints does not have a significant effect on the computed bending of the board: changes in strains at SG3 and SG4 were less than 5 % of the maximum strain, and the strain curve shape was the same, when the plastic properties of solder given in Table XI were taken

into account. The effect was similar to what it would be, if the damping coefficients were further modified.

9.4.1 Geometrical nonlinearity

FE analysis can take into account, how large bending changes the response of the board. In practise, this requires the stiffness matrix K in (45) to be updated during every step, and, by default, this is not done in the implicit method because of the large amount of computation needed. In Fig. 59 the computed strains of SG4 are plotted in the cases of the drop test and the 230-Hz vibration test. In the vibration test the need to use the option is emphasised when the loading frequency is close to the natural frequency of the board.

9.4.2 Supports

The effect of screw joint models on the computed first natural frequency were investigated in the case of the board without components. The results are presented in Table VIII, and the support types in Fig. 60. First, the effect of the support area was evaluated by using one or a few nodes to prevent vertical displacements. The screw model type a is the one used in the drop and vibration test analyses and in Table VII. All displacements and rotations of the support nodes (the centres of the screw holes) in the model a were prevented, and the elements within the 2.5-mm radius from the support nodes were reinforced. In the cases b - d no reinforced elements were used, but in c and d the vertical displacement was prevented at the nodes within the distance of 1.5 mm and 2.5 mm, respectively, of the support nodes. When the frequencies were measured, the boards were fastened with the screws to the ϕ-6-mm standoffs.

Table VIII *Computed first natural frequencies of the board with different boundary conditions.*

support type	a	b	c	d	e	f	g	h
first freq. [Hz]	221.4	162.8	209.3	222.3	116.3	235.5	204.2	221.0

When the reinforcement is used (type a), the values are close to the cases where the vertical displacements of the additional nodes are prevented (types c and d), but

a)

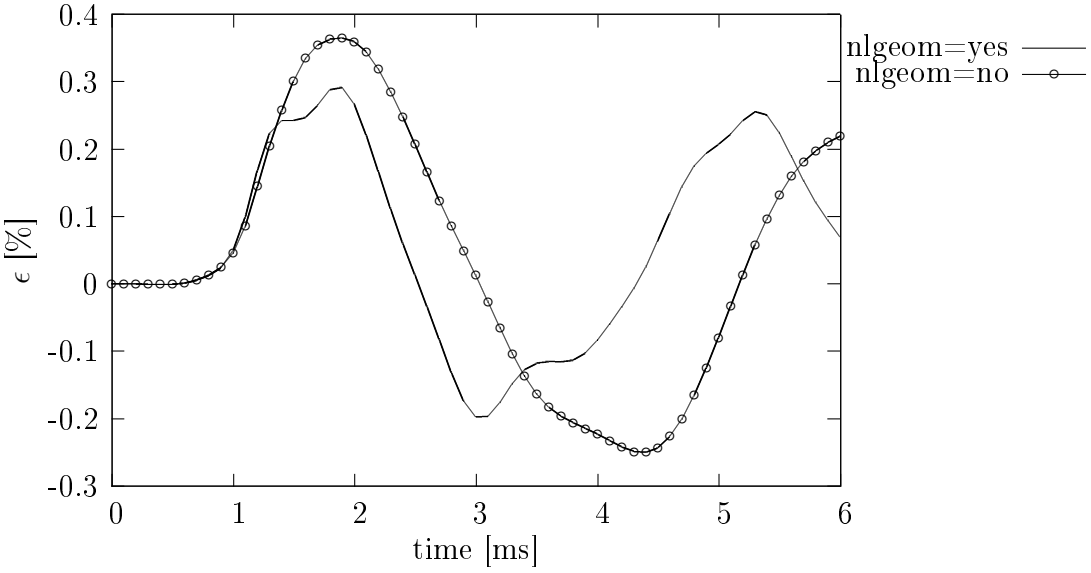

b)

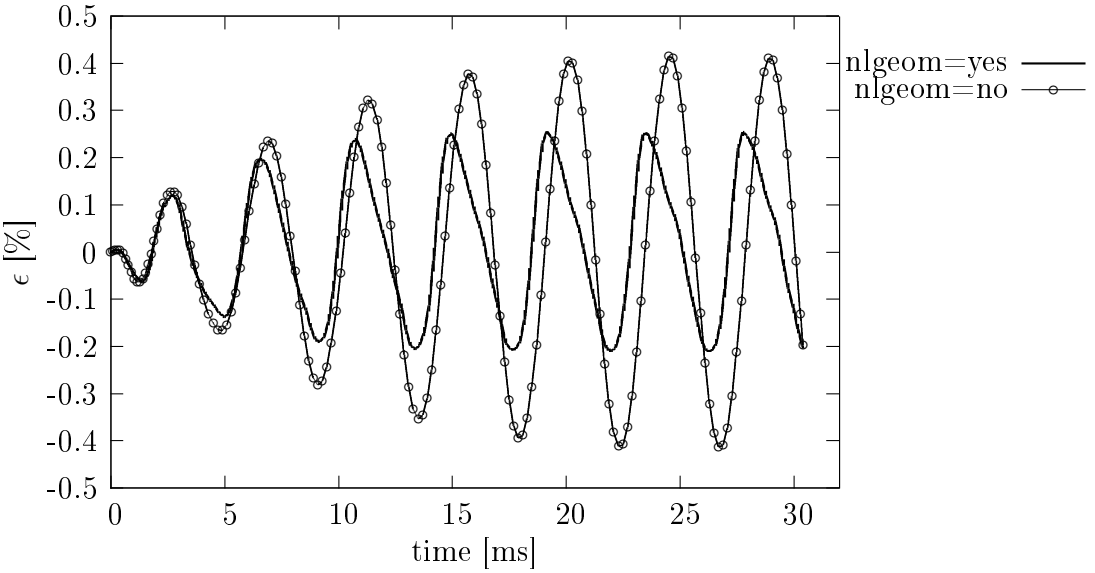

Figure 59 *Strains in the 0BGA board at the location SG4 when geometrical nonlinearity is or is not taken into account a) in the drop test and b) in the vibration test.*

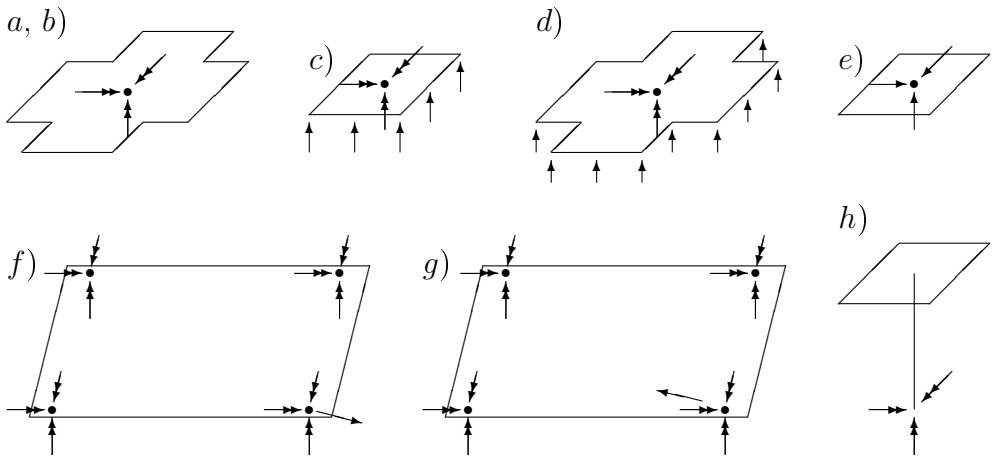

Figure 60 *Boundary conditions of the support types a - h. An arrow ← means fixed displacement in the direction of the arrow and a double arrow ↠ means fixed displacement and rotation. In the cases a-e, and h the boundary conditions of all four support nodes are identical, and only one support node is shown here.*

the difference is large when compared to the single-node support (type *b*). Applying the boundary conditions on only a single node causes high stress concentration around the node, which results in errors in the simulations unless the reinforcement is used. In addition to the changes in the frequencies, the reinforcement also affected the order of the modes: the frequency of the mode 6 (Fig. 27, page 61) was reduced to 886 Hz, while the frequency of the mode 7 (Fig. 27) was reduced to 809 Hz when no reinforcement was used (type *b*).

According to analytical solutions for rectangular plates that are rigidly supported at their edges, the first natural frequency should diminish by one half if the rotations at the edges are set free. Here free support (*e*) reduces the first frequency by one half only if reinforcement is used, or support is distributed over a few nodes.

The effect of tension on the natural frequencies was studied by applying a small displacement to one support node. When tension was generated in the board model by displacing one support node by 0.01 mm (0.01 %) in the x direction and 0.007 mm (0.01 %) in the y direction (support type f), the first natural mode increased to 235.5 Hz. When the direction of the displacement was reversed (support type g), the frequency diminished to 204.2 Hz; thus, even small tension should increase the

frequency in bending. Adding the standoffs of the drop test table had only a minor influence (h).

The effect of the thickness of the standoffs on the simulations of the drop test was evaluated. The results of the evaluation apply only to the FE model because of the difference in the behaviour of the screw joints; in the FE model the screw joints are rigid, which is not the case in the real applications. However, the trend should be similar: if a reduction in the thickness increases the bending amplitude, it should also increase in a real application, but the amount may be smaller.

Fig. 61 shows the measured and computed strains at location SG4 on both sides of the 0BGA board. When no sliding at screw joints is allowed, and thick supports are used, high membrane stresses (stresses in the middle plane of the shell) are generated in the board, which leads to large differences between the strain amplitudes on opposite sides of the boards. Support thickness also affects the vibration frequency: the thicker the supports, the higher the frequency; this results from the membrane stresses generated in the board (see (55)). The thickness of the standoffs has an effect on the rotation of the standoff end also. When the thickness is reduced in order to model horizontal sliding, the rotations of the support node are increased simultaneously. However, the sliding in the real screw joints should not increase the rotations. The effect was evaluated by fixing the rotations of the support node to zero, but the effect was insignificant.

Similar analysis was carried out to evaluate how the rigidity of the sandwich plate influences the behaviour of the board during the vibration test. In the simulations the thickness of the plate was multiplied by 0.5 and 2.0. The results are plotted in Fig. 62. When the thickness changes, the mass of the plate also changes. This has a small effect on the values, in addition to the effect of the change in the stiffness of the plate.

9.4.3 Elastic modulus and board thickness

The analytical solution (54) on page 29 predicts how changes in the thickness and elastic modulus of boards affect the vibration frequencies. In Fig. 63 the computed strains at location SG4 in the drop test are plotted in the case of no components. In Fig. 64 the computed strains at the same location are plotted during the vibration

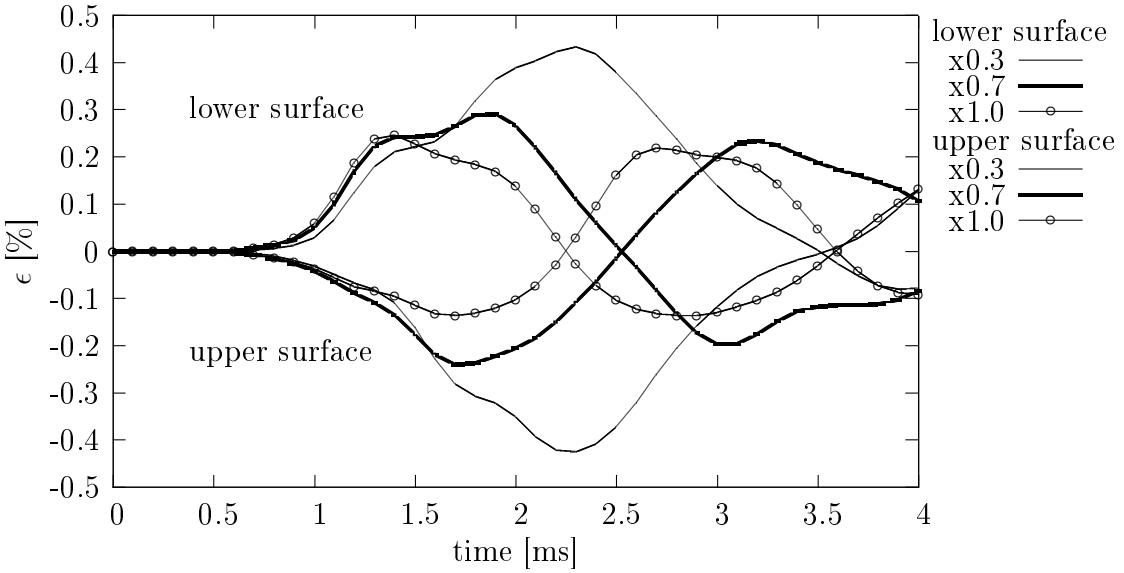

Figure 61 *Computed strains at SG4 on the upper and lower surfaces in the drop test with different standoff thicknesses.*

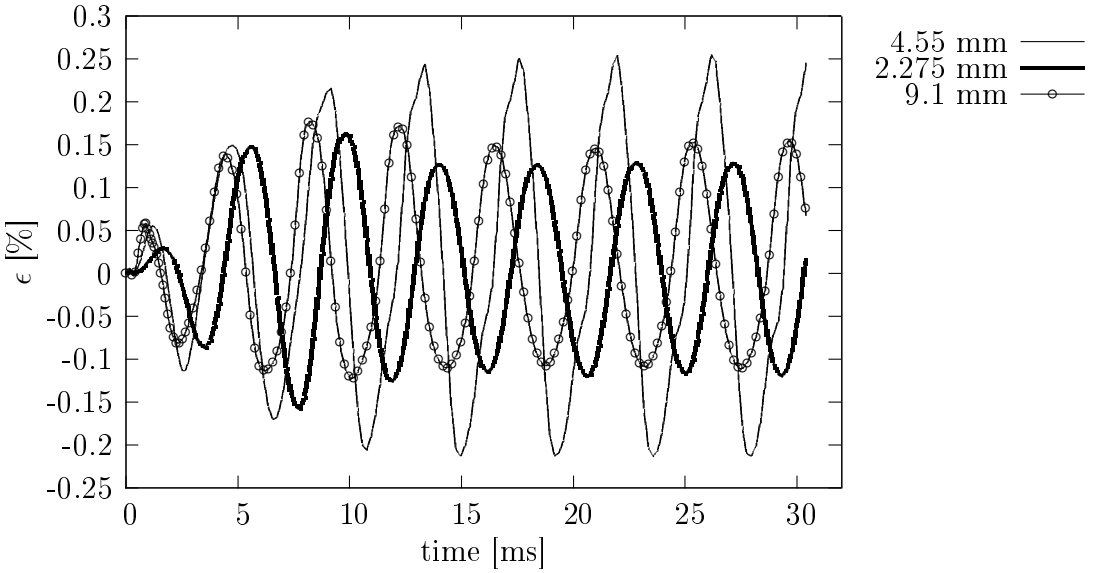

Figure 62 *Computed strains at SG4 in the vibration test when the thickness of the sandwich plate is changed, f = 230 Hz.*

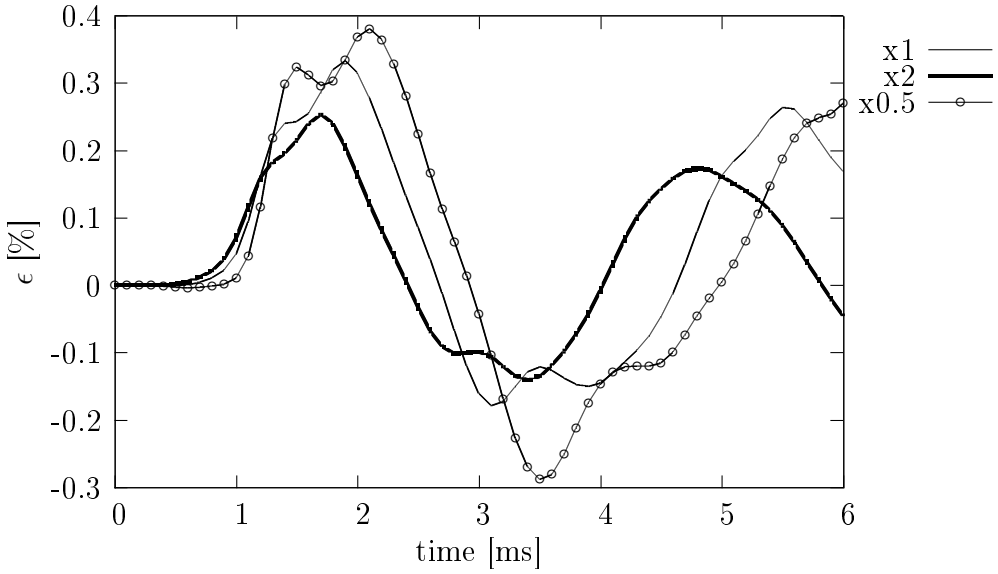

Figure 63 *Computed strains at SG4 in the drop test when the elastic moduli of the board materials are varied.*

test at 230 Hz.

Changes in the elastic modulus values of component boards affect the bending during the tests differently. In drop tests reducing the elastic modulus increases strains and *vice versa*, but in vibration tests strains lessen regardless of whether the elastic modulus is increased or reduced. Changing the elastic modulus or thickness of the board changes the resonance frequency, thereby reducing the vibration amplitude. According to (54), the resonance frequency is increased by 41 % when the elastic modulus is doubled, and the frequency is reduced by 29 %, if the modulus is halved.

Table IX shows the computed maximum bending amplitudes of a board with 15 BGAs in the drop and vibration tests. When the board thickness was increased from 1 mm to 2 mm, the bending amplitude in the drop test diminished by 40 % while in the vibration test the reduction was 63 %. In the vibration test the reduction is larger because the natural frequency of the board changes linearly with the thickness as shown in (54) (page 29). If the excitation frequency is not modified, the amplitude diminishes further as shown in Fig. 8 (page 26).

From the simulations presented above, it can be concluded that the vibration test is more sensitive to changes in the test board than the drop test. This is because the bending amplitude in the vibration test depends significantly on how

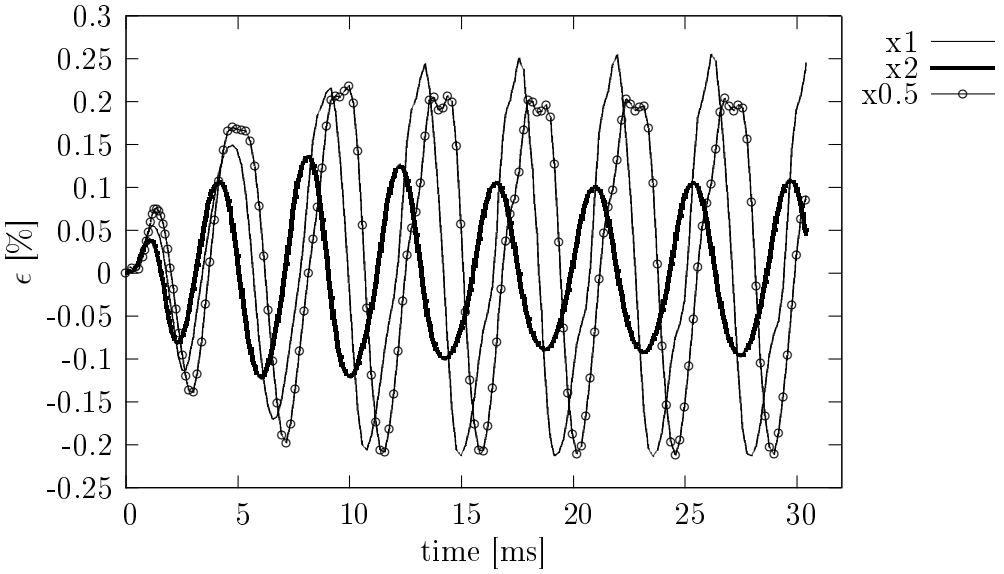

Figure 64 *Computed strains at SG4 in the vibration test when the elastic moduli of the board materials are varied, f = 230 Hz.*

Table IX *Computed bending amplitudes of the 0BGA boards having two different thicknesses in the drop and vibration tests (f = 230 Hz).*

	h_1 = 1 mm	h_2 = 2 mm	amp_2/amp_1
drop test [mm]	4.65	2.78	0.6
vibration test [mm]	4.25	1.58	0.37

close the frequency of the excitation is to the first natural frequency of the test assembly. And, most of the changes in the test board affect its natural frequencies. In the drop test, on the contrary, the loading is a single pulse, and the duration of the pulse is significantly shorter than that of the first natural mode of the test board. Hence, instead of describing the loading signal, the response of the board (the measured strain amplitude) should be used to describe the loading in the vibration test.

9.5 Stress analysis of the interconnections in the drop and vibration tests

In the previous sections the accuracy of the FE model and the parameters affecting the computation results have been investigated. Here, the stress states of the interconnections during the drop and vibration tests are studied by employing FEA.

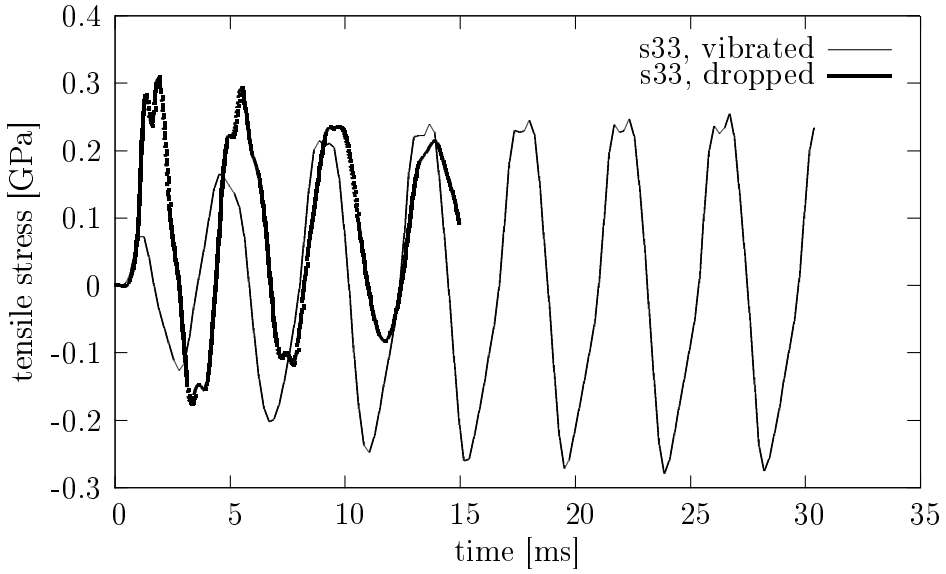

Figure 65 *Calculated vertical tensile stress in the corner interconnection of the central component C8 in a vibrated (0-30 ms) and a drop tested (0-16 ms) component board.*

9.5.1 Differences in the stress histories between the tests

In both the drop test and the vibration test, stresses in interconnections are generated by the bending of boards. Shock loading in drop tests excites a larger number of bending modes than harmonic loading does in vibration tests. Fig. 65 presents the computed vertical tensile stress histories in the corner interconnection of the centre component C8 in the component-level model during the drop and vibration tests. In the case of the drop test the first 16 ms and in the vibration test the first 30 ms were included in the computations.

There are quicker changes in the stress value during drop testing, and the amplitude diminishes rather quickly to zero. During the vibration testing the stress is rather smooth, and after the first few cycles, the stress amplitude remains constant.

9.5.2 Effects of the inertia forces

The components mounted on the boards were lightweight (0.3 g). Hence, on the basis of the applied acceleration (1500 g_n) and the total interconnection area in one component (144 bumps $\times(0.19\text{ mm})^2 \times \pi = 16.3\text{ mm}^2$), the average inertial stress in each interconnection is $\sigma = F/A = ma/A = 0.3 \cdot 10^{-3}\,\text{kg} \cdot 1500 \cdot 9.81\,\text{m/s}^2/16\,\text{mm}^2 =$ 0.28 MPa, which is very small when compared to the stresses generated by bending.

Thus, it is expected that the stresses in interconnections can be accurately computed by making a static analysis with the component level model using the boundary conditions computed during the dynamic analysis of the board level. Because there are a large number of elements in the component level model, this method would reduce the amount of computing time significantly. To verify the assumption, the stresses in the corner interconnection of the central component C8 were computed by the static and dynamic analysis of the component level. The maximum values of the vertical tensile stress at five different moments of times are given in Table X. The computed values correspond to each other reasonably well. Hence, the static method is employed on the component and interconnection level. Similar conclusions were made by Jih and Jung [98Jih] and Che and Pang [04Che].

Table X *Computed maximum vertical tensile stresses [MPa] in the corner interconnection of the central component C8 by using the dynamic and static methods.*

	time [ms]				
	1.0	1.25	1.5	1.75	2.0
dyn	76	252	248	270	292
stat	78	238	209	265	248

9.5.3 Effects of the component locations

According to the lifetime prediction model (28) (page 22), the larger the vertical stress, the earlier the failure. Hence, the distribution of the vertical stress was evaluated first (Fig. 66), and the correspondence between the test results and the calculated stresses was investigated. The effect of the location on the measured lifetimes in drop tests and vibration tests is presented in Fig. 51 on page 86.

There are similarities and differences between the calculated stress distributions and the measured lifetimes. The order of the three components to fail last is the same according to the tests and the lifetime prediction model (28). But the order of the components to fail first is different. According to the measurements, the order of the first three to fail is C3, C8, and C2, but the order is C2, C3, and C8 according to the simulation (Fig. 66). When the von Mises, Tresca, and principal stresses are compared instead of the maximum vertical stresses, the same order is obtained. However, in the case of the von Mises and Tresca stresses, the difference

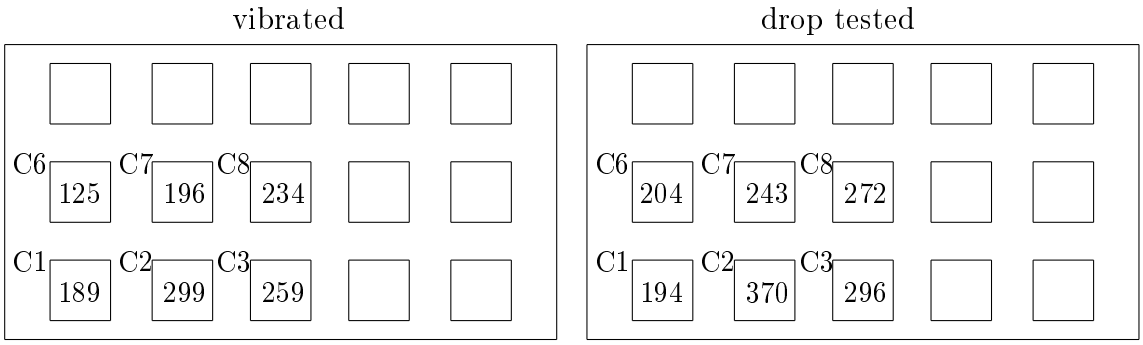

Figure 66 *Calculated maximum vertical tensile stresses (σ_z) in solder interconnections during drop and vibration tests.*

between the values of the stresses in the locations C2, C3, and C8 is smaller. The calculated maximum von Mises stress at the location C2 is only 10 % higher than at C3, while the difference is 25 % in the case of the vertical stress. Similar calculation results were obtained by Syed *et al.* [05Sye] for drop tested component boards, but they reported that during the tests the component C2 failed also first, although the difference between the lifetimes of C2 and C3 was very small.

Another interesting difference between the component locations is the distribution of the stresses between the interconnections of the components. At the location C8 all the corner interconnections are under the same stress state due to the symmetry. At the location C3 in the corners closest to the board edges, the stresses are about 20 % higher than in the other corner interconnections. At C2 the difference is significantly higher. The most highly stressed interconnections at C2 are the corner interconnection closest to the screw support and the centre. In those the computed stress is three to four times that in the two other corners. The high concentration of the computed stresses in the two corner interconnections of components C2 may explain the contradiction between the measured lifetimes and the computed stresses in components C2, C3, and C8. Unfortunately the other authors have not studied the effect of the component location on the computed stresses in detail.

The computed stress distributions in the two tests are similar, which supports the idea of using the vibration test as an alternative method to the drop test. The similar stress distributions also indicate that the first natural bending mode is the primary source of the stresses.

Table XI *Yield stress-plastic strain pairs used in FE analysis.*

plastic strain [%]	0	0.6	2	4	8	22
yield stress [MPa]	12	34	70	90	100	106

9.5.4 Effects of plastic deformation

All the simulations above were performed on the basis of the assumption that either there is negligible plastic deformation in solder joints, or that the material damping coefficients used in the computations include the influence of plastic deformation. When stress distributions in solder interconnections are computed, plastic deformation has a significant influence at the interconnection level. But should the plastic properties of solders be also included in the board level? The strains and stresses in the corner interconnections of the centre component were computed with the component-level model by using boundary conditions from two board-level computations; in one the solder was expected to be fully elastic and in the other the plastic properties given in Table XI were included. The differences in the distributions and maximum values were small. The maximum principal strain was 2.19 % and the maximum principal stress was 135.5 MPa when the plastic properties were included in the board level, and when they were not included, the values were 2.02 % and 135.0 MPa. Thus, the effect is rather small. However, on the component and interconnection levels the plastic properties should be taken into account.

9.5.5 Effects of strain rate

The effects of the strain rate on the stresses that interconnections experience were studied with the help of FEM in the case of the drop test. The displacements on the boundaries of the interconnection model were those computed using the 15-BGA board-level model and the component-level model of C8. Hence, only the mechanical properties of the solder and the time for the deformation are different between the computations in Fig. 67a-d.

The distribution of the calculated vertical tensile stress in the case where only elastic behaviour was included in the calculation is shown in Fig. 67a. The distributions in Figs. 67b and 67d were calculated by including the creep model (13), in addition to the elastic properties, to describe the behaviour of the solder. The

parameters determined for Sn3.4Ag0.8Cu were used (Table II, page 48). The deformation time was 1 ms in Fig. 67b and 30 min in Fig. 67d. In Fig. 67c the plastic properties given in Table XI were used instead of the creep properties.

In thermal cycling the creep model is expected to describe the behaviour of the solder well, because the number of cycles to failure is large, and solder is expected to strengthen during first loading cycles. But at high strain rates in the drop and vibration tests, it overestimates the stresses required for small plastic strains because it describes only the secondary stage of creep, not the primary one. In drop tests interconnections may fail after a couple of drops, and it is probable that solder does not reach its full strength. Hence, the distribution in Fig. 67b is an upper limit of the stresses in the interconnection in the drop test. Anand's model (14) is not included in the code of Abaqus; therefore, the evolution of the yield strength as a function of strain and strain rate has to be included by using other methods, or by using user subroutines. Here, Anand's model was used to predict the evolution of the yield strength at the strain rate of 1000 %/s, and from the calculation the stress-plastic strain pairs in Table XI were obtained. The distribution in Fig. 67c was computed when the plastic deformation was included by this method. Because of the strain-hardening during repeated drops, the stresses are expected to be in the range between the lower (Fig. 67c) and upper limit stresses (Fig. 67b) - if the models are otherwise accurate enough.

In Figs. 67a - c the deformation time was 1 ms, as it is during drop tests – although, time has no effect on Figs. 67a and c. If the strain rate is reduced, there is more time for plastic deformation, which reduces stresses. For example, in thermal shock tests the deformation time is approximately one minute or longer. To demonstrate the effect of the strain rate, the stresses were calculated when the deformation time was 30 minutes, and the result is plotted in Fig. 67d. The maximum vertical stress reduced to one third because of the increase in the deformation time.

The distributions in Fig. 67 are for the vertical tensile stress, which is the stress component that is perpendicular to the reaction layers and, hence, perpendicular to the propagation paths of most of the observed cracks. Other interesting stresses are the von Mises stress (the stress used in the models of plastic deformation), the Tresca stress (the maximum shear stress), the maximum principal stress (the maximum

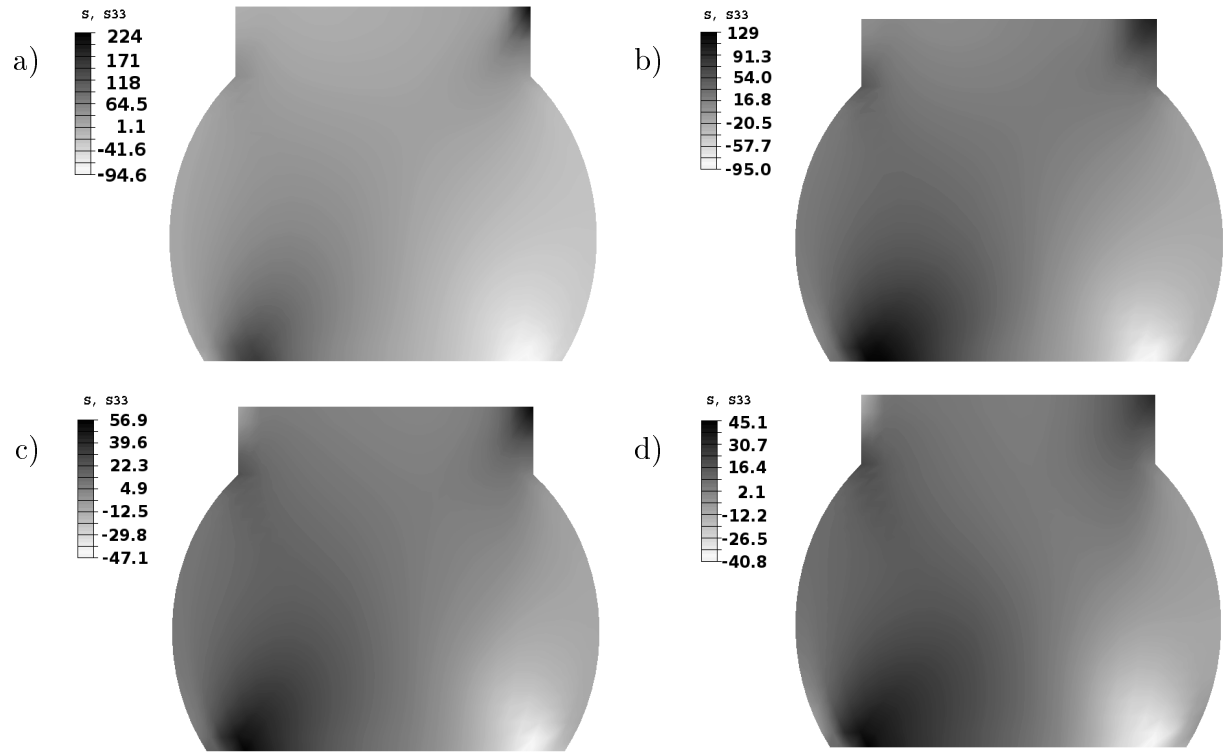

Figure 67 *Calculated vertical tensile stress distributions in the cross-sections of solder interconnections: a) elastic solder, b) creep included, c) plastic behaviour as in Table XI, d) creep included, deformation time 29 min.*

tensile stress). The distributions of these stresses are similar to those of the vertical tensile stress. In the case of elastic solder, the maximum values of each distribution were: *i*) Tresca 327 MPa, *ii*) the maximum principal stress 393 MPa, and *iii*) von Mises 292 MPa; and in the case of the plastic solder: *i*) Tresca 67.7 MPa, *ii*) the maximum principal stress 85.8 MPa, and *iii*) von Mises 58.7 MPa. The von Mises and Tresca stresses describe, depending on the yield criteria, if plastic deformation occurs, and hence, are related also to thermal cycling (low cycle fatigue), whereas the maximum principal stress and the vertical stress component are expected to have strongest effect on the fast propagation of cracks during the vibration and drop tests.

The strains during the tests have similar distributions to the stresses. The maximum principal strain was 1.1 % when the stress-strain pairs given in Table XI were used. The duration of one bending cycle is from 4 to 5 ms, see Fig. 40, and it takes a quarter of a cycle ($\approx$1 ms) for the strains to reach their maximum values. Hence, according to the FE analysis the strain rate in the interconnection can reach values

up to 1000 %/s. The change in the distance between two nodes, one of which was on the PWB side of the interconnection in the centre of the solder-pad interface, and the other was on the component side, was 0.31 %. Thus, the average strain rate is approximately 300 %/s, whereas in the calculation with the long deformation time, the strain rate was approximately $3 \cdot 10^{-4}$ %/s.

10 Discussions

The JEDEC drop test has been widely used during recent years, and some limitations have been noticed; therefore, methods for improving the test have been investigated. In the drop test the test assembly falls about one meter, before it hits a heavy block of stone generating a strong impact on both the test assembly and the testing apparatus. The impact causes the measurement cables to fail occasionally resulting in false signals and significantly prolonged testing times. The standoffs between the test board and the drop table need to be replaced also rather often because of the fatigue loading. The bearings wear out, and the drop height has to be adjusted rather often in order to produce the required acceleration pulse. Testing at elevated ambient temperatures, which is important because of the heat-generating high-density components and the temperature dependent properties of solders, is not possible due to the effect of the temperature on *a)* the properties of the strike surface and *b)* the friction between the guiding poles and the drop table. Moreover, measuring the bending of the component board is, in practise, limited to strain gauges, because of the long distance the board travels during the test. In addition, the impact load excites several natural modes; therefore, the bending of the component board is complex during the test.

The vibration test provides another method for generating a very rapid, high-amplitude loading that is similar to that generated by accidental drops. Many of the problems related to the drop test can be avoided with the vibration test because the test structure does not move significantly. In addition, the loading conditions can be modified in the vibration test more easily. In the vibration test two considerable problems were noticed: Firstly, the shaker was able to vibrate the test boards strongly enough only when the weight of the fixture was very small. Secondly, the data processing has to be very fast. Reading enough data points in a period from 15 channels and tracking if four failures has occurred during six successive periods ([03Jed]) is not trivial, even though the vibration frequency is only 230 Hz. Hence, increasing the vibration amplitude and frequency may be difficult.

In the previous chapters the bending of the test boards were measured during the JEDEC drop test and the vibration test, and the generated failure modes were

compared. When the strain amplitudes of the boards were of the same level, the same failure modes were produced. According to Tee *et al.* [03Tee] and the short review of the lifetime estimation models in Chapter 3.4, stresses have a major effect on the lifetime of solder interconnections under shock loading conditions. In the two tests, the stresses in the interconnections are generated when the board bends, and the interconnections between the components and the board are deformed.

The stresses in interconnections cannot be measured explicitly, but finite element analysis is needed. To verify the results of the FE analyses, it is desirable that the computed strains and displacements are compared to the measured ones. The less complex the bending and the more feasible the measurement, the easier the comparison and the more accurately the lifetime parameters can be determined. Therefore, carrying out reliability tests with a vibration system is expected to result in a more accurate relationship between the stresses in the interconnection and the measured times-to-failure. According to the FE analyses, the maximum stresses in the interconnections during the two tests are very similar. Hence, FE analysis does support the idea that the vibration test method can be employed to study the reliability of solder interconnections under shock loading conditions.

The vibration test makes use of the resonance. The component boards are vibrated at the first natural frequency of the component board. At resonance a large bending amplitude and, thereby, large stresses in the interconnections are generated with a low force. In contrary, in the drop test a large amplitude loading is needed for generating bending with the same amplitude. The first natural mode dominates the bending of the component board in the vibration test as well as in the drop test. Hence, it is not surprising that the failure modes in both tests are the same when the bending amplitudes are similar. Making use of the resonance has also a drawback: the vibration test is more sensitive to changes in the properties of test boards than the drop test. Changes in the mass, thickness, and elastic modulus of test boards changes their natural frequencies. Hence, when the vibration test is used, one should specify the strain amplitude used in a test, and tune the excitation voltage and frequency on the basis of the measured strains. Specifying the excitation but not the board response in the vibration test leads to larger differences between different test sets than that does in the drop test.

The evolution of the bending amplitudes is different between the tests. In the vibration test the amplitude increases during the first few periods, after which the amplitude remains constant for as long as the excitation continues. Thus, the loading amplitude is practically constant, and the time between the peaks is about two milliseconds (depending on the resonance frequency). In the drop test, on the contrary, the loading is a series of short impacts that cause rapidly attenuating vibrations. Thus, the loading amplitude of the interconnections is not constant. The time between two maxima is about 8 seconds (depending on the drop tester), and the time between two local decreasing maxima is about two milliseconds (depending on the resonance frequency). On the other hand, the vibration test system can be used to generate only a few excitation periods. The amplitude would increase to its maximum during the few periods, and, when the excitation stops, the vibration would attenuate. As the result, the bending in the vibration test would be very close to that in the drop test, see Fig. 68. In Fig. 68 the period of the constant-amplitude vibration has been edited away. In this case, the bending is very similar after the initiation of the vibration. The author suspects that the stress peaks before the maximum peak has similar influence on the nucleation and propagation of cracks as the attenuating peaks after the maximum. Hence, the only difference between this kind of periodical vibration test and the drop test would be the number of active vibration modes. However, keeping the stress amplitude constant during the test is expected to be more useful, because it makes analysing the test easier. On the other hand, the recovery may have influence in drop tests, and generating short pulses with the vibration tester may therefore be justified.

Figure 68 *Strains in the vibration test when the excitation is stopped after a few cycles, and those in the drop test.*

10.1 Comparison of the tests

Here, the observed pros and cons of the vibration test, when compared to the drop test, are collected in a list. The tests are compared also in numerical format in Table XII.

Figure 69 *Schematic figure of a thermal chamber and a vibration test system with a test board.*

- *The vibration test system is more versatile than the drop test system.* Because the test structure does not move much, accurate laser measurements, which do not affect the bending, can be carried out. In addition, the effects of ambient temperature on the time-to-failure can be studied in thermal chambers; see Fig. 69, Zhao *et al.* [00Zha], Weiss Umwelttechnik GmbH [06Wei]. Moreover, in the drop test one can control only the amplitude of the vibration, while the magnitude and frequency of the loading can be easily varied in the vibration test system. Hence, in the drop test the vibration is always a sum of several modes, the first mode having the largest influence. In the vibration test other modes can also be excited. However, the first mode requires the smallest force.

- *The vibration test system needs less maintaining.* The vibration of the test board at the resonance does not load the tester to the same extent as the strong impact in the drop test. Therefore, the fixture and the measurement cables are loaded significantly less. In the drop tester cables fail occasionally, while none were broken during the vibration tests carried out for this thesis. In addition, the standoffs in the drop tester need to be replaced more often than in the shaker. In addition, the mounting table is attached to the shaker body by springs, not bearings; hence, friction is insignificant in the vibration test system. The bearings in the drop tester need to be replaced occasionally, and the drop height needs to be adjusted rather often to generate the required shock impulse.

- *The vibration test is faster.* Carrying out 200 drops with a drop tester may take more than one hour if cables fail during the test. The 200 drops themselves take about half an hour. If we assume that three to five cycles in the vibration test correspond to one drop in the drop test, the corresponding test takes up to 5 seconds (1000 cycles, 200 Hz) in the vibration test. The very short

time interval between the bending maxima in the vibration test may prevent microstructural changes in interconnections, but similar acceleration is taking place also in the drop test – although not to the same extent.

- *The behaviour of the test board is less complex in the vibration test than in the drop test* because in the vibration test only one natural vibration mode is excited. In addition, changes in the drop height can affect other properties of the acceleration than just the amplitude, see Chapter 7.4.2. Hence, understanding the causes and effects is more simple in the vibration test. However, increasing the amplitude may also excite higher natural modes in the vibration test system (Chapter 7.3.5).

- *The vibration test is more sensitive to changes in test boards.* The bending amplitude in the vibration test depends strongly on the difference between the excitation frequency and the resonant frequency of the component board. Hence, increasing the board thickness (or the elastic modulus) reduces the bending amplitude because of two reasons: *i)* the board becomes stiffer and *ii)* the board is not in resonance unless the excitation frequency is increased. In the drop test, only the reason *i* affects the amplitude. If the thickness is reduced, the two reasons have opposite effect on the bending amplitude in the vibration test. In the drop test, on the contrary, only the reduction in the board stiffness affects. Hence, the bending amplitude depends more on the properties of the test board in the vibration test than in the drop test, as the simulations in Chapter 9 show. Therefore, when the reliability of components on varying boards are studied by using the vibration test system, the bending amplitude of the component board should be specified, and the excitation signal should be adjusted to produce the specified bending. In the JESD22-B111 drop test standard, the test is specified in the opposite way: the excitation is specified, and the bending is measured only.

The comparison of the test methods is collected in Table XII in a numerical form. The values are personal opinions of the author. Some explanations to the given numbers are presented in the following text. `Repeatability`: the drop tester needs more maintenance than the vibration tester, but the drop test is not as sensitive

to changes in the properties of the test board. `Speed`: even though the loading is repeated much more frequently in the vibration test, the test setup takes equally long time in both tests and is the slowest step in the case of short tests (< 50 drops). `Loading type`: the loading type in the drop test is a shock load, as it is in reality, while the vibration test generates continuous harmonic loading. However, when the magnitude and frequency of the vibration were equal in the two tests, no significant differences were found in the failure modes or stress distributions. `Reliability`: in long tests the cable failure was a serious problem in the drop test, and occasionally the cable failures were difficult to detect. In the vibration test no false signals were detected.

Table XII *Evaluation of the test methods (1=bad, 4=very good).*

	repeatability	speed	versatility	loading type	reliability
drop test	2	3	1	3	2
vibration test	3	4	3	2	3

11 Conclusions

Accidental drops of portable electronic devices can cause severe loadings in interconnections. Such impacts generate large and short deceleration peaks followed by the vibration of the product that has been dropped. Inside the products solder interconnections are highly stressed between rapidly bending circuit boards and rigid components. The vibration can be very fast, a couple of hundred cycles in a second or more, depending on how the boards are attached to the body of the product and on the dimensions and materials of the boards. Because the strengths of solders depend strongly on the strain rate and temperature, stresses in interconnections during the rapid bending in drop and vibration tests increase to levels that are significantly higher than those during thermal cycling. Because of the increase in the stresses in solder interconnections, the failure modes of interconnections change from those in thermally cycled specimens. Stresses increase over the strengths of the reaction layers, and failures are usually located there, instead of being in the bulk solder as typically observed in thermally cycled assemblies.

The plastic properties of three SnAgCu-solders were measured as functions of strain rate and temperature. The solders were found to harden significantly as the strain rate increased and soften with increasing temperature. The measured values were used in determining the values of the material parameters in the Anand's creep model. The properties were utilised in the stress analysis of solder interconnections during the drop and vibration tests.

Chapter 5 discusses the strains measured on the component boards during the standardised JESD22-B111 drop test as well as the vibration test. The vibration tests were carried out at the resonance frequency of the component boards, and the measured maximum bending amplitudes of the component boards were matched to those measured during the drop tests. The measured strains were compared, and two main differences were identified: 1) In the drop tests the first bending cycle after the shock impact is very large, but the amplitude damps very quickly, whereas the bending amplitude in the vibration test remains constant throughout the test. 2) The drop test activates many natural modes of vibration, which makes the bending complex. The vibration test, on the contrary, can be used to excite only one mode,

which makes understanding the bending of the test assembly easier.

The failure analyses (in Chapter 8) of the test boards revealed the same failure modes in solder interconnections as have been observed in the drop tested boards earlier: the cracks were *i*) in the Cu_6Sn_5 intermetallic layer on the component side or less frequently on the board side, *ii*) in the phosphorus-containing reaction layer on the board side in the Ni|Au-finished boards, *iii*) in the porous Cu_3Sn layer on the component side in the annealed assemblies, *iv*) in the RCC layer of the boards under the soldering pads, and *v*) in the traces on the circuit board. In addition, when the vibration amplitude was significantly smaller, one additional mode was observed: cracking of the bulk solder. The relative lifetimes of the different test assemblies and the effect of the component location on the lifetime were similar in both tests. When the strain amplitude in the vibration test and the frequency of the vibration are adjusted to the same level as in the drop tests, the interconnections experience similar loadings in both tests. This is why the same failure modes and similar times-to-failure are observed with both the tests.

The analytical solutions of a one-dimensional system under dynamic loading were obtained to introduce the difference between free and forced vibration, the effect of the loading frequency to the response of the test structure, and the effect of the component board structure on the resonance frequency. The finite element method was employed to compare the loading conditions between the two test methods, and the induced stress levels were found to be similar. According to the finite element analysis, the method of joining the test board to the text fixture has a strong influence on the results. It was concluded that the properties of the printed wiring boards have a stronger effect on the bending of the boards during the vibration tests than during the drop tests. In the vibration test the bending amplitude depends strongly on how close to the resonant frequency of the test assembly the excitation frequency is. Therefore, their effect on the stresses and times-to-failure are correspondingly greater. Thus, it is necessary that the excitation signal of the vibration tests is controlled on the basis of measured strains or displacements of the boards.

The experimental and computational results presented above show that the vibration test can be employed successfully for studying the reliability of solder interconnections under shock loading conditions. In addition, the vibration test enables

more versatile testing and reduces the testing time of long tests considerably.

References

[00Aba1] *ABAQUS/Standard version 6.1, User's Manual*, Hibbitt, Karlsson & Sorensen, Inc., (2000).

[00Aba2] *ABAQUS/Explicit version 6.1, User's Manual*, Hibbitt, Karlsson & Sorensen, Inc., (2000).

[05Ala] M. Alajoki, L. Nguyen, and J. K. Kivilahti, "Drop test reliability of wafer level chip scale packages", *Proceedings of the 55th Electronic Components & Technology Conference*, Lake Buena Vista, Florida, USA, June 2005, IEEE, (2005), pp. 637-643.

[02Ama] M. Amagai, M. Watanabe, O. Masaki, K. Kikuo, and S. Toshikazu, "Mechanical characterization of Sn-Ag-based lead-free solders", *Microelectronics Reliability*, vol. 42, (2002), pp. 951-966.

[87Ana] L. Anand and S. Brown, "Constitutive equations for large deformations of metals at high temperatures", *Constitutive Models of Deformation*, edited by J. Chandra and R. Srivastav, SIAM, Philadelphia, (1987), pp. 1-26.

[94And] T. Anderson, *Fracture Mechanics, Fundamentals and Applications*, 2nd ed., CRC Press, (1994), p. 688.

[02Arr] M. Arra, D. Xie, and D. Shangguan, "Performance of lead-free solder joints under dynamic mechanical loading", *Proceedings of 52th Electronic Components & Technology Conference*, San Diego, California, USA, May 2002, IEEE, (2002), pp. 1256-1262.

[96Bon] N. Bonda and I. Noyan, "Effect of the specimen size in predicting the mechanical properties of PbSn solder alloys", *IEEE Transactions on Components, Packaging, and Manufacturing Technology, A*, vol. 19, 2, (1996), pp. 208-212.

[Brü] *Instruction Manual, Vibration Exciter System V*, Brüel & Kjær, p. 60.

[04Che] F. X. Che and J. H. L. Pang, "Harsh Solder Joint Reliability Tests By Impact Drop and Highly Accelerated Life Test (HALT)", *Proceedings of*

the 6th Conference on Electronics Packaging Technology, Singapore, Dec. 2004, IEEE, (2004), pp. 205-209.

[00Che] Z. Cheng, G. Wang, L. Chen, J. Wilde, and K. Becker, "Viscoplastic Anand model for solder alloys and its application", *Soldering & Surface Mount Technology*, vol. 12, 2, (2000), pp. 31-36.

[05Cho] D. Chong, K. Ng, J. Tan, P. Low, J. Pang, F. Che, B. Xiong, and L. Xu, "Drop impact reliability testing for lead-free and leaded soldered IC packages", *Proceedings of the 55th Electronic Components & Technology Conference*, Lake Buena Vista, Florida, USA, June 2005, IEEE, (2005), pp. 622-629.

[92Dar] R. Darveaux and K. Banerji, "Constitutive relations for tin-based solder joints", *IEEE Transaction on Components, Hybrids, and Manufacturing Technology*, vol. 15, 6, (1992), pp. 1013-1024.

[97Dar] R. Darveaux, "Solder joint fatigue life model", *Design and Reliability of Solders and Solder Interconnections*, ed. R. Mahidhara, D. Frear, S. Sastry, K. Murty, P. Liaw, and W. Winterbottom, The Minerals, Metals & Materials Society, (1997), pp. 213-218.

[98Des] C. Desai, C. Basaran, T. Dishongh, and J. Prince, "Thermomechanical analysis in electronic packaging with unified constitutive model for materials and joints", *IEEE Transactions on Components, Packaging, and Manufacturing Technology - B*, vol. 21, 1, (1998), pp. 87-97.

[86Die] G. Dieter, *Mechanical metallurgy*, McGraw-Hill, Inc., (1986), p. 751.

[87Dra] B. Drapkin, V. Kononenko, "Temperature dependence of Young's modulus", *Russian Metallurgy*, no. 2, (1987), pp. 168-171.

[83Eng] W. Engelmaier, "Fatigue Life of Leadless Chip Carrier Solder Joints During Power Cycling", *IEEE Transactions on Components, Hybrids, and Manufacturing Technology*, vol. 6, no. 3, (1983), pp. 232-237.

[82Fro] H. J. Frost and M. F. Ashby, *Deformation- Mechanism Maps: The Plasticity and Creep of Metals and Ceramics*, Pergamon Press, Oxford, (1982), p. 166.

[65Gar] F. Garofalo, *Fundamentals of creep and creep-rupture in metals*, Macmillan Series in Materials Science, Macmillan, New York, (1965), p. 258.

[02He] X. He and R. Fulton, "Nonlinear dynamics analysis of a laminated printed wiring board", *Journal of Electronic Packaging*, vol. 124, June, (2002), pp. 77-84.

[87Hug] T. J. R. Hughes, *The finite element method : linear static and dynamic finite element analysis*, Prentice-Hall, Englewood Cliffs, New Jersey, (1987), p. 803.

[67Ios] N. Iosipescu, "New accurate procedure for single shear testing of metals", *Journal of Materials*, vol. 2, 3, (1967), pp. 537-566.

[57Irw] G. Irwin, "Analysis of stresses and strains near the end of a crack traversing a plate", *Journal of Applied Mechanics*, vol. 24, Sept, (1957), pp. 361-364.

[03Jed] *Board Level Drop Test Method of Components for Handheld Electronic Products*, JESD22-B111, JEDEC Solid State Technology Association, July, (2003).

[95Jen] F. Jensen, *Electronic Component Reliability*, Chichester, (1995), John Wiley & Sons, p. 355.

[98Jih] E. Jih and W. Jung, "Vibrational Fatigue of Surface Mount Solder Joints", *Proceedings of 1998 InterSociety Conference on Thermal Phenomena*, IEEE, (1998), pp. 246-250.

[96Ju] S.-H. Ju, B. Sandor, and M. Plesha, "Creep rupture investigation of 63Sn-37Pb solder by experiments and damage mechanics", *Journal of Testing and Evaluation*, vol. 24, 6, (1996), pp. 411-418.

[83Kam] H. Kamioka, "Temperature variations of elastic moduli up to eutectic temperature in tin-bismuth alloys", *Japanese Journal of Applied Physics*, vol. 22, 12, (1983), pp. 1805-1809.

[01Kul] M. Kulojärvi, "Reliability characterisation of lead-free and mixed technology FBGA assemblies", Espoo, Masters Thesis, Helsinki University of Technology, (2001), p. 106.

[04Lal] P. Lall, D. Panchagade, Y. Liu, W. Johnson, and J. Suhling, "Models for reliability prediction of fine-pitch BGAs and CSPs in shock and drop-impact", *Proceedings of the 54th Electronic Components & Technology Conference*, Las Vegas, Nevada, USA, June 2004, IEEE, (2004), pp. 1296-1303.

[82Lan] T. Langdon, "Deformation at high temperatures", *Proceedings of 6th International Conference on Strength of Metals and Alloys*, August 1982, (1982), pp. 1105-1120.

[90Lau] J. H. Lau, L. Powers-Maloney, J. Baker, D. Rice, and B. Shaw, "Solder joint reliability of fine pitch surface mount technology assembly", *IEEE Transactions on Components, Hybrids, and Manufacturing Technology*, vol. 13, 3, (1990), pp. 534-544.

[05Laur] T. Laurila, V. Vuorinen, and J. K. Kivilahti, "Interfacial reactions between lead-free solders and common base materials", *Materials Science and Engineering R*, vol. 49, 1-2, (2005), pp. 1-60.

[90Lem] J. Lemaitre, J.-L. Chaboche, *Mechanics of solid materials*, Cambridge University Press, Cambridge, (1990), p. 556.

[02Lim] C. Lim, M. Teo, and V. Shim, "Numerical simulation of the drop impact response of a portable electronic product", *IEEE Transactions on Components, Packaging, and Manufacturing Technology, Part A: Packaging Technologies*, vol. 25, 3, (2002), pp. 478-485.

[01Low] K. Low, A. Yang, L. Hoon, X. Zhang, J. Lim, and K. Lim, "Initial study on the drop-impact behavior of mini Hi-Fi audio products", *Advances in Engineering Software*, vol. 32, 9, (2001), pp. 683-693.

[69Mal] L. E. Malvern, *Introduction to the Mechanics of a Continuous Medium*, New Jersey, Prentice-Hall, Inc., (1969), p. 713.

[02Mats] H. Matsuki, H. Ibuka, and H. Saka, "TEM observation of interfaces in a solder joint in a semiconductor device", *Science and Technology of Advanced Materials*, vol. 3, (2002), pp. 261-270.

[05Mat] T. T. Mattila, "Reliability of high-density lead-free solder interconnections under thermal cycling and mechanical shock loading", Espoo, Doctoral thesis, Helsinki University of Technology, (2005), p. 56.

[06Mat1] T. T. Mattila and J. K. Kivilahti, "Failure mechanisms of lead-free chip scale package interconnections under fast mechanical loading", *Journal of Electronic Materials*, vol. 34, 7, (2006), pp. 969-976.

[06Mat2] T. T. Mattila and J. K. Kivilahti, "Reliability of lead-free interconnections under consecutive thermal and mechanical loadings", *Journal of Electronic Materials*, vol. 35, 2, (2006), pp. 250-252.

[06Mat3] T. T. Mattila, P. Marjamäki, and J. K. Kivilahti, "Reliability of CSP interconnections under mechanical shock loading conditions", *IEEE Transactions on Components and Packaging Technologies*, (in print).

[04Mat] T. T. Mattila, V. Vuorinen, and J. K. Kivilahti, "Impact of printed wiring board coatings on the reliability of lead-free chip-scale package interconnections", *Journal of Materials Research*, vol. 19, 11, (2004), pp. 3214-3223.

[98Mei] Z. Mei, M. Kaufmann, A. Eslambolchi, P. Johnson, "Brittle interfacial fracture of PBGA packages soldered on electroless nickel / immersion gold", *Proceedings of the 48th IEEE Electronic Components & Technology Conference*, Seattle, Washington, USA, May, (1998), pp. 952-961.

[61Met] *Metals handbook, vol. 1: Properties and selection of metals*, ed. T. Lyman, 8th edition, American Society for Metals, (1961), p. 1300.

[81Mil] MIL-STD-721C, "Definition of terms for reliability and maintainability", The United States Department of Defense, (1981), p. 14.

[98Oco] P. D. T. O'Connor, *Practical Reliability Engineering*, Chichester, (1998), John Wiley & Sons, p. 431.

[00Ong] J. H. Ong, G. H. Lim, "A simple technique for maximizing the fundamental frequency of vibrating structures", *Journal of Electronic Packaging*, vol. 122, 12, (2000), pp. 341-349.

[04Put] M. E. Fine, "Physical basis for mechanical properties of solders", *Handbook of Lead-Free Solder Technology for Mecroelectronics Assemblies*, ed. by K. J. Puttlitz, K. A. Stalter, Marcel Dekker, Inc., New York, (2004), pp. 211-237.

[98Rei] T. Reinikainen, M. Poech, M. Krumm, and J. K. Kivilahti, "A finite-element and experimental analysis of stress distribution in various shear tests for solder joints", *Journal of Electronics Packaging*, vol. 120, March, (1998), pp. 106 - 113.

[05Rei] T. Reinikainen, P. Marjamäki, and J. K. Kivilahti, "Deformation characteristics and microstructural evolution of SnAgCu solder joint", *Proceedings of EuroSime 2005*, Berlin, Germany, April 2005, IEEE, (2005), pp. 91-98.

[68Ric] J. Rice, "A path independent integral and the approximate analysis of strain concentration by notches and cracks", *Journal of Applied Mechanics*, vol. 35, (1968), pp. 379-386.

[05Sal] O. Salmela, "Reliability assessment of telecommunications equipment", Espoo, Doctoral thesis, Helsinki University of Technology, (2005), p. 177.

[98Sim] J. C. Simo, T. J. R. Hughes, *Computational Inelasticity*, New York, Springer, (1998), p. 392.

[02Suh] E. Suhir, "Could shock tests adequately mimic drop test conditions?", *Journal of Electronic Packaging*, vol. 124, Sept, (2002), s.170-177.

[05Sye] A. Syed, S. Kim, W. Lin, J. Khim, E. Song, J. Shin, and T. Panczak, "A methodology for drop performance prediction and application for design optimization of chip scale packages", *Proceedings of the 55th Electronic*

Components & Technology Conference, Lake Buena Vista, Florida, USA, June 2005, IEEE, (2005), pp. 472-479.

[05Tan] L. Tan, C. Ang, C. Lim, V. Tan, X. Zhang, "Modal and impact analysis of modern portable electronic products", *Proceedings of the 55th Electronic Components & Technology Conference*, Lake Buena Vista, Florida, USA, June 2005, IEEE, (2005), pp. 645-653.

[95Tay] T. E. Tay, H. G. Ang, and V. P. W. Shim, "An empirical strain rate-dependent constetutive relationship for glass-fibre reinforce epoxy and pure epoxy", *Composite Structures*, vol. 33, (1995), pp. 201-210.

[99Ted] J. Tedesco, W. McDouglas, and C. Ross, *Structural dynamics: theory and applications*, Addison Wesley Longman, Inc., (1999), p. 816.

[03Tee] T. Tee, H. Ng, C. Lim, E. Pek, and Z. Zhong, "Board level drop test and simulation of TFBGA packages for telecommunication applications", *Proceedings of the 53rd Electronic Components & Technology Conference*, New Orleans, USA, May 2003, IEEE, (2003), pp. 121-129.

[59Tim] S. P. Timoshenko, S. Woinowsky-Krieger, *Theory of Plates and Shells*, McGraw-Hill, New York, (1959), p. 580.

[06Vuo] V. Vuorinen, T. Laurila, H. Yu, and J. K. Kivilahti, "Phase formation between lead-free Sn-Ag-Cu solder and Ni(P)/Au finishes", *Journal of Applied Physics*, vol. 99, 023530, (online 31 Jan 2006), pp. 1-6.

[06Vuo2] V. Vuorinen, "Interfacial reactions between Sn-base solders and common metallisations used in electronics", Espoo, Doctoral thesis, Helsinki University of Technology, (2006), p. 136.

[76War] G. B. Warburton, *The dynamic behaviour of structures*, 2nd ed., Oxford, Pergamon Press, (1976), p. 354.

[06Wei] Weiss Umwelttechnik GmbH, "Climate Test Chamber with Road Simulator", (online http://www.wut.com/en/schunk01.c.11595.de/all_wvproductsarticle, 21th Dec 2006).

[06Win] M. Winter, *WebElements*, (online http://www.webelements.com/, 22th Nov 2006).

[98Wu] J. Wu, C.-P. Yeh, and K. Wyatt, "Drop/impact simulation and test validation of telecommunication products", *The 6th Intersociety Conference on Thermal and Thermomechanical Phenomena in Electronic Systems (ITHERM)*, Seattle, Washington, May, IEEE, (1998), pp. 330-336.

[05Zen] K. Zeng, R. Stieman, T.-C. Chiu, D. Edwards, K. Ano, and K. Tu, "Kirkendall void formation in eutectic SnPb solder joints on bare Cu and its effect on joint reliability", *Journal of Applied Physics*, vol. 97, 2, (2005), pp. 1-8.

[00Zha] Y. Zhao, C. Basaran, A. Cartwright, and T. Dishongh, "Thermomechanical gehavior of micron scale solder joints under dynamic loads", *Mechanics of Materials*, vol. 32, 3, (2000), pp. 161-173.

[83Zie] O. C. Zienkiewicz, *The Finite Element Method*, McGraw-Hill, London, (1983), p. 787.

A Appendix

Table A-I *Measured strain rates* $\dot{\epsilon}_{vm}$ [1/s] *and saturated stresses* σ^*_{vm} [MPa] *with grooved lap joint specimens.*

	Sn2Ag0.5Cu			Sn3.4Ag0.8Cu			Sn4Ag0.5Cu		
T [°C]	no.	$\dot{\epsilon}_{vm}$	σ^*_{vm}	no.	$\dot{\epsilon}_{vm}$	σ^*_{vm}	no.	$\dot{\epsilon}_{vm}$	σ^*_{vm}
23	b71	1.01E+00	82	a1	5.90E-4	48.5	c1	6.30E-3	41.3
23	b72	6.74E-1	69.2	a2	5.81E-4	47	c2	6.29E-4	50.89
23	b46	6.04E-2	60.1	a3	5.61E-5	47	c3	5.78E-4	58.68
23	b47	5.88E-2	57.2	a4	5.60E-5	41	c4	6.22E-4	56.02
23	b51	5.94E-2	44.4	a21	6.00E-4	53.1	c5	6.47E-5	40.17
23	b52	5.96E-2	46.3	a34	5.75E-3	56.6	c6	6.44E-5	41.37
23	b65	5.81E-2	56	a43	5.78E-3	45.5	c8	5.15E-6	42.69
23	b66	6.01E-2	56.7	a44	5.75E-3	60.1	c10	6.21E-3	62.26
23	b12	1.19E-2	64	a45	5.78E-2	69.7	c11	6.76E-7	28.03
23	b1	5.75E-3	46.9	a46	6.02E-2	69.7	c12	1.18E-6	32.4
23	b67	5.70E-3	51.6	a49	5.93E-5	38.8	c42	5.95E-2	75.9
23	b68	5.80E-3	42	a50	5.38E-5	44.9	c43	6.08E-2	67.7
23	b58	5.87E-3	38.2	a51	5.27E-4	46.9	c45	5.82E-5	34.7
23	b59	5.86E-3	43.5	a52	5.63E-4	46.1	c46	7.61E-5	42.3
23	b20	6.35E-4	43.2	a53	5.60E-3	48.3	c47	5.55E-4	49.6
23	b2	5.75E-4	36.4	a54	5.72E-3	53	c49	5.80E-4	47.1
23	b11	5.75E-4	35.7	a57	5.74E-5	46.6	c50	5.78E-3	59.9
23	b3	5.75E-4	31.3	a58	6.00E-5	53.1	c51	5.78E-3	56.3
23	b56	5.79E-4	33.3	a59	5.70E-4	60.7	c52	5.91E-2	76.9
23	b57	6.48E-4	35.2	a60	5.48E-4	66.7	c53	6.11E-2	71.3
23	b63	5.81E-4	26.6	a61	5.77E-3	67.3	c55	9.88E-7	26.01
23	b64	5.67E-4	41.6	a62	5.75E-3	70.1	c57	6.35E-5	40.8
23	b61	5.99E-5	35.6	a63	5.97E-2	88.9	c58	1.94E-7	27.25
23	b62	5.82E-5	32.1	a64	5.80E-2	90.8			
23	b54	5.76E-5	28.1	a65	5.63E-2	79.6			
23	b55	5.82E-5	28	a66	5.72E-3	74.9			
23	b15	5.75E-5	30.5	a22	4.64E-7	26.12			
23	b5	5.55E-5	27.8	a5	2.90E-5	40			
23	b7	3.15E-5	29	a6	1.17E-5	32			
23	b8	7.65E-6	22.2	a8	2.56E-6	35			
23	b70	4.05E-6	28.09	a7	4.04E-5	36			
23	b69	5.58E-7	18.9						
23	b23	4.59E-7	19.5						

Table A-I(cont) *Measured strain rates $\dot{\epsilon}_{vm}$ and saturated stresses σ^*_{vm} with grooved lap joint specimens.*

	Sn2Ag0.5Cu			Sn3.4Ag0.8Cu			Sn4Ag0.5Cu		
T [°C]	no.	$\dot{\epsilon}_{vm}$	σ^*_{vm}	no.	$\dot{\epsilon}_{vm}$	σ^*_{vm}	no.	$\dot{\epsilon}_{vm}$	σ^*_{vm}
70	b22	5.95E-3	44.8	a27	5.82E-3	41.6	c27	5.83E-4	46
70	b24	5.80E-3	38.2	a28	5.71E-4	34.9	c28	5.75E-3	51.95
70	b16	5.75E-4	40	a29	5.77E-4	32.4	c32	6.09E-3	45.01
70	b37	5.85E-5	22.08	a30	5.84E-3	51.5	c35	5.82E-5	28.1
70	b38	5.75E-5	21.87	a36	5.76E-5	26.7	c36	5.41E-5	33.2
70	b42	3.24E-7	10.37	a37	5.72E-5	27.4	c38	2.10E-4	30.34
70	b43	2.65E-7	9.7	a47	6.24E-2	45.73	c39	9.22E-5	29.71
70				a48	6.02E-2	43	c41	2.60E-7	17.82
70				a38	3.24E-6	19.88	c44	6.42E-2	54.3
70				a39	1.13E-6	14.11	c59	5.74E-5	30.8
70				a42	1.54E-6	17.55	c60	5.80E-4	33.5
70				a40	1.44E-6	16.91	c61	5.99E-4	35.8
70							c62	1.36E-1	59
70							c64	5.93E-3	40.5
110	b17	5.80E-3	35.4	a24	5.64E-4	27.2	c26	4.04E-4	14.9
110	b21	5.05E-3	26.6	a25	5.82E-3	35	c29	6.05E-3	33.29
110	b19	5.80E-4	15.82	a26	5.92E-3	39.4	c30	5.45E-4	29.1
110	b18	5.80E-4	15.45	a31	5.57E-4	25.6	c31	5.99E-3	33.31
110	b41	5.80E-5	11.92	a33	5.57E-5	19.5	c34	5.24E-5	20.9
110	b39	5.80E-5	11.62	a35	5.80E-5	15.98	c37	6.05E-5	18.8
110	b40	5.80E-5	10.5						
110	b44	3.59E-4	16.56						
110	b45	1.40E-5	12.02						

B Appendix

Table B-I *Vibrated boards having one BGA.*

board	surface finish	via	annealing	cycles	centre ave. disp. [mm]	centre max. disp. [mm]	support ave. disp. [mm]	support max. disp. [mm]	freq. [Hz]	exc. amp. [V]
PM10-1	Sn	no	no	3312	2.20	2.46			232.56	1.5
PM10-2	Sn	no	no	1813	2.30	2.45			232.56	1.5
PM10-3	Sn	no	no	3300	2.31	2.44			232.56	1.5
PM14-2	Sn	no	no	>3000	2.34	2.65			232.56	1.5
PM1-1	Sn	no	no	728	2.75	2.98			232.56	2
PM1-2	Sn	no	no	2615	2.70	3.02			232.56	2
PM1-3	Sn	no	no	1886	2.79	3.07			232.56	2
PM6-1	Sn	no	no	384	2.51	2.74			232.56	2
PM6-2	Sn	no	no	551	2.59	2.85			232.56	2
PM6-3	Sn	no	no	772	2.56	2.82			232.56	2
PM3-1	Sn	no	yes	21	3.89	4.59	0.62	0.89	233.1	4.2
PM3-2	Sn	no	yes	29	3.94	4.61	0.61	0.90	233.1	4.2
PM3-3	Sn	no	yes	68	3.82	4.57	0.63	0.90	233.1	4.2
PM5-2	Sn	via	no	24					232.56	4.2
PM5-3	Sn	via	no	19					232.56	4.2
PM7-1	Sn	no	yes	31					232.56	4.2
PM7-2	Sn	no	yes	87	4.03	4.69	0.57	0.93	233.1	4.2
PM7-3	Sn	no	yes	179	4.02	4.69	0.60	0.89	233.1	4.2
PM12-1	Sn	no	yes	36	4.05	4.71	0.62	0.88	233.1	4.2
PM12-2	Sn	no	yes	62	3.96	4.69	0.59	0.89	233.1	4.2
PM12-3	Sn	no	yes	29	3.97	4.72	0.60	0.88	233.1	4.2
PM15-1	OSP	via	no	181	4.48	4.95			232.56	4.2
PM15-2	OSP	via	no	119	4.65	5.05			232.56	4.2
PM15-3	OSP	via	no	173	4.45	4.97			232.56	4.2
PM16-1	OSP	via	no	62	4.55	4.93			232.56	4.2
PM16-2	OSP	via	no	15	4.81	5.13			232.56	4.2
PM16-3	OSP	via	no	>201	4.59	5.11			232.56	4.2
PM17-1	OSP	via	no	44	4.71	5.11			232.56	4.2
PM17-2	OSP	via	no	84	4.69	5.16			232.56	4.2
PM17-3	OSP	via	no	28	4.83	5.16			232.56	4.2
PM18-1	OSP	via	no	144	4.76	5.08			232.56	4.2
PM18-2	OSP	via	no	49	4.74	5.01			232.56	4.2
PM18-3	OSP	via	no	50	4.62	5.10			232.56	4.2
PM19-1	NiAu	no	no	>201	4.51	5.13			232.56	4.2
PM19-2	NiAu	no	no	34	4.51	5.04			232.56	4.2
PM19-3	NiAu	no	no	47	4.45	4.94			232.56	4.2

Table B-I(cont) *Vibrated boards with one BGA.*

board	surface finish	via	annealing	failure	centre ave. disp. [mm]	centre max. disp. [mm]	support ave. disp. [mm]	support max. disp. [mm]	freq. [Hz]	exc. amp. [V]
PM20-1	NiAu	no	no	32	5.00	5.30			232.56	4.2
PM20-2	NiAu	no	no	41	4.93	5.15			232.56	4.2
PM20-3	NiAu	no	no	14	5.06	5.28			232.56	4.2
PM21-1	NiAu	no	no	119	4.78	5.09			232.56	4.2
PM21-2	NiAu	no	no	>251	4.76	5.03			232.56	4.2
PM21-3	NiAu	no	no	26	4.70	5.05			232.56	4.2
PM22-1	NiAu	no	no	>201	4.05	4.65			232.56	4.2
PM22-2	NiAu	no	no	112	4.63	5.05			232.56	4.2
PM22-3	NiAu	no	no	72	4.70	5.10			232.56	4.2

C Appendix

Table C-I *Measured displacement amplitudes at the centre of the board and the numbers of cycles to failure in the case of the fully populated vibrated boards.*

board	comp. type	displ. [mm] max.	displ. [mm] ave.	C1	C2	C3	C4	C6	C7	C8	C9
TR-5	BGA	4.36	3.86	>600	192	8	92	>600	215	16	48
TR-6	BGA	4.68	4.30	>600	11	48	246	>600	468	132	>600
TR-7	BGA	4.49	3.86	>600	4	13	41	>600	>600	34	72
TR-9	LLP48	4.47	3.98	>600	33	39	287	>600	143	22	129
TR-10	LLP48	4.54	3.96	>600	27	21	426	>600	>600	35	80
TR-11	LLP8	5.25	4.99	>1200	110	25	53	>1200	392	33	236
TR-12	LLP8	5.20	4.95	573	264	12	137	>1200	252	22	84
TR-8	LLP8	4.85	4.42	>1200	509	40	420	>1200	>1200	35	>1200

Table C-II *The numbers of drops to failure in the case of the fully populated BGA boards in the JESD22-B111 drop test.*

board	components 1	2	3	4	5	6	7	8	9	10	11	12	13	14	15
NiAu-1	22	6	5	7	51	199	115	8	63	269	217	44	5	1	165
NiAu-2	91	6	3	1	75	115	90	9	115	10	115	42	11	1	71
NiAu-3	89	42	3	25	98	167	29	7	20	179	151	22	2	6	99
NiAu-4	49	23	3	4			25	9	26			33	7	8	
NiAu-5		33	1	10	73		104	5	58			87	11	1	
NiAu-6	102	14	4	9	45		174	14	52			48	7	7	
NiAu-7		31	3	28			59	5	13			59	9	4	52
NiAu-8	33	34	3	6			47	10	46			59	9	5	
NiAu-9	2	19	3	18			76	14	36			55	8	5	39
NiAu-10	98	32	3	5	52	496	53	3	21	47	184	54	9	5	196
NiAu-11	267	15	3	7	56	304	48	11	39	110	80	48	5	6	88
NiAu-12	526	61	7	8	135	345	55	7	33	165	383	42	14	6	336
OSP-1	101	61	3	38	125		16	97	44	160		84	13	14	
OSP-2		62	7	22			86	24	50			117	13	12	
OSP-3		58	8	30	129		54	14	70			138	9	24	
OSP-4		46	4	20			78	12	47			100	8	10	
OSP-5	59	32	5	28	96		107	14	40			114	12	21	
OSP-6	28	18	6	20	39	63	31	15	23	127	136	38	12	12	29
OSP-7	111	64	21	84	111	57	346	40	108	174	342	70	24	13	189
OSP-8	63	37	7	36	210	204	70	14	53	274	124	167	13	12	392
OSP-9	258	59	10	42	246	320	177	24	45	243	355	53	51	11	142
average	119	36	5.3	21	103	227	88	17	48	160	209	70	12	8.8	150